

DEVELOPMENT OF ZnO-BASED THIN FILM TRANSISTORS AND
PHOSPHORUS-DOPED ZnO AND (Zn,Mg)O
BY PULSED LASER DEPOSITION

By

YUANJIE LI

A DISSERTATION PRESENTED TO THE GRADUATE SCHOOL
OF THE UNIVERSITY OF FLORIDA IN PARTIAL FULFILLMENT
OF THE REQUIREMENTS FOR THE DEGREE OF
DOCTOR OF PHILOSOPHY

UNIVERSITY OF FLORIDA

2006

Copyright 2006

by

Yuanjie Li

To my family

ACKNOWLEDGMENTS

I would like first to express my sincere appreciation to my advisor and committee chairman, Professor David P. Norton, for providing me all the opportunities, guidance and motivations throughout my graduate studies. I am grateful for his knowledge and support that have helped me to finish my dissertation work. I would also like to thank my supervisory committee members, Professor Stephen J. Pearton, Professor Paul Holloway, Professor Cammy R. Abernathy and Professor David Tanner, for their suggestions and guidance. I also want to thank Professor Fan Ren for his discussions and advice on my research work.

I would like to thank Professor Andrew Rinzler, Dr. Zhihong Chen and Dr. Xu Du for their help and suggestions on lithography processing. I appreciate Jau-Jiun Chen, Dr. Valentin Craciun, Dr. Brent Gila, the Major Analytical Instrumentation Center staff and many other people for their collaborations and assistance. My gratitude also goes to my group members including Mat Ivill, George Erie, Hyun-Sik Kim, Daniel Leu, Ryan Pate, Li-Chia Tien, Seemant Rawal, Charlee Calender, and Patrick Sadik for their help during my graduate research.

I would like to express my deepest appreciation and love to my family members and friends for their unconditional love and inspiration. Especially, I want to thank my parents and my husband, Shengbo Xu, for their support and encouragement that have helped me to overcome many difficulties during my development and make it to this point in life.

TABLE OF CONTENTS

	<u>page</u>
ACKNOWLEDGMENTS	iv
LIST OF TABLES	vii
LIST OF FIGURES	viii
ABSTRACT	xi
CHAPTER	
1 INTRODUCTION	1
2 BACKGROUND REVIEW.....	5
Properties of ZnO	5
Crystal Structure	5
Physical Properties	6
ZnO growth methods	8
ZnO Single Crystal	8
ZnO Thin Film.....	10
Doping of ZnO.....	11
Intrinsic defects in undoped ZnO	12
N-type doping of ZnO	14
P-type doping of ZnO	15
Nitrogen doping.....	16
Phosphorus doping	17
Arsenic doping	18
Nitrogen and group III codoping.....	18
3 EXPERIMENTAL TECHNIQUES.....	20
Film Growth via Pulsed Laser Deposition.....	20
Post-growth Annealing Process.....	23
Experimental Characterization Techniques.....	24
X-ray Diffraction	24
Scanning Electron Microscopy.....	25
Energy-dispersive X-ray Spectroscopy	25
Atomic Force Microscopy	26

	Hall Effect Measurement.....	26
	Photoluminescence	29
	X-ray Photoelectron Spectroscopy	30
	Current-voltage Measurement	31
4	DEVELOPMENT OF OXIDE-BASED THIN-FILM TRANSISTORS	32
	Introduction.....	32
	Transparent Semiconducting Oxides for Thin-Film Transistors.....	34
	ZnO-based Transparent Thin-film Transistors.....	36
	Deposition and Properties of Channel Materials.....	38
	Fabrication of ZnO-based TFTs	39
	ZnO-based TFT Device Characterization.....	47
	ZnO-TFTs Using Undoped ZnO as Active Channel Layer.....	49
	ZnO-TFTs Using P-doped ZnO and (Zn,Mg)O as Active Channel Layer.....	50
5	GROWTH AND CHARACTERIZATION OF P-TYPE PHOSPHORUS-DOPED (Zn,Mg)O BY PULSED LASER DEPOSITION	53
	Introduction.....	53
	Experimental.....	54
	Results and Discussion	55
6	SYNTHESIS AND CHARACTERIZATION OF (Zn,Mg)O:P/ZnO HETEROSTRUCTURES AND Al-DOPED ZnO	67
	Introduction.....	67
	Experimental.....	68
	Results and Discussion	69
7	GROWTH AMBIENT AND ANNEALING STUDY OF PHOSPHORUS- DOPED ZnO.....	82
	Introduction.....	82
	Experimental.....	82
	Results and Discussion	83
8	CONCLUSIONS	98
	LIST OF REFERENCES.....	102
	BIOGRAPHICAL SKETCH	112

LIST OF TABLES

<u>Table</u>	<u>page</u>
2-1 Physical properties of ZnO and GaN.	7
2-2 Different epitaxy substrates for ZnO thin film growth.	11
2-3 Valence and ionic radii of candidate dopant atoms.....	17
4-1 Properties of transparent semiconducting oxides.....	35
6-1 Growth conditions of 0.01 at. % Al-doped ZnO films via PLD.	70
6-2 FWHM values of ZnO (0002) omega rocking curve for 0.01at.% Al-doped ZnO..	74
6-3 Room temperature Hall measurement of 0.01at.% Al-doped ZnO films under different growth conditions.	76

LIST OF FIGURES

<u>Figure</u>	<u>page</u>
2-1 A schematic illustration of ZnO crystal structure.	6
2-2 Schematic of the hydrothermal growth system.	10
2-3 Defect formation enthalpies in Zn-rich and O-rich conditions after LDA corrections.	14
3-1 Schematic illustration of a pulsed laser deposition system.	23
3-2 A schematic of Hall effect on an n-type, bar-shaped semiconductor. The sample has a finite thickness of d.	28
4-1 Schematic illustration of passive and active matrix displays.	33
4-2 Electrical properties of undoped ZnO thin films grown on glass at 400°C as a function of oxygen pressure.	40
4-3 X-ray diffraction pattern of the undoped ZnO film deposited at $P_{O_2}=20\text{mTorr}$ on glass substrate.	41
4-4 An AFM image of the surface of the undoped ZnO thin film deposited at $P_{O_2}=20\text{mTorr}$ on glass substrate.	41
4-5 Schematic cross section view of a top-gate-type TFT structure.	42
4-6 Schematic fabrication sequence of ZnO-based TFT structure.	46
4-7 Top-view microscopy image of the ZnO-TFTs on glass substrate.	47
4-8 Drain current as a function of drain voltage characteristics for the undoped ZnO- TFT.	49
4-9 The output characteristics of the TFT with alternative active channel materials: (a) P-doped ZnO as the channel; (b) P-doped (Mg,Zn)O as the channel.	51
4-10 Transfer characteristics of ZnO-TFT with P-doped (Zn,Mg)O as the channel layer at the drain voltage of 6V.	52

5-1	ZnO (0002) omega rocking curves of P-doped ($Zn_{0.9}Mg_{0.1}$)O samples with and without LT-ZnO buffer layer.	57
5-2	Carrier concentration and carrier type in P-doped ($Zn_{0.9}Mg_{0.1}$)O films as a function of oxygen partial pressure.	58
5-3	Effect of oxygen partial pressure on carrier mobility of P-doped ($Zn_{0.9}Mg_{0.1}$)O films.	58
5-4	Resistivity of P-doped ($Zn_{0.9}Mg_{0.1}$)O films vs oxygen partial pressure.	59
5-5	X-ray photoelectron spectroscopy survey of P-doped ($Zn_{0.9}Mg_{0.1}$)O films.	62
5-6	X-ray photoelectron spectroscopy multiplex of P 2s peak for P-doped ($Zn_{0.9}Mg_{0.1}$)O films grown at 500°C, 150 mTorr oxygen pressure.	62
5-7	X-ray diffraction of P-doped ($Zn_{0.9}Mg_{0.1}$)O films grown under different oxygen partial pressures.	63
5-8	XRD ϕ scans of P-doped ($Zn_{0.9}Mg_{0.1}$)O film and sapphire substrate.	63
5-9	AFM images of the P-doped ($Zn_{0.9}Mg_{0.1}$)O films grown at different oxygen pressures: (a) 20; (b) 100; (c) 150; (d) 200mTorr.	64
5-10	RMS roughness of the P-doped ($Zn_{0.9}Mg_{0.1}$)O films as a function of oxygen partial pressure.	65
6-1	Schematic illustration of ZnMgO:P/ZnO heterostructure.	70
6-2	The I-V curve of Au and Ti/Au metal contacts on: (a) p-ZnMgO; (b) n-ZnO films, respectively.	72
6-3	Current-voltage characteristics of the ZnMgO/ZnO heterostructure on: (a) sapphire; (b) ZnO substrate.	73
6-4	X-ray diffraction of 0.01 at.% Al-doped ZnO films grown under different conditions.	75
6-5	Omega rocking curve of ZnO (0002) peak for 0.01 at.% Al-doped ZnO films grown under 300 mJ laser energy.	75
6-6	Laser energy effect on RT-PL for 0.01 at.% Al-doped ZnO films grown at (a) 700°C; (b) 800°C.	79
6-7	Oxygen partial pressure effect on room temperature PL of 0.01 at.% Al-doped ZnO films.	80

6-8	AFM image of 0.01 at.% Al-doped ZnO films grown under different conditions. The z-scale is 40 nm/div.....	81
7-1	Room temperature resistivity as a function of growth temperature for ZnO: P _{0.002} films grown in different gas ambient.	85
7-2	Carrier density of ZnO: P _{0.002} films as a function of growth temperature.....	87
7-3	Carrier mobility of ZnO: P _{0.002} films as a function of growth temperature.....	87
7-4	Photoluminescence spectra of P-doped ZnO grown in: (a) O ₂ /Ar/H ₂ ; (b) pure oxygen; (c) ozone/oxygen.	89
7-5	Resistivity of 0.2 at.% P-doped ZnO films annealed at different temperatures in O ₂ . The films were grown in: (a) O ₂ /Ar/H ₂ ; (b) pure oxygen; (c) ozone/oxygen.	92
7-6	Carrier concentration of 0.2 at.% P-doped ZnO films annealed at different temperatures in O ₂	93
7-7	Mobility of 0.2 at.% P-doped ZnO films annealed at different temperatures in O ₂ . The films were grown in: (a) O ₂ /Ar/H ₂ ; (b) pure oxygen; (c) ozone/oxygen.	95
7-8	RT-PL of 0.2 at.% P-doped ZnO films annealed at different temperatures in O ₂ . The films were grown at 800°C and in O ₂ /Ar/H ₂ mixture.	96
7-9	Surface morphology of 0.2 at.% P-doped ZnO films annealed at different temperatures in O ₂ . The films were grown at 700°C and in 60 mTorr O ₂	97

Abstract of Dissertation Presented to the Graduate School
of the University of Florida in Partial Fulfillment of the
Requirements for the Degree of Doctor of Philosophy

DEVELOPMENT OF ZnO-BASED THIN FILM TRANSISTORS AND
PHOSPHORUS-DOPED ZnO AND (Zn,Mg)O
BY PULSED LASER DEPOSITION

By

Yuanjie Li

May 2006

Chair: David P. Norton

Major Department: Materials Science and Engineering

Top-gate type ZnO-based TFTs were fabricated on glass substrate via photolithography and wet chemical etching processing. The ZnO layers were deposited using pulsed laser deposition (PLD). N-channel depletion-mode operation was shown for the undoped ZnO and P-doped ZnO thin film transistors. The current-voltage measurements demonstrated an enhancement-mode device operation for the thin film transistors with P-doped (Zn,Mg)O as the active channel layer.

P-type phosphorus-doped ($\text{Zn}_{0.9}\text{Mg}_{0.1}\text{O}$) films have been realized via PLD without post-annealing process. The conduction type of the films strongly depends on the oxygen partial pressure during the deposition process. Increasing the oxygen partial pressure from 20 to 200 mTorr yielded a carrier type conversion from n-type to p-type. The P-doped (Zn,Mg)O films grown at 150 mTorr oxygen partial pressure were p-type and

exhibited a hole concentration of $2.7 \times 10^{16} \text{ cm}^{-3}$, a mobility of $8.2 \text{ cm}^2/\text{Vs}$ and a resistivity of $35 \text{ } \Omega \text{-cm}$.

$(\text{Zn}_{0.9}\text{Mg}_{0.1})\text{O:P/ZnO}$ heterostructures were fabricated on sapphire and ZnO substrates via PLD with Au and Ti/Au served as Ohmic contacts. Both structures exhibit rectifying electrical characteristics. The turn-on voltages were determined to be 1.36 V and 1.15 V for the structure grown on sapphire and ZnO substrate, respectively.

The resistivity of Al-doped ZnO depends on growth temperature, laser energy and oxygen pressure. The photoluminescence properties of the Al-doped ZnO films have strong correlations to the electrical properties and crystallinity of the films. The possibility of the non-radiative trapping through deep level defect states decreases with increasing the electron density of Al-doped ZnO films. AFM results showed that the root-mean-square roughness increases with growth temperature and oxygen partial pressure.

The resistivity of the as-deposited 0.2 at.% P-doped films grown in ozone/oxygen ambient rapidly increased with growth temperature. The improvement in band edge emission intensity for the films grown in $\text{O}_2/\text{Ar}/\text{H}_2$ mixture may reflect the passivation effect of the deep acceptor-related levels by hydrogen, which also yields the passivation of the deep level emission. Oxygen interstitials may contribute to the deep level emission of RT-PL for annealed P-doped ZnO films.

CHAPTER 1 INTRODUCTION

Semiconductor devices have been exerting a critical influence on our life since the first transistor was invented at Bell Labs in 1947. The development of advanced semiconductor materials to obtain desirable properties is one of the essential contributions to modern semiconductor devices. Silicon (Si) as a conventional semiconductor material is approaching the theoretical limits by recent technology advances. To overcome the high power and high temperature limits of Si-based electronic devices, wide bandgap semiconductors such as silicon carbide (SiC), gallium nitride (GaN) and diamond have been developed to be the better candidates. For semiconductor photonic devices such as ultraviolet (UV)/blue light-emitting diodes (LEDs) and laser diodes, wide bandgap group III nitrides have been the focus of intensive research due to their specific properties.

II-VI compound semiconductor zinc oxide (ZnO) has attracted much attention because of its unique combination of electrical, optical, piezoelectric and acoustical properties for decades. With the development of recent technologies, the research interests in ZnO are renewed in a broad range of applications from optoelectronics, transparent thin film transistors (TFTs) and nanostructured materials to spintronics (spin + electronics). ZnO has a direct wide bandgap of ~ 3.3 eV at room temperature with a large saturation velocity and a high breakdown voltage. Compared with GaN, ZnO has several important advantages making it ideal for UV LEDs and lasers [1]: (1) larger exciton binding energy of 60 meV (vs. ~ 25 meV for GaN) enhancing the radiative

recombination efficiency as well as lowering turn-on voltage for laser emission; (2) the availability of large single crystal ZnO substrate desirable for vertical device development; (3) low-temperature epitaxial growth and (4) possible wet chemical etching process leading to potential low-cost ZnO-based devices. Polycrystalline ZnO gains much attention in transparent TFTs for the electronic flat panel display industry. Due to its transparency in the visible spectrum, minimal light sensitivity, and process temperatures compatible with glass/plastic technology, ZnO-based transparent TFTs show possible solutions to the limitations of Si-based TFTs [2-4]. With a reduction in crystallite size to nanometer scale, ZnO introduces novel electrical, mechanical, chemical and optical properties with rich family of nanostructures such as nanorings, nanowires and nanobelts [5]. These one dimensional (1D) materials can be used to demonstrate the potential applications in novel nanodevices. ZnO doped with transition metals such as manganese (Mn) and cobalt (Co) also shows potential in spintronic applications due to a predicted Curie temperature above room temperature [6,7].

The motivation for ZnO-based transparent TFTs is to overcome the opacity of Si-based TFTs for active matrix arrays. In addition, by using ZnO as active channel layer in TFTs the channel mobility can be increased leading to faster device operation and higher drive current [8]. Key challenges existing in ZnO-based TFTs include device structure fabrication and realization of an enhancement-mode device operation by controlled channel carrier densities. Undoped ZnO is intrinsic n-type with electron concentration in the range of $\sim 10^{18} \text{ cm}^{-3}$. High electron density causes the channel layer to be conductive even in the absence of applied gate voltage. Previous results on annealed P-doped ZnO films showed that phosphorus substitution may introduce an acceptor level that reduces

the native electron density in ZnO. Therefore, to deplete the channel electron carrier and realize the enhancement-mode operation devices, annealed P-doped ZnO and (Zn,Mg)O films were employed as the active channel materials in ZnO-based TFTs.

In order to realize the practical applications of ZnO in optoelectronic devices, both n-type and p-type materials with high carrier concentration and low resistivity have to be achieved. While n-type ZnO is easily realized via Al or Ga doping, it has shown that ZnO has the particular difficulty in producing reliable p-type conduction. This critical issue impedes the widespread development of the ZnO-based UV LEDs and lasers. Therefore, achieving high-conductivity p-type ZnO has become one of the key challenges for ZnO-based optoelectronics. Recent studies in p-type doping of ZnO have focused on group V ions such as nitrogen (N), phosphorus (P) and arsenic (As) substituted on the oxygen site [9-11]. Thus, the motivation of this part of the dissertation research was to synthesize and characterize phosphorus-doped ZnO and (Zn,Mg)O thin films for optoelectronic applications via using pulsed laser deposition (PLD).

This introduction chapter presents the challenges and motivations of this dissertation work. Following, a second chapter reviews the related background, including general properties of ZnO; growth methods for single crystal and thin films of ZnO; current experimental and theoretical studies of n- and p-type doping of ZnO. Chapter 3 describes the film growth and characterization techniques employed in this work. In chapter 4, the fabrication process and device characteristics of the top-gate type ZnO-based TFTs on glass substrates are described. Chapter 5 discusses the effect of oxygen partial pressure on the realization of p-type P-doped (Zn,Mg)O films grown on LT-ZnO buffer layer. The development of (Zn,Mg)O:P/ZnO heterostructures for light emitting

applications is the focus in the following Chapter 6. The growth condition effect on the electrical and optical properties of Al-doped ZnO is also included in Chapter 6. The systematic studies of growth condition, post-annealing on the electrical and photoluminescence as well as crystallinity and surface morphology of P-doped ZnO films are discussed in Chapter 7. Finally, chapter 8 will give the conclusions of this dissertation.

CHAPTER 2 BACKGROUND REVIEW

This chapter introduces the general properties of ZnO, including its crystal structure and physical parameters; growth methods for ZnO single crystal and thin films; n-type and p-type doping of ZnO focused on recent experimental and theoretical studies.

Properties of ZnO

Crystal Structure

Hexagonal wurtzite is the thermodynamically stable crystal structure for ZnO. There are two other phases known to exist. A zincblende phase is formed under some specific growth conditions [12]. A rocksalt structure can be synthesized under high pressure above 10 GPa at room temperature or above 6 GPa at 1200 K [13]. However, this rocksalt structure is difficult to retain under ambient conditions.

In the hexagonal wurtzite structure, each Zn cation is surrounded by four oxygen anions at the corners of a tetrahedron, and vice versa. In other words, ZnO crystal structure is composed of alternating planes of Zn^{2+} and O^{2-} ions stacking along the c-axis. Figure 2-1 presents the schematic diagram of ZnO crystal structure. ZnO shows a highly ionic character due to the large difference in electronegativity between Zn and O atoms. Non-centrosymmetric tetrahedral coordination in ZnO results in piezoelectric properties and crystallographic polarity. The oppositely charged zinc-terminated (0001) Zn-face and oxygen-terminated ($000\bar{1}$) O-face produce spontaneous polarization along the c-axis [5].

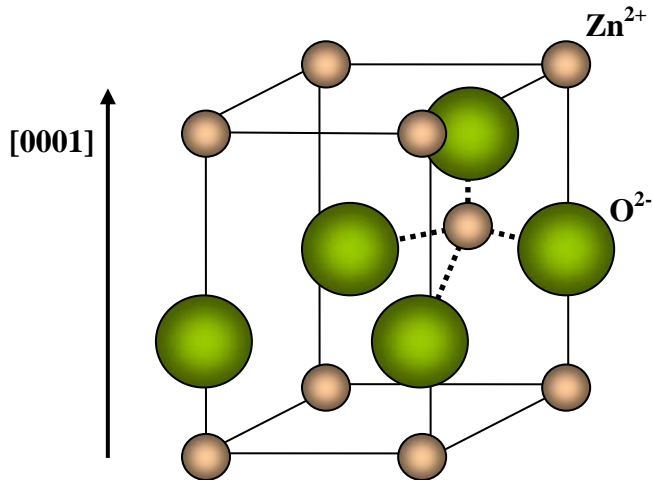


Figure 2-1. A schematic illustration of ZnO crystal structure.

Physical Properties

The physical properties of ZnO are compared to GaN in Table 2-1 [23-25]. ZnO and GaN have the same wurtzite crystal structure with $\sim 1.9\%$ lattice mismatch on the c -plane. Therefore, ZnO is a promising substrate candidate for GaN epitaxy due to its stacking order match and crystal lattice match [14, 15]. High quality, low planar defects GaN epilayers have been grown on ZnO (0001) substrate via reactive molecular beam epitaxy (MBE) [16].

ZnO has an exciton binding energy of 60 meV, which is much higher than the thermal energy at room temperature (26 meV). In principle, the excitonic recombination in semiconductors is a more efficient radiative process and can enhance low-turn-on stimulated emission [17-19]. In order to realize efficient excitonic laser action at room temperature or even higher temperature, it is essential to have an exciton binding energy greater than thermal energy at room temperature. The first optical pumping laser action in single crystal ZnO grown by vapor phase method was reported by Reynolds, Look and Jogai [20]. The lasing occurred at a very low pump power ($\sim 4 \text{ Wcm}^{-2}$) and the as-grown crystal planes act as the lasing cavity. D. M. Bagnall *et al.* [21] and P. Yu *et al.* [22]

reported UV laser emission in ZnO thin films grown on sapphire substrates at room temperature. Although the electron Hall mobility in single crystal ZnO is lower than that of GaN, ZnO has a higher saturation velocity allowing it to compete with GaN in semiconductor devices applications. In addition, ZnO is highly resistant to radiation damage making it suitable for space and other extreme operating conditions [1].

Table 2-1. Physical properties of ZnO and GaN.

Property	ZnO	GaN
Crystal structure	Wurtzite	Wurtzite
Lattice constant at 300K (nm)	$a_0 = 0.32495$ $c_0 = 0.52069$	$a_0 = 0.3189$ $c_0 = 0.5185$
Density (g cm ⁻³)	5.606	6.15
Thermal conductivity (W/cm K)	0.6	1.3
Linear expansion coefficient (K ⁻¹)	$a_0 = 6.5 \times 10^{-6}$ $c_0 = 3.0 \times 10^{-6}$	$a_0 = 5.59 \times 10^{-6}$ $c_0 = 7.75 \times 10^{-6}$
Melting point (°C)	1977	2497
Refractive index	2.008, 2.029	2.9
Bandgap at 300K (eV)	3.3	3.39
Exciton binding energy (meV)	60	25
Saturation velocity (cm s ⁻¹)	3.0×10^7	2.5×10^7
Breakdown voltage (V cm ⁻¹)	5.0×10^6	5.0×10^6

Alloying ZnO films with CdO ($E_g = 2.3$ eV) and MgO ($E_g = 7.8$ eV) makes bandgap engineering possible for realizing ZnO-based heterostructure devices [26-32]. For many advanced semiconductor devices, heterostructure designs are one of the key structures to improve the device performance via introducing band offsets and carrier confinement. The ionic radii of Cd²⁺ (0.74Å) and Mg²⁺ (0.57Å) are close to Zn²⁺ (0.60Å) [33]. According to the phase diagram of MgO-ZnO system, the thermodynamic solid solubility of MgO in ZnO is less than 4 mol% [34]. However, previous work has reported the solid solubility of MgO in ZnO thin films to be up to 33 mol% while maintaining the ZnO wurtzite structure via using pulsed laser deposition [29]. Thus, it is possible to synthesize Zn_{1-x}Mg_xO metastable phases well above the thermodynamic solubility limit by using pulsed

laser deposition techniques. Cadmium (Cd) substitution on the Zn site leads to a reduction in the bandgap to ~ 3.0 eV [26] and substituting magnesium (Mg) can increase the bandgap up to ~ 4.0 eV [29]. A quantum-confinement effect by a blueshift in photoluminescence (PL) spectra was observed in ZnO/Zn_{0.8}Mg_{0.2}O superlattices grown by laser molecular beam epitaxy (L-MBE) [35]. S. Choopun *et al.* summarized the bandgap relations in Zn_{1-x}Mg_xO as a function of composition via a virtual crystal approximation [30]. For $x = 0$ to 0.33, the bandgaps of Zn_{1-x}Mg_xO have a linear dependence on Mg content and the films retain the hexagonal structure. For $x = 0.33$ -0.35, there is a discontinuity in the bandgap relation due to the structural transition from wurtzite to cubic phase.

ZnO growth methods

ZnO Single Crystal

There are three important growth methods for bulk ZnO single crystal: pressurized melt growth [36], seeded sublimation growth [37] and hydrothermal solution growth [38-40].

Pressurized melt growth employs the use of modified Bridgman configuration developed by Cermet, Inc. High quality ZnO wafers up to 2-inch in diameter are commercially available [41]. This technology involves a high pressure induction melting apparatus, where the melt is contained in a water-cooled crucible [36]. An overpressure of the oxygen as the growth atmosphere can overcome the ZnO decomposition problems during heating under normal melt growth pressures. Radio frequency energy is used as the source to melt the material. Part of the molten phase is cooled by the cold crucible wall with the same composition as the melt. This cold material prevents the molten material from direct contacting with the cooling wall surface, which eliminates the

contamination possibilities from the reactive crucible. High crystal quality (linewidths as low as 49 arcsec) and low defect density (10^4 cm^{-2}) ZnO crystals can be produced in a fast growth rate ($1\text{-}5 \text{ mm h}^{-1}$) by using this method [36].

Seeded sublimation growth or vapor-phase growth technique uses pure ZnO powder formed by the reaction of Zn-vapor and oxygen as the source material. This ZnO source is put at the hot end of a horizontal tube which maintains at a certain growth temperature. Hydrogen is used as a carrier gas during the process to make the growth reactions achievable. At the hot end of the tube the possible reaction follows $\text{ZnO(s)} + \text{H}_2(\text{g}) \rightarrow \text{Zn(g)} + \text{H}_2\text{O(g)}$. A reverse reaction takes place at the cold end to form ZnO assisted by a single crystal seed [37]. High quality ZnO crystal has been grown by Eagle-Picher Technologies using this method. Room temperature mobility is about $225 \text{ cm}^2/\text{Vs}$ and an electron concentration is in the range of mid- 10^{16} cm^{-3} [37].

Several works have reported high quality bulk ZnO single crystals grown hydrothermally. Hydrothermal autoclaves made of high strength steel were used for crystal growth. During the growth, high purity ZnO nutrient mixed with the solvent (also called as mineralizer) is sealed in a platinum (Pt) inner container [40]. The purpose of using Pt inner container is to isolate the growth environment from the wall of the autoclave. There are two zones in the Pt container: the crystal growth zone and the dissolution zone. Figure 2-2 shows a schematic hydrothermal growth system. The major parameters of this growth technique are the temperature of growth zone, the temperature difference between the two zones, the pressure and the concentration of the mineralizer [40]. Good quality ZnO single crystals have been achieved using this technology with a growth rate about 0.2mm per day [39].

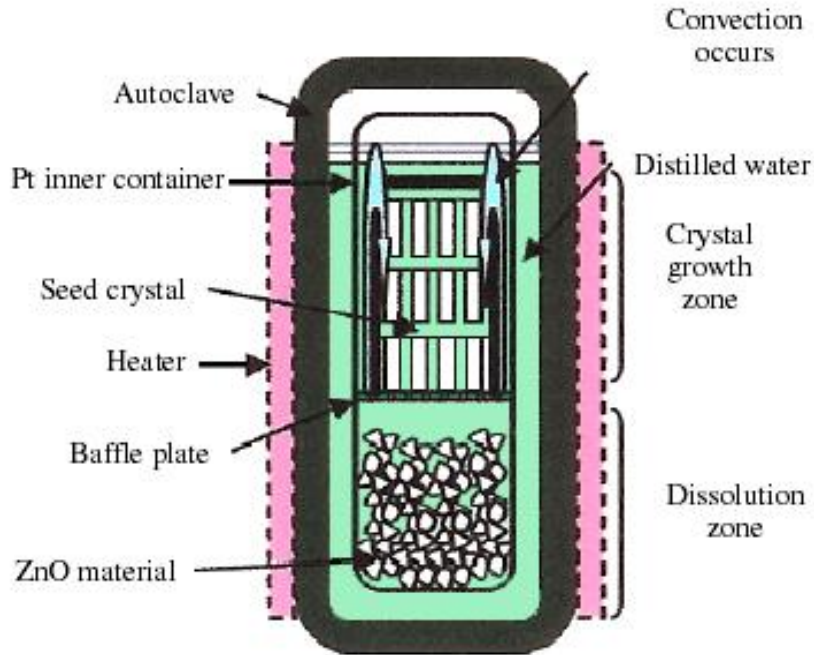


Figure 2-2. Schematic of the hydrothermal growth system [40].

ZnO Thin Film

ZnO epitaxial thin films have been grown via numerous deposition techniques including molecular beam epitaxy (MBE), pulsed laser deposition (PLD), radio-frequency (RF) magnetron sputtering and metal-organic chemical vapor deposition (MOCVD) etc. All the ZnO and (Zn,Mg)O films presented in this dissertation were synthesized via using pulsed laser deposition. The detailed description of this technique is included in the following chapter.

Different substrates for ZnO thin film epitaxy are listed in Table 2-2. The most common substrate used for ZnO thin films is sapphire due to its hexagonal structure, low cost and high crystal quality. (0001) *c*-plane sapphire has been used frequently for growing epitaxial ZnO films due to the strong tendency of ZnO to grown in *c* orientation. Other possible substrates include (11 $\bar{2}$ 0) *a*-plane sapphire, (1 $\bar{1}$ 02) *r*-plane sapphire and SiC. Most of the substrates have a large lattice mismatch with ZnO. The lattice-matched

substrate for ZnO is (0001) ScAlMgO₄ (SCAM) which consists of alternating stacks of rock salt layers and wurtzite layers [47]. A number of studies have reported the growth of epitaxial ZnO and ZnO-based device structures on (0001) SCAM substrate [47-49].

Polycrystalline ZnO films can also be grown on inexpensive substrates such as glass at low temperatures [55, 56]. By using these characteristics it is possible to realize thin film transistors by using ZnO as the active channel layer for displays and transparent electronic devices.

Table 2-2. Different epitaxy substrates for ZnO thin film growth.

Substrate	Crystal structure	Orientation	Mismatch (%)	Reference
<i>c</i> -plane Al ₂ O ₃		(0001)	18.3	[42-45]
<i>a</i> -plane Al ₂ O ₃	hexagonal	(11 $\bar{2}$ 0)	...	[46]
<i>r</i> -plane Al ₂ O ₃		(1 $\bar{1}$ 02)	...	[47]
ScAlMgO ₄	hexagonal	(0001)	0.09	[48-50]
GaN	wurtzite	(0001)	1.9	[51]
SiC	wurtzite	(0001)	5.5	[52]
Si	diamond	(100)	...	[53,54]

Doping of ZnO

To realize ZnO-related materials in electronic and photonic applications, both high quality, low resistivity n- and p-type ZnO have to be achieved. However, wide bandgap semiconductors such as ZnSe, ZnS, ZnTe or CdS can be doped either n-type or p-type, but not both [57]. ZnSe and GaN can be easily doped n-type, but p-type doping is difficult to be realized. On the contrary, ZnTe is hard to dope n-type while p-type is formed readily. This asymmetry in n-type versus p-type doping also exists in ZnO [58,59]. While n-type ZnO is easily realized via Al, Ga or In doping, ZnO exhibits significant resistance to the formation of shallow acceptor levels. To explore and realize the p-type doping of ZnO, it is essential to understand intrinsic defects in undoped ZnO. The following sections discuss the intrinsic donors and acceptors in undoped ZnO,

introduce the n-type doping of ZnO and largely focus on the recent experimental and theoretical studies of p-type ZnO doped with nitrogen (N), phosphorus (P), arsenic (As) as well as co-doped with N and group III elements.

Intrinsic defects in undoped ZnO

Undoped ZnO is an n-type semiconductor with various electron concentrations from mid- 10^{16} cm^{-3} in high quality single crystal [60] to $\sim 10^{18} \text{ cm}^{-3}$ in epitaxial thin films grown on sapphire substrates. The origins of the dominant donors in undoped ZnO have been investigated both theoretically and experimentally [61-68]. In the study of native defects in ZnO by Kohan *et al.* [61] the most dominant native defects are suggested to be Zn and O vacancies depending on the Zn partial pressure. The calculations based on the first-principles pseudopotential method indicated that in Zn-rich conditions oxygen vacancy (V_O) has lower energy than zinc interstitial (Zn_I) for all Fermi-level positions. For oxygen-rich conditions, zinc vacancy (V_{Zn}) dominant over the whole range of Fermi level range. Zhang *et al.* [62] calculated the formation enthalpies of the intrinsic defects in ZnO such as V_O , Zn_I , Zn-on-O antisite (Zn_O), V_{Zn} and oxygen interstitial (O_I) based on the plane-wave pseudopotential total energy and force method. Figure 2-3 shows the defect formation enthalpies after the local density approximation (LDA) corrections. It suggests that both Zn_I and V_O have low formation enthalpies. In contrast, the native acceptor defects V_{Zn} and O_I have high formation enthalpies for Zn-rich conditions. Therefore, undoped ZnO shows intrinsic n-type conduction and can not be doped p-type by these intrinsic acceptor defects. The study, however, suggested that Zn_I is a shallower donor than V_O , thus it is considered to be the dominant intrinsic donor in ZnO. Look *et al.* [63] studied high-energy electron irradiation on both ZnO (0001) and (000 $\bar{1}$) face

samples and found the donors and acceptors production rate is much higher for Zn-face irradiation. The donor is assigned to a Zn-sublattice defect which has an activation energy of about 30 meV suggesting that Zn_i (and not V_O) is the dominant native shallow donor in ZnO. Recent work by Janotti *et al.* also indicated that V_O is too high in energy to play any significant role in as-grown *n*-type material. However, it is expected to act as a compensating center in p-type ZnO and it can also be formed during irradiation and ion implantation [64].

Several experimental and theoretical studies have shown that there is another candidate for the dominant donor defect in undoped ZnO [65,66]. First-principles calculation based on density functional theory (DFT) found that high electron concentration (10^{17} - 10^{18} cm^{-3}) in undoped ZnO may result from the presence of hydrogen (H) as a shallow donor [65]. Hydrogen forms a strong bond with oxygen providing a strong driving force to incorporate into ZnO. The incorporation of hydrogen in ZnO results in significant relaxations of surrounding atoms and always occurs as a positive charge. The formation energy of H^+ is low to allow a large solubility of hydrogen in ZnO. Since hydrogen is generally present in the films growth ambient and has a high diffusion coefficient into ZnO, control of hydrogen exposure during film growth has to be carefully carried out.

The native acceptors in undoped ZnO including zinc vacancy (V_{Zn}) and oxygen interstitial (O_i) have high formation enthalpies in Zn-rich conditions, so these defects are not abundant [61]. Recent work by Tuomisto *et al.* [68] studied the dominant acceptor in undoped ZnO by using temperature-dependent Hall measurements and positron annihilation spectroscopy. It was shown that V_{Zn} densities in as-grown and irradiated

ZnO have a good agreement with the total acceptor densities determined by temperature-dependent Hall measurements. Thus, V_{Zn} is identified as a possible dominant acceptor in both as-grown and irradiated ZnO.

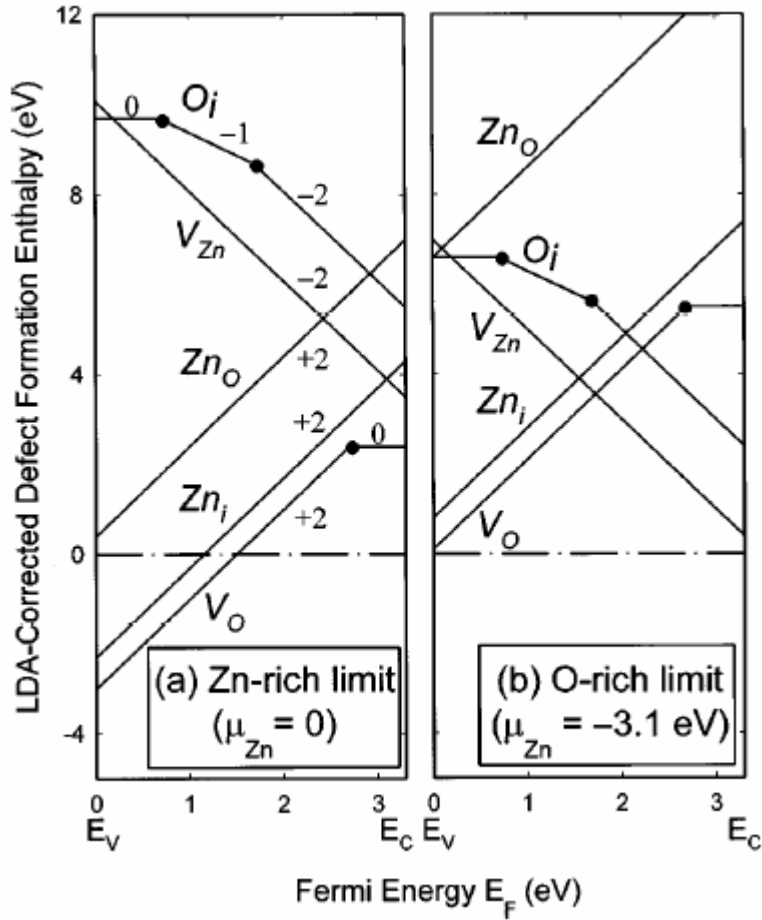


Figure 2-3. Defect formation enthalpies in Zn-rich and O-rich conditions after LDA corrections [61].

N-type doping of ZnO

Group III elements such as Al, Ga and In can act as extrinsic donors for ZnO by substitution on Zn site. High quality and high electron concentration n-type ZnO epitaxial films have been successfully synthesized by using MBE, sputtering or MOCVD [69-72]. Highly conductive and transparent n-type ZnO films have been utilized as a potential candidate to replace indium tin oxide (ITO) for displays and solar cells. Miyazaki *et al.*

[69] reported transparent conductive Ga-doped ZnO films deposited on glass substrate having a minimum resistivity of $2.2 \times 10^{-4} \Omega \text{ cm}$ at substrate temperature of 250°C .

Highly conductive Al-doped ZnO thin films with average transmittance over 91% in the visible spectrum region has been deposited by using photo-MOCVD method [70]. Chang *et al.* [72] also synthesized Al-doped ZnO thin films on silicon and glass substrates by RF magnetron sputtering. The dependence of film properties on different growth parameters such as RF power, substrate temperature, oxygen pressure and target composition was examined systematically.

P-type doping of ZnO

As mentioned earlier, theoretical and experimental studies have shown the asymmetry of n-type versus p-type doping of ZnO. There are several possible mechanisms to explain these difficulties [73-75]. First, the acceptor dopants may have low solubility in the host material to limit the accessible hole concentration. In ZnO, the native donor defects have low formation enthalpies and thus compensate extrinsic acceptors. Zunger [76] proposed that in ZnO, the p-type pinning energy $E_F^{(p)}$ where the native “hole killers” spontaneously form to compensate p-type doping is considerably above the valence band maximum (VBM). The Fermi energy E_F in extrinsic p-type doping which moves downwards will encounter $E_F^{(p)}$ first before encountering the VBM. As a result, “hole killers” such as Zn_I and V_O will be generated spontaneously before any significant doping commences. Moreover, acceptor dopants can form deep levels in ZnO that are not easily activated at room temperature. The doping difficulty in p-type ZnO may also result from other compensation mechanisms such as the formation of deep defect AX centers through a double broken bond (DBB) mechanism [73]. The net result

of the formation of these defect complexes is releasing two electrons (equivalent to capture of two holes). Recent research in p-type dopants has mainly focused on group V ions such as N, P, As or Sb substituted on the O site. The following sections will present these results.

Nitrogen doping

Table 2-3 lists the valence and ionic radii of candidate acceptor dopants. Among the group V atoms, N has the closest ionic radius to that of O. Theoretical studies also suggested that N has some advantages for p-type doping of ZnO such as the smallest ionization energy and metastable N AX complexes [73]. There have been significant activities focused on N doping by using different nitrogen sources including NH₃, N₂, N₂O, NO and Zn₃N₂ [77-88]. Minegishi *et al.* [77] reported p-type ZnO doped with N by simultaneous addition of NH₃ in hydrogen and excess Zn in source ZnO powder. A proposed model explained that the high resistivity of about 100 Ω cm may be reduced via thermal annealing. Look *et al.* [78] reported p-type ZnO grown by MBE using N₂ RF plasma source and Li-diffused semi-insulating ZnO substrates. The N-doped ZnO layers showed a hole concentration of $9 \times 10^{16} \text{ cm}^{-3}$, a mobility of $2 \text{ cm}^2/\text{Vs}$ and a resistivity of 40 Ω cm. In another case, p-type ZnO has been grown by PLD, in which a N₂O plasma is used for doping [80]. Iwata *et al.* [81] grew N-doped ZnO using MBE by introducing N₂ and O₂ through a RF radical source. However, type conversion from n-type to p-type did not occur even though the N concentration was in the range of 10^{19} cm^{-3} . It is suggested that the formation of N-N related complexes introduce compensating defects. Thus, dopant sources contain only one nitrogen atom such as NO and NO₂ are considered to be better choices due to the large dissociation energy of N-N in N₂ (9.76 eV) [75]. Yan and

co-workers [82] proposed a theoretical model predicting that the defect formation energy of N on O site (N_O) from NO is negative in Zn-rich conditions and lower than that from N_2O . Li *et al.* [83] reported on the realization of p-type ZnO using NO gas as the dopant source by MOCVD. The carrier concentration is in the range of 10^{15} - 10^{18} cm^{-3} and mobility is in the range of 10^{-1} cm^2/Vs .

Table 2-3. Valence and ionic radii of candidate dopant atoms [75].

Atom	Valence	Radius (Å)
Zn	2+	0.60
Li	1+	0.59
Ag	1+	1.00
O	2-	1.38
N	3-	1.46
P	3-	2.12
As	3-	2.22
Sb	3-	2.45

Phosphorus doping

While there have been many activities focused on nitrogen doping, few reported efforts have addressed phosphorus doping. Nevertheless, Aoki *et al.* reported *p-n* junction-like behavior between an n-type ZnO substrate and a surface layer that was heavily doped with phosphorus [89]. Zinc-phosphide (Zn_3P_2) used as the phosphorus dopant source was decomposed into Zn and P atoms by excimer laser radiation in high pressure oxygen or nitrogen ambient. Light emission also was observed by forward current injection at 110 K indicating that a p-type ZnO was formed.

Work by K. Kim *et al.* on P-doped ZnO films grown by sputter deposition showed that n-type as-grown films were converted to p-type by a thermal annealing process to activate the P dopant [90]. In this case, phosphorus was doped in ZnO using the ZnO target mixed with 1 wt% P_2O_5 . XPS results of the p-type ZnO showed that the P_{2p} peak came from P_2O_5 in the film. The p-type films showed a low resistivity of 0.59-4.4 Ω cm,

a hole concentration of 1×10^{17} - $1.7 \times 10^{19} \text{ cm}^{-3}$ and a mobility of 0.53 - $3.52 \text{ cm}^2/\text{Vs}$. These results indicate that phosphorus is another promising acceptor dopant for p-type ZnO.

Our previous annealing studies on P-doped ZnO films grown on sapphire substrates by PLD showed that post-growth annealing process yielded semi-insulating behavior which is consistent with activation of a deep acceptor level [91].

Arsenic doping

Although density functional theory (DFT) predicts that As_O should have a very deep acceptor level ($\sim 1.15 \text{ eV}$) based on the large ionic size difference between As and O, Ryu *et al.* [92] have synthesized p-type ZnO by As diffusion from a GaAs substrate. The hole concentration can be increased up to the mid- 10^{17} cm^{-3} range. Homostructural ZnO *p-n* junctions based on As-doped ZnO has also been reported [93]. Based on first-principles calculations, a model for large-size-mismatched group-V dopants such as As and Sb in ZnO was proposed by Limpijumng and co-workers [94]. These dopants do not occupy the O sites, but on the Zn sites: each forms a complex with two spontaneously induced Zn vacancies in a process that involves fivefold As coordination. The model also predicted that *p*-type ZnO doped with As could be realized under O-rich growth or annealing conditions.

Nitrogen and group III codoping

A codoping method refers to using N acceptors and group III donors such as Ga, Al or In as the reactive codopant to increase the N incorporation in ZnO [95]. The theoretical calculations showed that codoping wurtzite ZnO with N and group III elements, the distance between two N acceptors decreases from 6.41 \AA to 4.57 \AA indicating the enhancement of N incorporation. It also showed that the simultaneous codoping

decreases the Madelung energy of p-type codoped ZnO compared with p-type ZnO doped only with N. Several research groups reported the realization of p-type ZnO using codoping method. Joseph *et al.* [96] demonstrated p-type ZnO films by applying Ga and N codoping method. A resistivity of 0.5 Ωcm and a carrier concentration of $5 \times 10^{19} \text{cm}^{-3}$ have been obtained in ZnO films on glass substrate. Singh *et al.* [97] also reported p-type conduction in ZnO by using N and Ga codoping technique. Ye and co-workers [98,99] reported p-type ZnO thin films realized by the N-Al codoping method. Secondary ion mass spectroscopy showed that the N incorporation was enhanced by the presence of Al in ZnO. The lowest room temperature resistivity is 57.3 Ω , with a Hall mobility of 0.43 cm^2/Vs and carrier concentration of $2.25 \times 10^{17} \text{cm}^{-3}$ for the N-Al codoped film grown on glass substrate.

CHAPTER 3 EXPERIMENTAL TECHNIQUES

This chapter describes the details of the experimental techniques and procedures applied to the deposition of phosphorus-doped ZnO and (Zn,Mg)O thin films, post-growth annealing process and characterization measurements for structural, surface morphology, transport, optical as well as chemical state properties of the films.

Film Growth via Pulsed Laser Deposition

Pulsed laser deposition has been used for epitaxial growth of thin films and multilayer/superlattice of complex materials. It provides many important advantages for oxide films with high melting points and complicated stoichiometry, some of which can not be achieved by using other growth techniques such as sputtering, MBE or MOCVD [100]. PLD was the first method used to successfully deposit high-temperature superconducting thin films [101,102]. The main advantage of PLD derived from the laser material removal mechanisms. A pulsed laser ablates the target with very high peak energy to evaporate the target material without change in the target composition. The evaporants, also called a plume, arrives at the heated sample substrate and then starts the film growth. As a result, films with the desirable stoichiometry similar to the target can be obtained by using PLD. Other advantages of PLD include the easy adaptation to different operational modes with no constraints from the internal powered sources and the ability to change the deposition gas pressure over a broad range as well as a high deposition rate [100].

In principle, the film deposition process in PLD can be divided into three separate stages: (1) the interaction of the laser beam with the target material; (2) dynamic formation of plasma; (3) plasma isothermal expansion and deposition of thin films [103]. In the first stage, the target material is rapidly heated above its melting point by the high peak energy laser pulses. The evaporation of the target material with the same stoichiometry as the target occurs. The turn-on energy defined as the minimum laser energy above which appreciable evaporation is observed depends on the laser wavelength, pulse duration, plasma losses as well as the optical and thermal properties of target material [103]. The interaction of the laser beam with the target involves several mechanisms such as thermal, collisional, electronic, exfoliation and hydrodynamic sputtering [100].

The evaporated mixture of energetic species including atoms, molecules, electrons, ions, and micron sized particulates further interacts with the laser beam by absorbing the laser energy to generate a high-temperature plasma. The particle density in the plasma depends on the ionization degree, evaporation rate and the plasma expansion velocities. Most of the evaporated species are deposited perpendicular to the laser spot. However, the thickness variation existing in the films is larger than that from a conventional thermal evaporation process [103].

The plasma expansion is isothermal in vacuum due to the termination of the laser pulse. With the kinetic energy in the plasma, it retains its elliptical shape during the deposition process. Nucleation and growth of film starts after a condensation region on the substrate is formed. Substrate temperature and surface mobility of the deposited species affect the quality of thin film. Two dimensional, i.e. layer-by-layer growth is

more preferable compared to the three dimensional (island) growth in order to obtain high quality epitaxial thin films.

Compared to the laser-target interaction and film deposition mechanisms, the system setup is much simpler. A PLD system is usually composed of an excimer laser, optical elements to guide and focus the laser beam and a vacuum chamber. Figure 3-1 shows a schematic of a PLD system along with the laser and optic lenses. In this work, a Lambda Physik (COMPEX 205) KrF excimer laser which delivers 248 nm wavelength and maximum average power of 50 W was used. The laser influence is in the range of 1-3 J/cm² and a laser repetition rate from 1 to 10 Hz was used for the film growth. Multiple targets can be installed inside the chamber simultaneously to realize multilayer and superlattice structures with a target to substrate distance of 4-5 cm. A quartz lamp heater was used to heat sample substrates up to 950°C. The chamber pumping system consists of an oil-free diaphragm roughing pump and Pfeiffer turbo pumps. The base pressure of the growth chamber was in the range of 8×10^{-8} - 2×10^{-7} Torr. By using a mass flow control valve (MKS 600 series) it is possible to adjust input of different gases into the chamber in a wide range of deposition pressures from high vacuum ($\sim 10^{-7}$) to 10^{-1} Torr.

There are several factors that play important roles in obtaining high quality thin films grown via PLD. The laser energy density on the target has a significant effect on particulate formation. In order to make laser ablation occur, the laser energy has to exceed the turn-on energy of the target material. However, if the laser energy is much greater than the turn-on energy, the density of the particulates will increase. Therefore, it is important to use the optimal laser energy density to obtain high quality films. An external energy meter was used to determine the actual laser energy reaching the target in

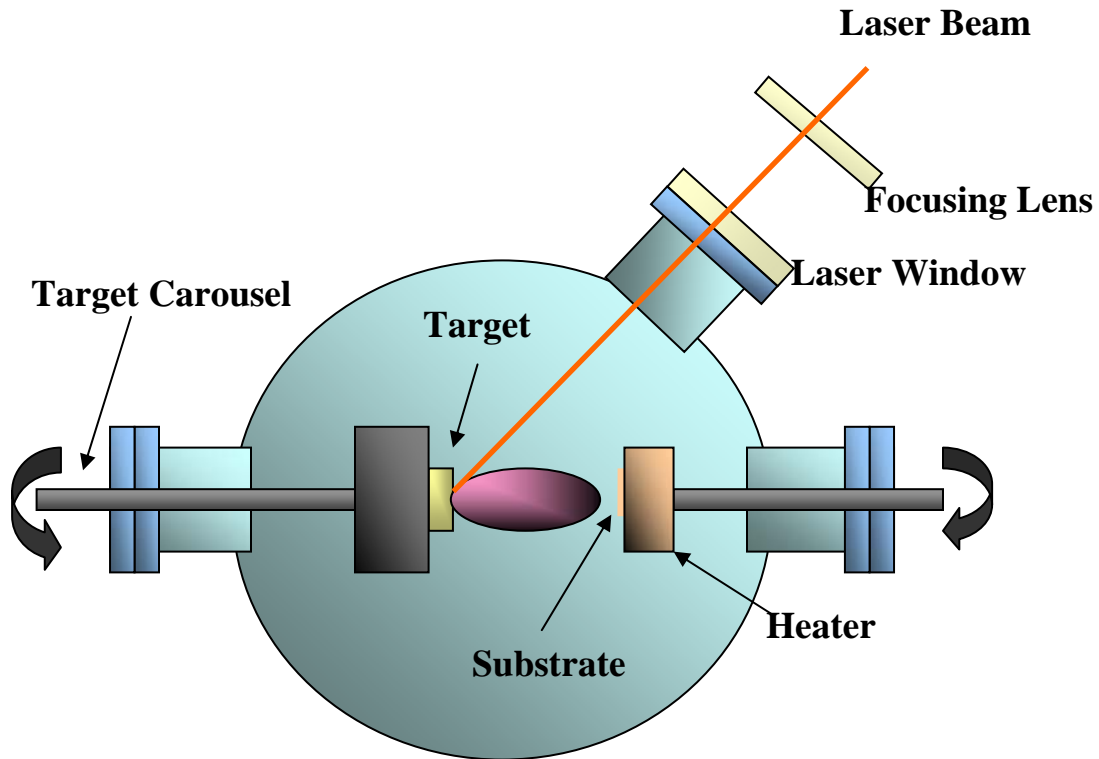


Figure 3-1. Schematic illustration of a pulsed laser deposition system.

front of the chamber laser window. The laser energy can be adjusted by panel settings based on the external energy meter values during every experimental growth. In addition, pre-ablation of the target is necessary to have a stable deposition rate and decrease the particulate formation. Pre-ablation of the targets with a high laser repetition rate of 10 Hz was used for 1000-2000 laser shots before the films growth. Deposition gas pressure and substrate temperature also influence the films growth rate, the kinetic energy distribution of depositing species, as well as the films crystal structure [100]. Therefore, it is essential to carry out the systematic studies of these growth condition effects on the film properties.

Post-growth Annealing Process

There are two different post-growth annealing processes conducted in this dissertation work: in-situ chamber annealing and tube furnace annealing. In-situ chamber annealing was carried out after film growth. The annealing gas pressure could be

increased to above 100 Torr. This annealing process overcomes the possible surface contamination imposed by taking samples out the vacuum chamber for post-annealing. However, the annealing gas pressure is limited to certain levels. Compared to chamber annealing, tube furnace is more versatile in realizing high temperature ($\sim 1100^\circ\text{C}$), controlled gas pressure (up to 1 atmosphere) and different ambients annealing. An alumina crucible containing the samples was located at the center of a quartz tube, where the temperature has been calibrated. The annealing tube was purged with high purity annealing gas for up to 8 hours before increasing the temperature. Desirable heating and cooling rates can be realized by using a pre-programmed temperature controller.

Experimental Characterization Techniques

This section describes the different characterization techniques used to investigate the structural, surface morphology, transport, optical and chemical bonding properties of the as-grown and annealed films. The effects of growth pressure, temperature, ambient, dopant concentration and annealing conditions on film properties were explored.

X-ray Diffraction

X-ray diffraction (XRD) is an important technique to analyze the crystallinity, phase, strain, preferred orientation and defects of samples. A collimated beam of X rays is incident on a sample and diffracted by the crystalline phases in the sample according to Bragg's law such that

$$\lambda = 2d \sin \theta \quad (3-1)$$

where λ is the wavelength of the incident X-ray, d is the spacing between atomic planes in the crystalline phase, θ is the angle between atomic planes and the incident X-ray beam. The intensity of the diffracted X-rays is measured as a function of the diffraction angle 2θ . This diffraction pattern is used to identify the sample crystalline phases [104].

A Philips APD 3720 X-ray diffractometer with Cu K α ($\lambda = 1.5406\text{\AA}$) was used to examine the films structure and crystallinity in this work. The 2θ scan range is from 30 to 75 degree. Omega rocking curve was measured by using a four-circle Philips X'pert X-ray diffractometer. The full-width-at-half-maximum of the rocking curve was used to delineate the films crystallinity.

Scanning Electron Microscopy

Scanning Electron Microscopy (SEM) is a useful instrument to examine the sample surface when the light microscope reaches its resolution limits. In the SEM, an electron beam is focused into a fine probe and scanned over a small area on the sample. Different signals such as secondary electrons, photon emissions as well as internal currents are created by the electron beam and sample interactions. These emitted signals are collected by detectors and subsequently an image is produced on a cathode ray tube (CRT) [104].

A JEOL 6400 scanning electron microscopy was used to investigate the sample surface in low and high magnifications. The SEM was operated at 10-15 keV depending on the conductivity of the sample surface. The sample surface was not coated with a carbon layer and preserved in its original status for other characterization measurements.

Energy-dispersive X-ray Spectroscopy

Qualitative and semi-quantitative analysis of elements presenting in a sample can be achieved by using energy-dispersive X-ray spectroscopy (EDS). When atoms are ionized by a high-energy radiation they emit characteristic X-rays. A solid state detector made from Si(Li) is used to convert these X-rays into signals which are then processed into an X-ray energy spectrum. Most applications of EDS are in electron column instruments like SEM, field emission-SEM, transmission electron microscope [104]. In

this dissertation work, EDS was used to determine the composition of the surface particulates as well as the films. However, the relative accuracies are about 10% for the elements with concentration less than 5 wt% [104].

Atomic Force Microscopy

In order to measure the surface roughness and topography with atomic resolution, atomic force microscopy (AFM) is a valuable technique. Unlike electron microscopes, the resolution of AFM is determined by the size of the tip instead of electron beam diffraction effects. In addition, a wide range of samples including metals, polymers, glasses, semiconductors, thin films and composites can be measured in air even in liquids. AFM works by measuring attractive or repulsive van der Waals forces between the atoms of a tip and sample surface [105]. The magnitude of the deflection resulting from these forces depends on the tunneling current and the tip-to-sample distance. A highly position-sensitive photodiode detects the tip cantilever deflection and converts the signal to an image.

In this work, AFM Dimension 3100 (Digital Instrument, Inc.) was performed in contact mode to obtain the surface topographic images and roughness of as-grown and annealed samples under different conditions. Root-mean-square (RMS) roughness was calculated based on 2×2 or $5 \times 5 \mu\text{m}^2$ scan area. The scan rate is in the range of 1-1.5 Hz.

Hall Effect Measurement

Since its discovery by Edwin H. Hall (1879) the Hall effect has become one of the most important electrical characterization methods of materials. The Hall effect provides

a relative simple way of measuring the carrier density, electrical resistivity and the mobility of carriers in semiconductors.

The principle underlining the Hall effect is Lorenz force which is defined as a force exerted on a charged particle in an electromagnetic field. Figure 3-2 shows an n-type, bar-shaped semiconductor. It is assumed that a constant current I flows along the x-axis from left to right in the presence of a z-directed magnetic field. Under Lorenz force electrons drift toward the negative y-axis and accumulate on the side of the sample to produce an electrical surface charge. As a result, a potential drop across the sample called Hall voltage is formed. The induced electric field increases until it counteracts to the opposite Lorenz force. In this case,

$$eE_y = ev_x B = -eBj_x / ne \quad (3-2)$$

where eE_y is the induced electric field force, $ev_x B$ is the Lorenz force, $j_x = nev_x$ is the total current density. The Hall coefficient R_H is defined as

$$R_H = -\frac{1}{ne} \quad (3-3)$$

The mobility is defined as the coefficient of proportionality between v and E and measured as follows:

$$\mu = \frac{v_x}{E_x} = -\frac{j}{neE_x} = R_H \sigma \quad (3-4)$$

where σ is the conductivity. For p-type semiconductors, a hole has a positive charge e .

Therefore, the Hall coefficient is positive in sign.

The Van der Pauw technique which requires no dimension measured for the calculation of sheet resistance or sheet carrier density solves the potential problem in a thin layer of arbitrary shape. Thus, this method has increased in popularity relative to the Hall-bar configuration. The validity of the van der Pauw method requires that the sample

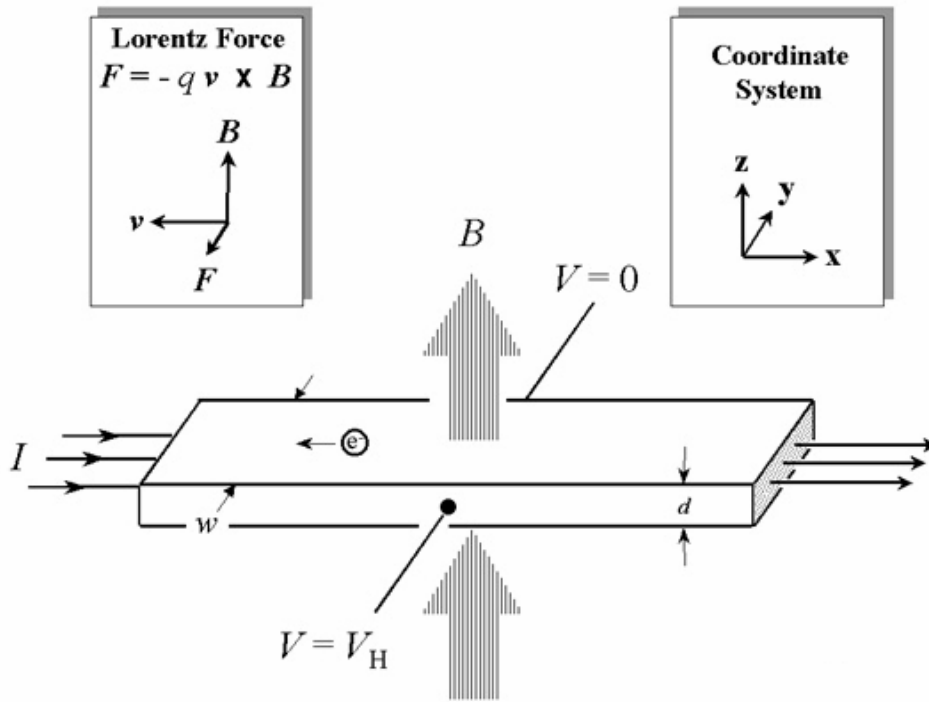


Figure 3-2. A schematic of Hall effect on an n-type, bar-shaped semiconductor. The sample has a finite thickness of d [106].

be flat, homogenous, isotropic, a single connected domain and have line electrodes on the periphery [107]. In addition, the contact size has to be sufficiently small to reduce the measurement corrections.

In this dissertation work, a Lake Shore 7500/9500 Series Hall System was used to perform Hall measurements on the samples at room temperature. The van der Pauw method was applied for the measurements. The samples have square geometry with contact size to sample periphery ratio as low as possible. In order to eliminate the persistent photoconductivity (PPC) relaxation effect on the transport properties, the samples were maintained in the dark for 12 h prior to performing Hall measurements. PPC effect has been observed in many III-V and II-VI compound semiconductors and can be explained by several theoretical models [108-110]. In many cases, PPC is attributed to the existence of deep defects such as DX centers which form when shallow

donors undergo a large lattice relaxation and convert to deep donors [108]. The difference in lattice relaxation between these two states results in a barrier that prevents the recapture of carriers into the stable state, thus yielding the PPC effect [109]. Other possible models include band-bending resulted from the interface leading to PPC effect and random local-potential fluctuation model inducing the separation of photoexcited carriers from traps and reduced recapture rate of carriers.

Photoluminescence

Photoluminescence (PL) refers to emission of light resulting from optical stimulation. The detection and analysis of this emission is widely used as an analytical tool due to its sensitivity, simplicity, and low cost [104]. When an electron increases energy by absorbing light there is a transition from the ground state to an excited state of an atom or molecule. This excited system does not have the lowest energy and has to return to the ground state. In luminescence materials the released energy is in the form of light, which is called as radiative transition. This emitted light is detected as photoluminescence, and the spectral dependence of its intensity provides information about the properties of the materials. Specially, photoluminescence of a semiconductor is related to both intrinsic and extrinsic defects in the material which usually create discrete electronic states in the bandgap and therefore influence the optical emission of the material.

PL can be performed both at room temperature and low temperatures. At room temperature, PL emission is thermally broadened. With decreasing temperature, PL peaks tend to be much sharper and the emission intensity is also stronger due to fewer nonradiative transitions. PL is normally useful for semiconductors which have direct

bandgap. However, at low temperatures, localized bound states and phonon assistance allow certain PL transitions to occur even in materials with indirect bandgap [104].

A He-Cd (325 nm) laser was used as the excitation source in room temperature PL measurements for the samples presented in this dissertation. The measurements were taken in a wavelength range of 340 to 800nm. A NESLAB chiller cooled GaAs PMT detector was used for UV up to ~900 nm.

X-ray Photoelectron Spectroscopy

X-ray photoelectron spectroscopy (XPS) is the most broadly applicable surface analysis technique today due to its surface sensitivity, quantitative and chemical state analysis capabilities [104]. All elements except for hydrogen and helium can be detected by using XPS. In XPS monoenergetic X-rays bombard a sample and cause photoelectrons to be ejected. Einstein photoelectric law in Equation (3-3) defines the relationship of the kinetic energy of the ejected photoelectrons and the binding energy of the particular electron to the atom.

$$KE = h\nu - BE \quad (3-3)$$

where KE is the kinetic energy of the photoelectron, $h\nu$ is the X-ray photon energy and BE is the binding energy. By measuring the photoelectron kinetic energy the characteristic binding energy of the electron in the atom can be determined. The depth of the solid samples varies from the top 2 atomic layers to 15-20 layers.

Perkin-Elmer PHI 5100 ESCA system was used to examine the chemical environment of P in P-doped ZnO and (Zn,Mg)O films. The base pressure of the XPS chamber was about 1×10^{-9} Torr after increasing the voltage to 15 kV and the power to 300 Watt. Both Mg and Al anodes were used to acquire XPS spectrums of different

samples. Argon gas sputtering to remove the sample surface contamination is necessary to obtain more accurate information about the film composition.

Current-voltage Measurement

Current-voltage (I-V) measurements were carried out at room temperature to characterize the performance of the devices including ZnO-based thin film transistors and (Zn,Mg)O/ZnO heterostructures. The electrical properties of ohmic contacts for Hall measurements were also examined. Semiconductor parameter analyzers Agilent 4155A and HP 4145B connected to a probe station were used in this dissertation work.

CHAPTER 4 DEVELOPMENT OF OXIDE-BASED THIN-FILM TRANSISTORS

Introduction

Display technologies based on organic/polymer light emitting diodes (OLED/PLED) are promising for providing lightweight, power efficient, flexible, high brightness performance. One challenge facing polymer light emitting devices is the thin-film transistors (TFTs) array control circuitry [111-116]. In active matrix displays, each pixel is programmed to provide a desirable current during the entire frame time, eliminating the issue of continuous increased current density encountered in the passive matrix approach. Figure 4-1 shows a schematic illustration of passive and active matrix displays. The light-emitting pixels in active matrix displays may be controlled by a thin film transistor array for much better brightness and efficiency. However, current opaque TFTs made with amorphous and poly silicon severely restrict the amount of light detected by observer. Depending upon the design of the array and interconnects, only a fraction of the emitted light is used by the observer of the information resulting in significant energy loss. In addition, TFTs based on amorphous Si have other limitations such as light sensitivity, light degradation and low field effect mobility ($\leq 1 \text{ cm}^2/\text{Vs}$) [11]. One method to overcome these problems is to utilize the recent progress in transparent oxides that are semiconducting to near-metallic.

Transparent conducting oxides (TCOs) can be regarded as a specific group of oxides exhibiting both high optical transmittance and electrical conductivity. There are many applications for TCOs such as transparent electrodes for flat-panel display and

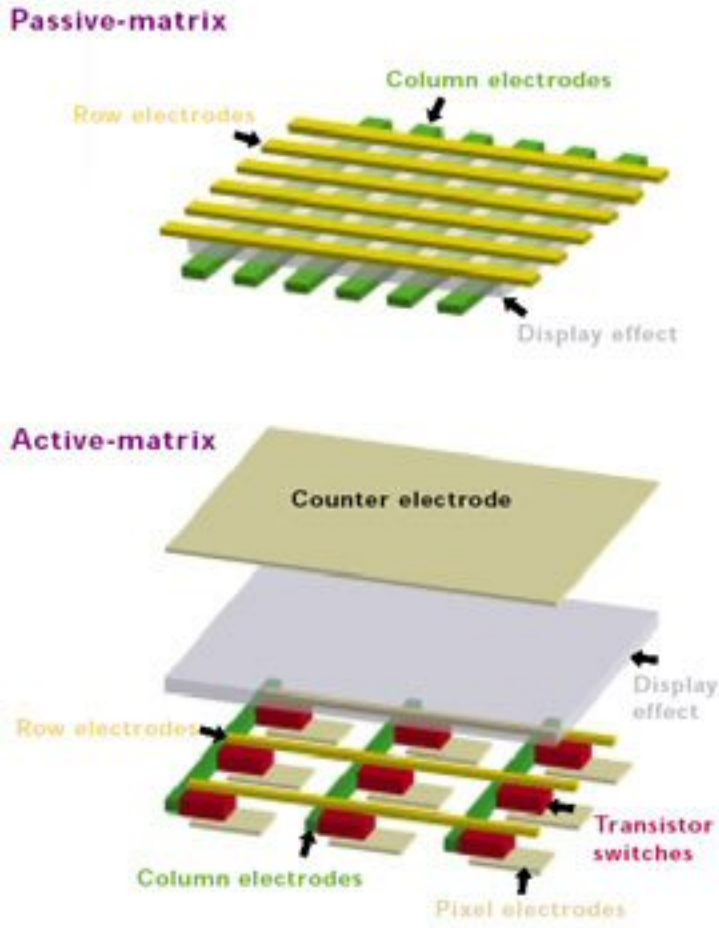


Figure 4-1. Schematic illustration of passive and active matrix displays [117].

solar cell, transparent electronic devices and selective window coatings in architecture.

N-type TCOs whose dominant carriers are electrons include indium tin oxide (ITO), SnO_2 , impurity-doped ZnO, CdO, as well as their related multicomponent oxides [117-

119]. As used for thin film transparent electrodes, TCOs should have a carrier

concentration of order of 10^{20} cm^{-3} or higher and bandgap above 3 eV [120]. With the

increasing need for transparent electrodes for optoelectronic devices, it is essential to

develop alternatives to ITO due to its expensive indium source. Ga- and Al-doped ZnO

with a resistivity on order of $10^{-5} \Omega \text{ cm}$ are promising candidates for thin film transparent

electrode applications [121]. In addition to binary compounds, ternary compounds such

as Cd_2SnO_4 , CdSnO_3 , CdIn_2O_4 , Zn_2SnO_4 , and CdSb_2O_6 have been developed to be used as n-type TCOs [120]. On the other hand, p-type TCOs such as CuAlO_2 , CuGaO_2 , and SrCu_2O_2 have been demonstrated recently [122-126], offering the promise of transparent two- and three-terminal devices. In fact, p-n junctions from n and p-type TCOs have been realized [124], establishing the feasibility of a transparent oxide bipolar transistor. With this development, the TFT and apertures could be replaced by a transparent TFT (TTFT) array with significant gain in the emitted light. This should significantly lower both the voltage and drive current required by the PLEDs. The sunlight readability and extended device lifetime can also be realized.

Transparent Semiconducting Oxides for Thin-Film Transistors

A distinction should be made between transparent semiconducting oxides (TSOs) and TCOs based on the different carrier densities for channel and interconnect performance. Table 4-1 lists the candidate materials, along with the range of electronic and photonic properties. For the channel layer, significant modulation of the channel conductance is needed to achieve field effect transistor (FET) switching. Thus, only moderate carrier densities (semiconducting behavior) are needed for the channel layer. On the other hand, TCOs' with high conductivity are needed for interconnects. Both of these materials are required to be highly transparent in the visible range of electromagnetic spectrum. There are two problems for TCOs or TSOs materials with marginal bandgaps for visible light transparency. First, the polycrystalline nature of the functional device introduces defects that extend the optical absorption into the bandgap. This reduces the efficiency of the devices, particular at the blue end of the spectrum where luminescence is weakest. Second, the optical absorption by the channel region can

lead to band-to-band excitations of carriers and subsequent shifting of transistor characteristics.

Table 4-1. Properties of transparent semiconducting oxides.

Material	Band gap	Resistivity (m Ω -cm)	Carrier density(cm ⁻³)	Mobility (cm ² V ⁻¹ sec ⁻¹)	Carrier type
ZnO	3.35 eV	0.5-100	10 ¹⁷ - 10 ²¹	200	n
ITO	3.6 eV	0.3-20	10 ¹⁸ -10 ²¹	10-40	n
Ag(In _{0.95} Sn _{0.05})O ₂	4.4 eV	10-10 ⁶	10 ¹⁹	0.47	n
ZnGaO ₄	4.4 eV	30-10 ⁵	n
CuGaO ₂	3.6 eV	10 ⁵	10 ¹⁸	0.46	p
(Co,Ni)O _x	3.8 eV	1-10 ⁶	10 ¹⁵ -10 ²⁰	0.5	p

Different channel materials can be considered for transparent TFT development.

Although most device applications of interest focus on inexpensive glass as the substrate of choice, experiments have also included epitaxial (on single crystals) channel materials in order to delineate the effects of crystallinity and grain boundaries on device performance. A key issue is to identify transparent materials that are suitable for use as channel materials in thin-film FET structures. Relevant factors include carrier density, carrier mobility, crystallinity, surface morphology, optical absorption, and photoconductivity over the visible spectrum. The latter is relevant to the stability of the TTFTs when coupled to PLED emitters. For TFT operation characteristics, enhancement-mode or “normally-off” is preferable to depletion-mode or “normally-on” due to lower power supply and simpler circuit design. Large off-current and the normally-on characteristics may originate from the fact that channel materials display high carrier densities resulting in a channel that will be conducting in the absence of applied field. Thus, the primary focus for TSOs has been on materials with higher electron mobility and easily controlled carrier densities.

ZnO-based Transparent Thin-film Transistors

ZnO has many characteristics that make it attractive to be used as an active channel layer in transparent TFTs. Due to its wide bandgap at room temperature ZnO is highly transparent in the visible spectrum. Thus, ZnO-based TFTs can realize increased aperture ratio of active matrix arrays and overcome the light sensitivity and degradation issues encountered with Si-based TFTs. Another particular interest in ZnO exists in the fact that good quality polycrystalline ZnO films with mobility ranging from 10 to 50 cm²/Vs can be realized at low temperatures (<500°C) on amorphous glass substrates or plastic/flexible substrates. The growth of ZnO thin films has been demonstrated using a number of deposition techniques, including sputtering, pulsed-laser deposition (PLD) and molecular beam epitaxy. In addition, ZnO can be processed by wet chemical etching making the device fabrication processing relative simple and low cost.

Transparent TFTs based on poly- and single crystalline ZnO films as active channel layers have been reported by several groups recently [127-131]. Hoffman *et al.* [127] fabricated an n-channel, enhancement-mode transparent TFT in which ZnO served as the channel layer with aluminum-titanium oxide (ATO) as the gate oxide, and ITO was used as the source, drain and gate. Rapid thermal anneal (RTA) process was used to increase the ZnO channel crystallinity and resistivity. The transfer characteristics of TTFTs indicated a maximum drain current on-to-off ratio of $\sim 10^7$ and the effective channel mobility ranged from 0.3 to 2.5 cm²/Vs. Masuda *et al.* [128] reported ZnO-based TFTs with a double layer gate oxide consisting of SiO₂ and SiN_x. The ZnO-TFT fabricated on Si substrate showed enhancement-mode operation. The drain current on-to-off ratio was more than 10⁵. The transparent ZnO-TFTs fabricated on glass substrate showed

depletion-mode characteristics. It is considered that the ZnO in the transparent device had rougher surface and more background electrons than the ZnO in the TFTs on Si substrates. The field-effect mobility μ_{FE} of the TFT device was $0.031 \text{ cm}^2/\text{Vs}$ which is much smaller than the Hall mobility of ZnO film. However, inserting a high carrier concentration layer between the channel layer and the source/drain contacts can increase μ_{FE} to $0.97 \text{ cm}^2/\text{Vs}$. This indicates that the high carrier concentration layer reduced the contact resistances and had a good effect on the theoretical drain current [128].

In plastic/flexible electronics, the processing temperatures are limited to be less than 100°C . Although organic semiconductors can be the material choices, their low mobility ($<0.1 \text{ cm}^2/\text{Vs}$) and instability in ambient conditions impede the further applications for TFTs. TFTs employing ZnO as a channel layer have been realized at room temperature with higher mobility and current on/off ratio. Carcia *et al.* [129] fabricated ZnO TFTs by rf magnetron sputtering on Si substrates near room temperature. The best devices had μ_{FE} of more than $2 \text{ cm}^2/\text{Vs}$ and an on/off ratio $> 10^6$. Fortunato *et al.* [130] also reported high performance ZnO TFTs fabricated at room temperature. The devices operated in the enhancement mode with a saturation mobility of $27 \text{ cm}^2/\text{Vs}$ and an on/off ratio of 3×10^5 . The ZnO films with very high resistivity of about $10^8 \Omega \text{ cm}$ were deposited by using rf sputtering for the TFT devices. Highly conductively Ga-doped ZnO was used as the source and drain electrodes.

In this dissertation work, the development of ZnO-based TFTs with transparent conducting oxides as the source/drain is presented. Specifically, the fabrication process of these top-gate type TFT devices on glass substrate is described. Three types of active

channel materials including undoped ZnO, P-doped ZnO and (Zn,Mg)O films were employed in the TFTs. The primary interest is TFT devices that operate in enhancement mode exhibiting a normally off (gate voltage $V_g = 0$) channel state. The output and transfer characteristics of the TFT devices using different channel materials are also discussed.

Deposition and Properties of Channel Materials

Pulsed laser deposition was used to deposit the ZnO films as the channel layer in TFTs. A KrF excimer laser ($\lambda = 248$ nm) was used as the ablation source. A laser repetition rate of 1 Hz was applied, with a laser pulse energy density of 1-3 J/cm². The dependence of film properties on deposition conditions for undoped ZnO was investigated for the films grown at 400° C in an oxygen pressure ranging from 2mTorr to 300mTorr. Corning 7059 glass substrate (1cm x 1cm) was used as the film growth substrate. The thickness of the films is in the range of 400-500 nm. 2 at.% P-doped ZnO and (Zn_{0.9}Mg_{0.1})O thin films were also utilized as the channel materials for TFTs. Post-growth annealing process was carried out in chamber at 600° C and 100 Torr oxygen pressure for 1 hr for all the films. Previous results showed that this annealing process for P-doped ZnO and (Zn,Mg)O films can further reduce the native electron density by introducing an acceptor level from phosphorus substitution [91].

The electrical properties (carrier concentration, Hall mobility and resistivity) of the undoped polycrystalline ZnO films as a function of oxygen pressure are shown in Figure 4-2 [131]. Note that all of the films are deposited on bare glass and post-annealed at 600°C in 100 Torr oxygen. For films deposited at $P(O_2) = 20$ mTorr, a Hall mobility of 26 cm² V⁻¹s⁻¹ was realized. With increasing oxygen pressure, the n-type carrier

concentration steadily decreases. This behavior reflects suppressed oxygen vacancies and/or Zn interstitials which contribute to the intrinsic electrons in ZnO as growth pressure increases. It is necessary to decrease the background electron density of the ZnO films as the active channel layer and also desirable to maximize the mobility of the channel layer. Therefore, 400°C and 20 mTorr oxygen pressure were chosen to grow ZnO films for TFTs.

Crystallinity is an important factor in determining the transport properties of the channel material. One interesting aspect of ZnO is its strong tendency to maintain uniaxial texture in polycrystalline films deposited on almost any substrate. Figure 4-3 shows an XRD pattern of an undoped ZnO film grown on a glass substrate at $P_{O_2}=20\text{mTorr}$. The (002) and (004) ZnO diffraction peaks are predominant indicating c-axis orientation in this polycrystalline film. However, this uniaxial texture does not eliminate grain boundaries. Figure 4-4 shows an AFM image of the ZnO film growth under the conditions described above. Grain size is on the order of 100-150 nm. In a field-gated structure, the effect of grain boundary conductance and charge density has to be considered in order to model the field-effect characteristics.

Fabrication of ZnO-based TFTs

Top-gate type TFTs using ZnO as the active channel layer were realized using photolithography followed by wet chemical etching processing. A schematic cross section view of a top-gate type TFT structure is shown in Figure 4-5. Amorphous gate oxides (Ce,Tb)MgAl₁₁O₁₉ (CTMA) and HfO₂ were grown by PLD and sputtering, respectively. Tin-doped indium oxide (ITO) served as the source and drain electrodes due to its low resistivity ($\sim 2 \times 10^{-4} \Omega \text{ cm}$) and high transparency in the visible spectrum.

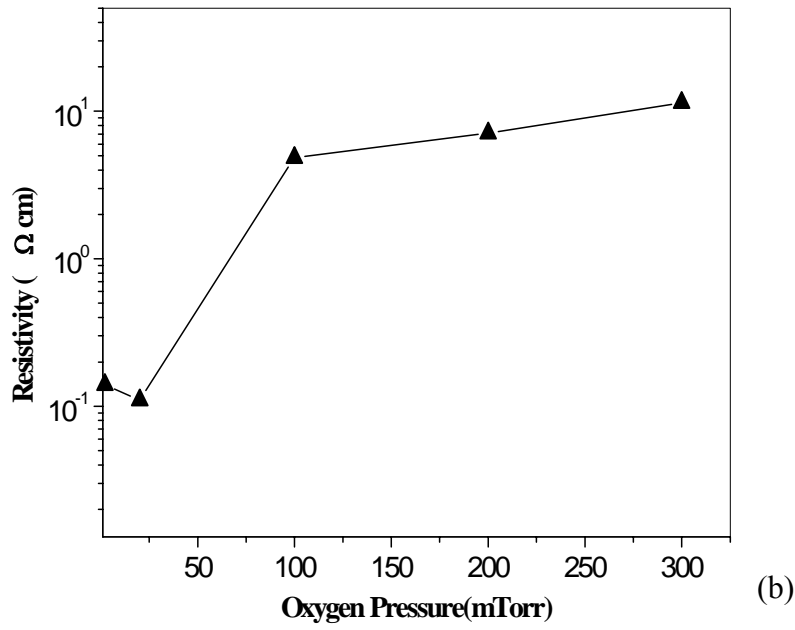
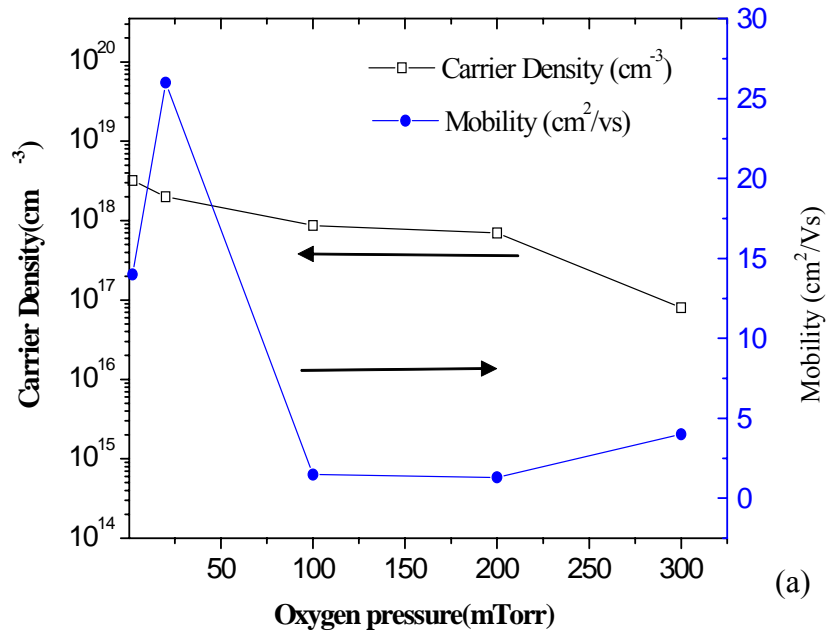


Figure 4-2. Electrical properties of undoped ZnO thin films grown on glass at 400°C as a function of oxygen pressure. Plots showing (a) carrier density, mobility, and (b) resistivity of the films.

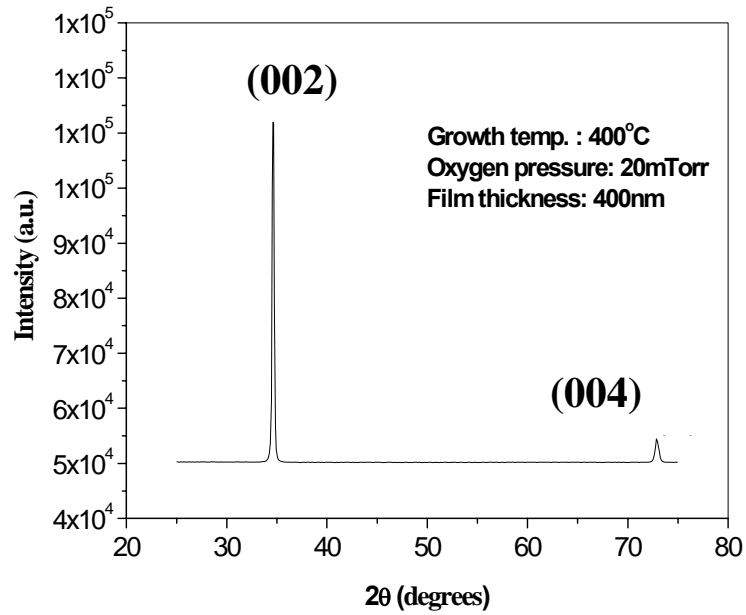


Figure 4-3. X-ray diffraction pattern of the undoped ZnO film deposited at $P_{O_2}=20\text{mTorr}$ on glass substrate.

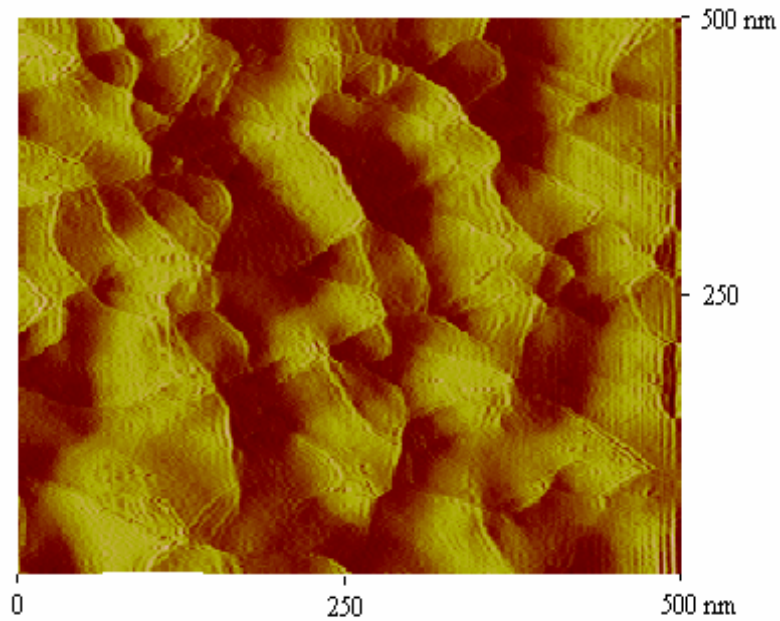


Figure 4-4. An AFM image of the surface of the undoped ZnO thin film deposited at $P_{O_2}=20\text{mTorr}$ on glass substrate.

There are several reasons why buried-channel structure is chosen: (1) the buried channel device is expected to have higher mobility because in bulk conduction the surface scattering can be avoided [132]; (2) the active channel layer is protected from ambient by the gate oxide layer, thus the channel layer can be made thinner in order to reduce the potential parallel resistance; (3) the source and drain electrodes make direct contact with the channel material at the gate oxide/channel interface eliminating the potential series resistance [133].

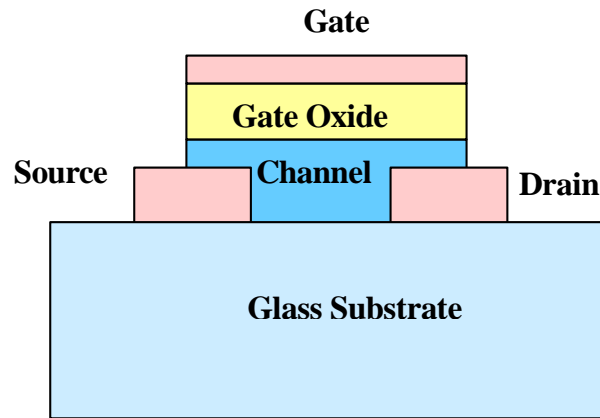


Figure 4-5. Schematic cross section view of a top-gate-type TFT structure.

Standard photolithography process had been used to fabricate the ZnO-based TFTs in this dissertation work. Positive photoresist (Shipley 1813) was chosen due to the requirements of the available photoresist masks. Uniform application of photoresist was accomplished by spinning the resist on the sample substrates. The final thickness of the photoresist film depends on the spin rate and spin time. In this work, a uniform photoresist layer with thickness of about 800-1000 nm was obtained by setting spinning speed at 5500 RPM for 30-40 sec. Samples with different photoresist thicknesses were also investigated in order to obtain the optimal exposure and development conditions for

the best resolution of the patterns. Before being exposed to UV light the photoresist was soft-baked at 90°C in air for 45 min.

The resist-coated samples were then contacted with a photoresist mask and exposed to light. Karl Suss mask aligner which has a mercury (Hg) UV lamp was used to expose photoresist and align the drain electrodes with those of source and drain. After the exposure, the sample was treated with a developing solution. The exposure and development time for certain thickness of photoresist depend on the exposure UV light intensity which may decrease during the extended usage of the UV lamp. Therefore, the actual intensity of UV light had to be measured to determine and adjust the exposure and development conditions.

The photoresist pattern obtained by the development was used as a mask for the etching of the underlying layers. In the ZnO-based TFTs fabrication scheme, wet chemical etching was utilized for the mesa isolation and the pattern formation of source, drain and gate. Compared to dry etching, wet etching has several advantages such as high selectivity, less damage to the underlying material and cheap system setup. During wet etching, the slowest step, called the rate limiting step, determines the etch rate. Generally, there are two types of rate limiting step in wet etching: diffusion-limited and reaction-limited. In diffusion-limited etching mode, the etch depth has a square root dependence on etch time and the solution agitation significantly affects the etch rate. The solution has to be agitated in some manner to assist in the movement of etchant to the surface and the removal of the etch product. On the contrary, in reaction-limited etching, the etch depth has a linear dependence on etch time and the etch rate is independent of solution agitation.

Since it is desirable to have a reproducible and well controlled etch rate for device fabrication, the reaction-limited etching is more preferable to the diffusion-limited mode.

In this work, wet etching of the materials employed in the TFT structure has been investigated by using different acid solutions including H_2SO_4 , HCl , HNO_3 , H_3PO_4 , HF as well as the mixtures of these acids. To realize this top-gate TFT structure high selectivity of gate, gate oxide and channel layers over underlying source/drain layer is required. It was found that among these etchants H_3PO_4 has the best resolution for the gate metal and the highest selectivity of gate oxide and channel layers over underlying ITO. For the etching of ITO source and drain, HCl acid was found to have the best etching results. Stylus profilometer was used to measure the film thickness in order to calculate the etch rate after the removal of photoresist mask in acetone. In the same time, the etch bias resulting from the isotropic wet etching can be observed and minimized by optimizing the temperature of acid solution and the etching time.

Figure 4-6 schematically illustrates the fabrication processing sequence for the ZnO-based TFT structure. The initial substrate is commercial ITO-coated display glass substrate. First, the ITO source and drain patterns were defined via using photolithography process, with wet etching of the ITO performed in HCl acid at around 35°C . The dependence of etch depth on etch time showed a linear relationship, indicating the etching process was reaction-limited. After removing the source/drain photoresist patterns in acetone, ZnO was then deposited at 400°C in 20 mTorr oxygen as the active channel layer on the ITO patterned glass substrate. The thickness of channel layer was in the range of 20-50nm. A thin layer of gate oxide (100-200 nm) was deposited on top of the ZnO channel layer. Then aluminum as the gate metal ($\sim 100\text{nm}$) was deposited by

using magnetron rf sputtering at room temperature. The gate contact was defined via using lithography alignment followed by selective wet etching gate metal (Al), gate oxide and channel layers with H_3PO_4 acid down to the source and drain contacts. Aluminum deposited by sputtering can be easily etched by H_3PO_4 at $\sim 60^\circ\text{C}$ with a well-controlled profile. Etching of gate oxide and ZnO films without removing the underlying ITO layer as well as the glass substrate was realized in H_3PO_4 acid at moderate temperatures (35-40 $^\circ\text{C}$). Thus, etching this top-gate TFT structure by using H_3PO_4 acid with high selectivity made the device fabrication process much simpler and more controllable.

Top-view microscopy images of the ZnO-TFT devices on glass substrate are shown in Figure 4-7 (a) and (b). Top-gate type TFT structures with well-defined contact patterns were realized by using photolithography and wet etching. Devices with different channel widths and lengths were fabricated as shown in Figure 4-7 (a). For the device shown in Figure 4-7 (b), the channel length and width are 50 μm and 90 μm , respectively.

In order to field gate this structure, it is necessary to form either a Schottky barrier or gate oxide. For ZnO, Schottky barriers are low and are apparently unsuitable for field gated rectifying structures. For oxide gates, the gate dielectric must be chosen to have a band offset with the channel material so as to avoid carrier injection into the conduction band and/or valence band of the gate insulator. For wide bandgap semiconductors, such as ZnO, this necessitates the use of the larger bandgap oxides and precludes the use of many insulators being considered for field gated structures on other semiconductors. $(\text{Ce,Tb})\text{MgAl}_{11}\text{O}_{19}$ (CTMA) with wide bandgap ($>5\text{ eV}$) was used as the gate dielectric for the TFT. Low leakage current about 10^{-7} A cm^{-2} was obtained for a 200 μm diameter Al-CTMA-ZnO capacitor [131].

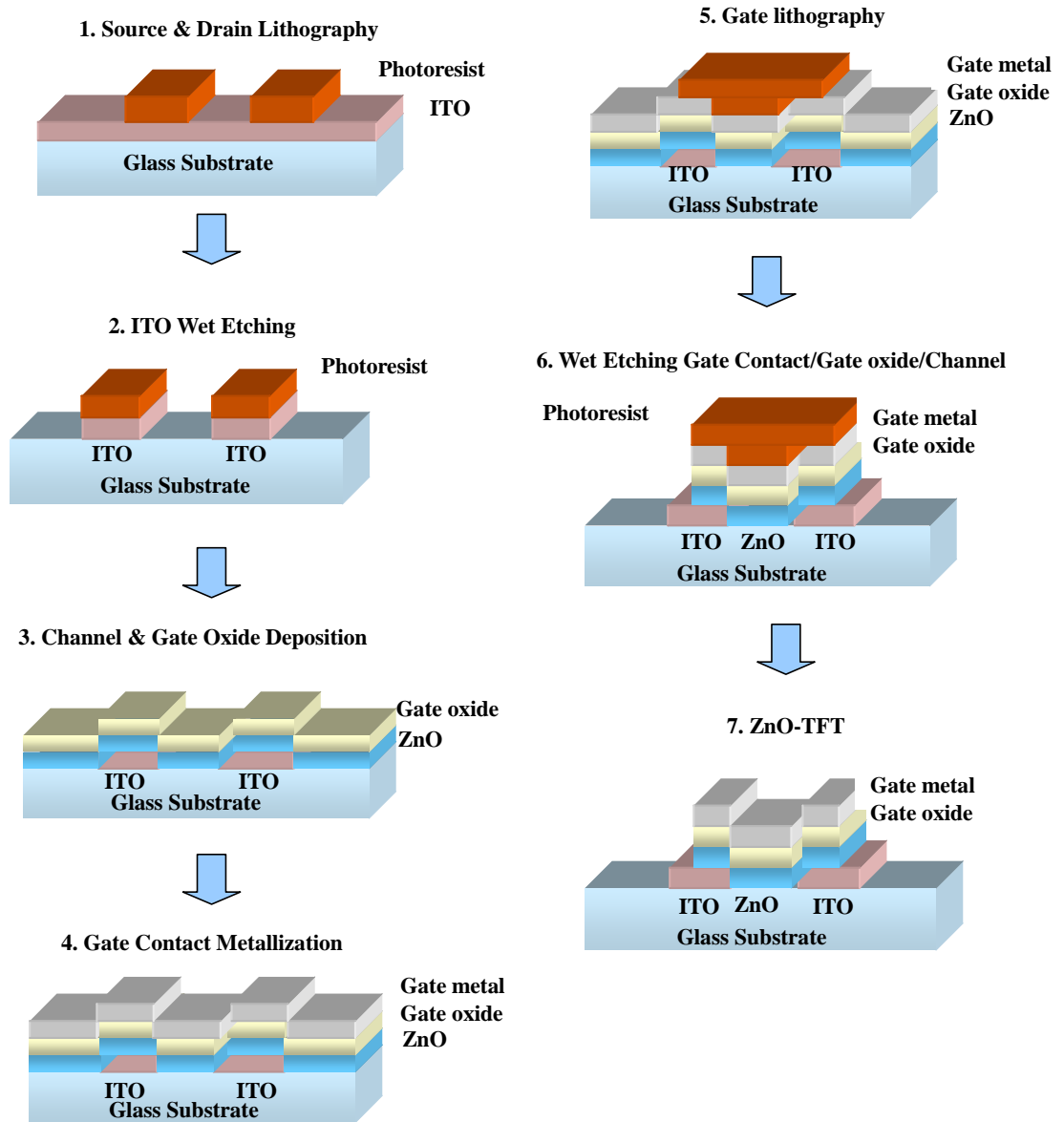


Figure 4-6. Schematic fabrication sequence of ZnO-based TFT structure.

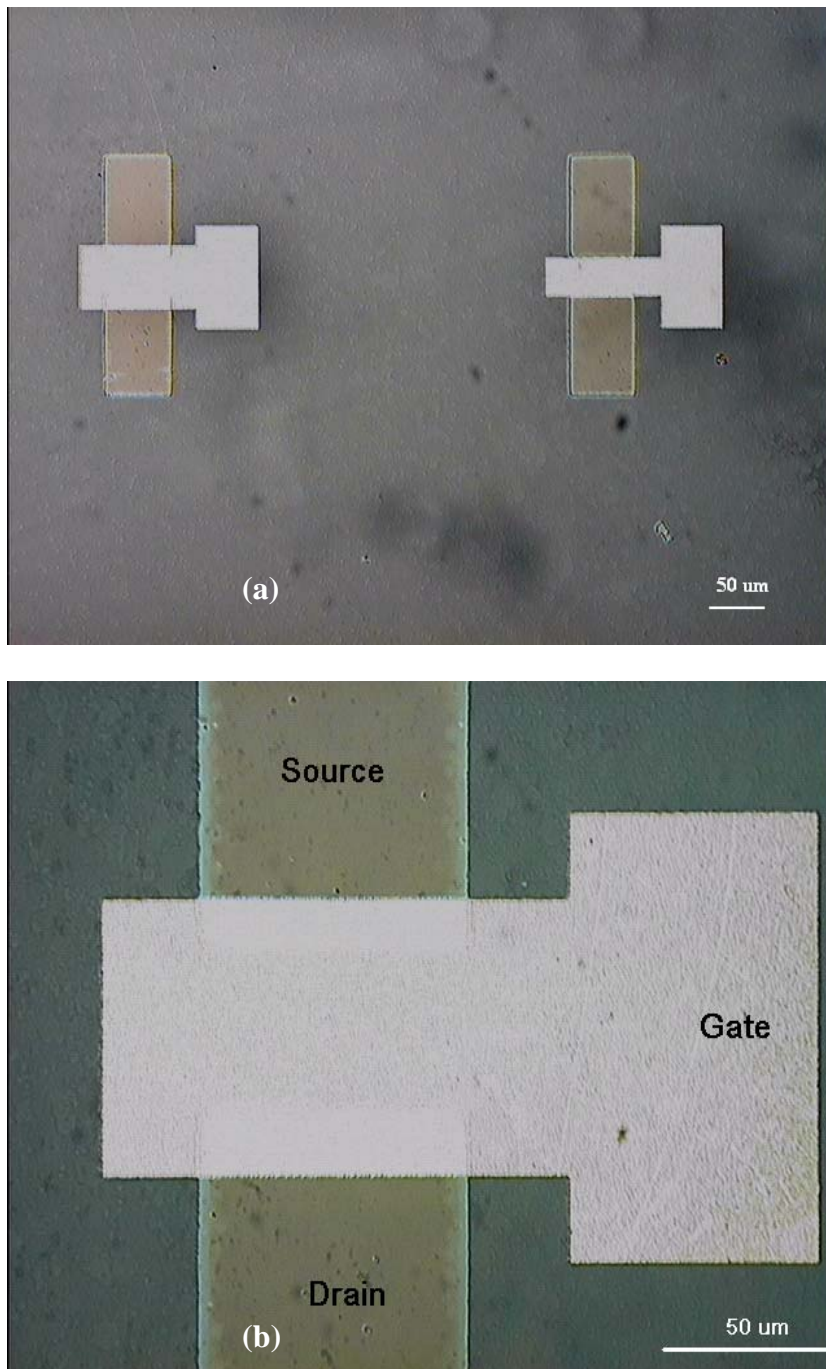


Figure 4-7. Top-view microscopy image of the ZnO-TFTs on glass substrate.

ZnO-based TFT Device Characterization

We characterized the output and transfer performance of the TFT devices using an Agilent 4155A Semiconductor Parameter Analyzer at room temperature. The transfer

characteristics of the devices include drain current I_d and gate current I_g as a function of gate voltage V_g at a fixed drain voltage V_d , drain current on-and-off ratio (I_{ON}/I_{OFF}) and field-effect mobility. When the current carriers are confined within a narrow channel layer additional scattering mechanisms have to be considered. The location of the carriers at the oxide-semiconductor interface introduces additional scattering mechanisms like Coulomb scattering from oxide charges and interface states, as well as surface roughness scattering. Generally, field-effect mobility can be obtained both from the transconductance value and from the saturation current. In field-effect transistors, transconductance is defined by [134]

$$g_m = \left. \frac{\partial I_{DS}}{\partial V_{GS}} \right|_{V_D} \quad (4-1)$$

The field-effect mobility μ_{FE} is given by

$$\mu_{FE} = \frac{Lg_m}{WC_{OX}V_{DS}} \quad (4-2)$$

Where L is the channel length, W is the channel width, C_{OX} is the capacitance of gate oxide, V_{DS} is the source-drain voltage. The turn-on voltage need not be known for the determination of μ_{FE} . Another way to calculate field-effect mobility is fitting straight line to the plots of the square root of drain current vs gate-drain voltage, while the drain current in the saturated region, $I_{d_{sat}}$ is given by [128]

$$I_{d_{sat}} = \left(\frac{W}{2L} \right) \mu_{FE} C_i (V_{GS} - V_{th})^2 \quad (4-3)$$

$(V_{ds} > V_{gs} - V_{th})$

Where C_i is the capacitance per unit area of the gate oxide.

ZnO-TFTs Using Undoped ZnO as Active Channel Layer

The electrical characteristics of the TFT device with undoped ZnO as the channel layer are shown in Figure 4-8. For this device structure, the ZnO film thickness was 20nm. This TFT device operated as an n-channel, normally-on device, as evident from the fact that there was a source-drain current at the gate voltage of 0V and a negative voltage was required to deplete the carriers in the channel layer. Note that the device drain currents I_{DS} are large, of order of mA, in its “ON” state is due to the high carrier concentration in the undoped ZnO channel layer. To further modulate and deplete the channel conductance, low channel carrier density is necessary to achieve.

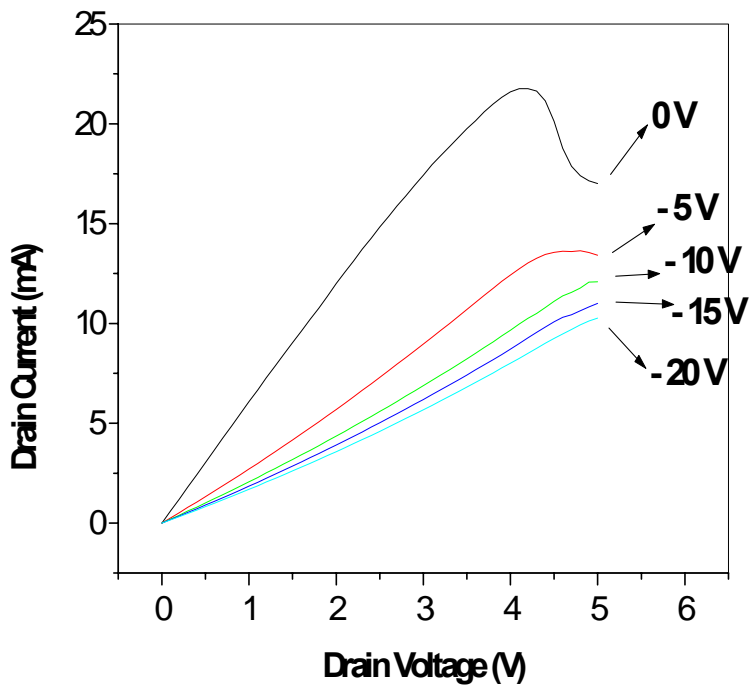


Figure 4-8. Drain current as a function of drain voltage characteristics for the undoped ZnO-TFT.

ZnO-TFTs Using P-doped ZnO and (Zn,Mg)O as Active Channel Layer

For efficient TFT operation, an enhancement-mode device is preferable over depletion-mode, thus avoiding the need to apply voltage in order to turn the device off. Much less power dissipation is possible when normally-off, enhancement-mode devices are employed. For this motivation, alternative channel materials have been investigated in order to decrease carrier density. Phosphorus-doped ZnO and (Zn,Mg)O have been deposited as the active channel layer for the TFT. Post-deposition oxygen annealing processes were used to further decrease the electron density in these films. Figures 4-9 (a) and (b) show the output characteristics of devices with P-doped ZnO and (Zn,Mg)O (50 nm for both) as the channel materials, respectively. For P-doped ZnO based TFT, the device has the same depletion-mode operation as the undoped ZnO one. However, the channel conductivity is lower than that of TFT with undoped ZnO as the channel at the gate voltage of 0V.

Enhancement-mode operation (Figure 4-9 (b)) was realized for P-doped (Zn,Mg)O based TFTs with HfO₂ serving as the gate dielectrics. In these devices conducting channels were induced by applying positive gate voltages. Channel length and width were 20 μ m and 90 μ m, respectively. A saturation of I_{DS} (pinch-off) was observed for small values of V_{DS}. This pinch-off behavior indicates that the channel layer is sufficiently depleted in this TFT. The field-effect (FE) mobility was derived to be about 5.32 cm² V⁻¹ s⁻¹ from the transfer characteristics of the devices operated at 6V shown in Figure 4-10. This value is comparable to that realized in undoped ZnO channels indicating that acceptor doping did not have a detrimental impact on channel mobility. We also determined the carrier density was as low as 3.9x10¹⁶ cm⁻³ for this channel

material, which is two orders lower than that in the undoped ZnO thin film. The on/off current ratio is on the order of 10^3 at the gate voltage of 10V for these devices.

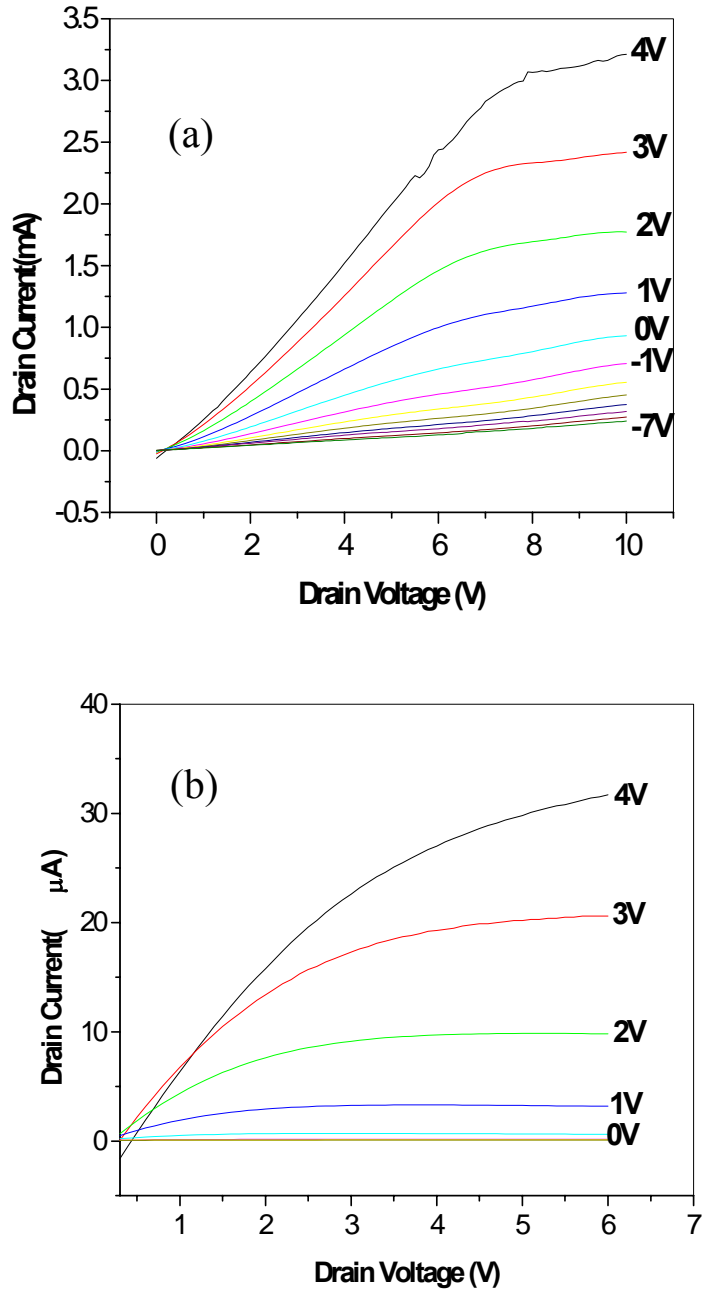


Figure 4-9. The output characteristics of the TFT with alternative active channel materials: (a) P-doped ZnO as the channel; (b) P-doped (Mg,Zn)O as the channel.

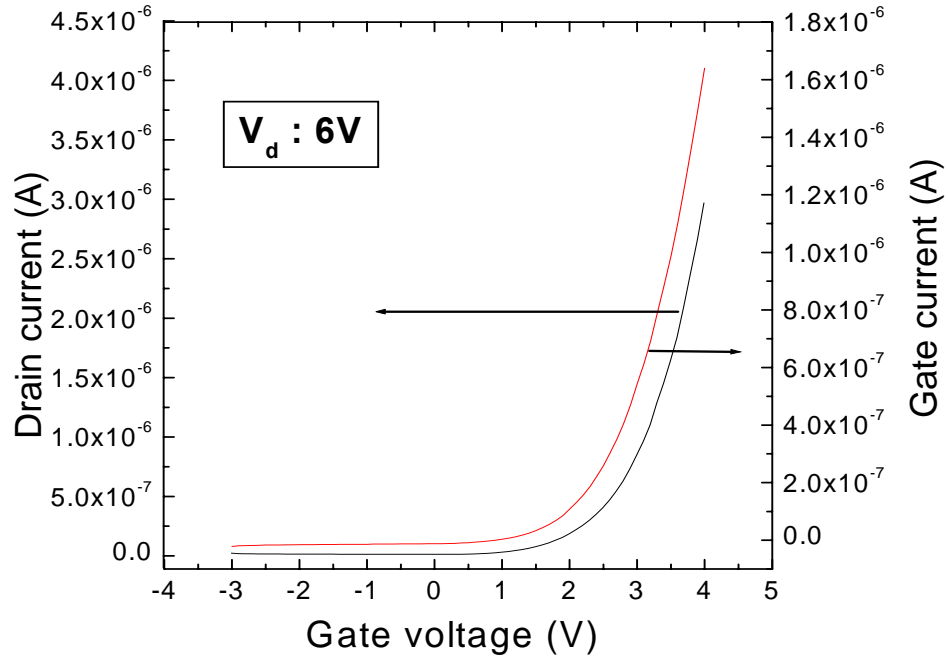


Figure 4-10. Transfer characteristics of ZnO-TFT with P-doped (Zn,Mg)O as the channel layer at the drain voltage of 6V.

CHAPTER 5
GROWTH AND CHARACTERIZATION OF P-TYPE PHOSPHORUS-DOPED
(Zn,Mg)O BY PULSED LASER DEPOSITION

Introduction

One of the critical issues in developing ZnO-based UV LEDs and lasers is to realize low resistivity, high carrier density p-type ZnO material. Phosphorus is a possible acceptor dopant that can be used to synthesize p-type ZnO. Doping of ZnO with Mg provides a means to increase the band gap further into the UV. The motivation for examining phosphorus doping in Mg-doped ZnO is two-fold. First, p-type conductivity in (Zn,Mg)O films will be necessary for LED heterostructures in which carrier confinement for efficient electron-hole recombination is needed. Second, the addition of Mg shifts the conduction band edge to higher energy, perhaps increasing the activation energy of the defect donor states. Previous results on annealed phosphorus-doped (Zn,Mg)O device structures, in particular C-V and I-V characteristics, indicate that phosphorus yields an acceptor state and p-type behavior [135]. However, these materials did not yield an unambiguous positive Hall voltage, presumably due to the low mobility and high carrier compensation.

In this chapter, an unambiguous positive Hall coefficient in as-grown P-doped (Zn,Mg)O films is presented. The effect of oxygen partial pressure on the transport properties of P-doped (Zn,Mg)O films grown on low-temperature (LT) undoped ZnO buffer layers is described. The chemical state of phosphorus in p-type (Zn,Mg)O:P films

is presented. The crystallinity and the surface morphology of these films are also discussed.

Experimental

The phosphorus-doped ($\text{Zn}_{0.9}\text{Mg}_{0.1}\text{O}$) epitaxial films were grown via pulsed laser deposition (PLD) on *c*-plane sapphire substrates. The target was fabricated using high-purity ZnO (99.9995%) and MgO (99.998%), mixing with P_2O_5 (99.998%) as the doping agent. The melting point and boiling point for P_2O_5 are about 340°C and 360°C, respectively. P_2O_5 has a lower heat of formation ($H_f = -360$ Kcal/mole) compared with that of SiO_2 ($H_f = -202.6$ Kcal/mole) [136]. The phosphorus doping level in the target was 2 at.%. A KrF excimer laser ($\lambda = 248$ nm) was used as the ablation source. A laser repetition rate of 1 Hz was applied, with a laser pulse energy density of 1-3 J/cm². The ZnO growth chamber has a base pressure of 10⁻⁶ Torr. An undoped ZnO buffer layer (~50nm) was initially deposited at 400°C and 20mTorr oxygen partial pressure before the growth of P-doped ($\text{Zn}_{0.9}\text{Mg}_{0.1}\text{O}$) films. The undoped ZnO buffer layer was post-annealed at 650°C in flowing O₂ for 1h in order to decrease the electron conductivity. Semi-insulating buffer layers are preferable in order to perform Hall measurements without influence from buffer layer conduction. The phosphorus-doped ($\text{Zn}_{0.9}\text{Mg}_{0.1}\text{O}$) films were then deposited on the annealed undoped ZnO buffer layer at a substrate temperature of 500°C under oxygen partial pressure ranging from 20 mTorr to 200 mTorr. The total film thickness ranged from 500 to 700 nm.

Four-point Van der Pauw Hall measurements were performed at room temperature in order to examine the transport properties of the as-grown P-doped ($\text{Zn}_{0.9}\text{Mg}_{0.1}\text{O}$) films. The chemical state of phosphorus in the films was examined by using XPS with an Al

anode (photon energy = 1486.6 eV). The film crystallinity and surface morphology of the P-doped ($\text{Zn}_{0.9}\text{Mg}_{0.1}\text{O}$) films as a function of oxygen growth pressure were also investigated by using XRD and AFM, respectively.

Results and Discussion

The large lattice and thermal mismatch between ZnO and sapphire substrate will generate considerable stress in the epitaxial film, affecting the growth and quality of the film. To optimize the crystallinity and properties of the epitaxial films, a well-created buffer layer is necessary. Kaidashev *et al.* [137] reported that by inserting a thin ZnO relaxation layer grown at lower temperature between sapphire substrate and high-temperature ZnO film the crystallinity and mobility of the films have been improved. In this work, a thin layer of LT-ZnO was grown at 400°C on sapphire substrate before the growth of P-doped ZnMgO film. The effect of the LT-ZnO buffer layer on crystallinity of P-doped ($\text{Zn}_{0.9}\text{Mg}_{0.1}\text{O}$) films were investigated by measuring the omega rocking curve for ZnO (0002) plane. Figure 5-1 shows the ZnO (0002) omega rocking curves of the P-doped ($\text{Zn}_{0.9}\text{Mg}_{0.1}\text{O}$) sample with and without a LT-ZnO buffer layer. These films were grown at 500°C and under 20 mTorr oxygen pressure. An increase in diffraction intensity is clearly shown for the film grown with LT-ZnO buffer layer. The full-widths at half maximum (FWHM) values of the omega rocking curve are 0.83° and 1.02° for the films grown with and without buffer layer, respectively, indicating that the crystallinity was improved by introducing a thin LT-ZnO buffer layer. Thus, by applying a thin layer of LT-ZnO buffer layer, the properties of the P-doped ZnMgO films were expected to be optimized.

For many samples, a persistent n-type photoconductivity was observed that complicated the transport characterization. To eliminate the photoconductivity relaxation effect on the transport properties, the samples were maintained in the dark for 12 hours before performing Hall measurements at room temperature. Using this procedure, the carrier density and conduction type of as-grown P-doped $(\text{Zn}_{0.9}\text{Mg}_{0.1})\text{O}$ films was determined. These properties as a function of oxygen growth pressure are shown in Figure 5-2. Each sample was measured a minimum of twenty times to obtain the average results shown here. The error bars represent the maximum deviation from the average values. Note that films deposited at the oxygen partial pressure lower than 100 mTorr show n-type conductivity with electron concentration in the range of 10^{16} - 10^{17} cm^{-3} . However, as oxygen pressure increases above 100 mTorr, the electron concentration continuously decreases and the samples started showing indeterminate carrier type indicating the coexisting of electrons and holes in the films.

Unambiguous conduction type was not observed for the samples grown at 100 and 120 mTorr due to near-equivalent concentrations of holes and electrons in the films. When the oxygen partial pressure was increased to 150 mTorr during the film deposition, the Hall-effect data showed consistent p-type carrier type with a hole concentration of 2.7×10^{16} cm^{-3} . Also note that as the oxygen partial pressure was increased up to 200 mTorr, the films reverted to an indeterminate carrier type. Figure 5-3 shows the carrier mobility carrier type films grown under 100, 120 and 200 mTorr oxygen pressure yield large of P- doped $(\text{Zn}_{0.9}\text{Mg}_{0.1})\text{O}$ films as a function of oxygen pressure. The indeterminate standard deviations compared with those with unipolar conduction type films. These results imply that for the samples which may contain both types of carriers,

more attention needs to be paid for the Hall measurements and data analysis. The p-type films grown at 500°C and 150 mTorr oxygen show an average hole mobility of 8.2 cm²/Vs at room temperature. This mobility value is reasonable compared with the ones reported in the previous studies on N, Al-N and P-doped p-type ZnO.

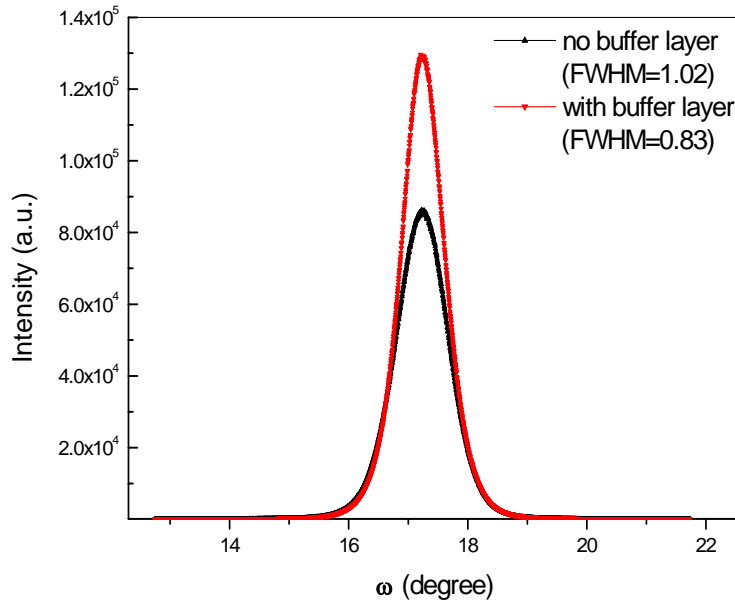


Figure 5-1. ZnO (0002) omega rocking curves of P-doped ($Zn_{0.9}Mg_{0.1}$)O samples with and without LT-ZnO buffer layer.

The resistivity of the P-doped ($Zn_{0.9}Mg_{0.1}$)O films grown under different oxygen pressures are also shown in Figure 5-4. The resistivity of the films increases from 1.0395 Ω -cm to 350.5 Ω -cm as oxygen growth pressure increases from 20 to 100 mTorr. The increase in resistivity for the films grown under oxygen pressure between 20 to 100 mTorr results from the decreased carrier concentration in the films. The films grown at 100 mTorr exhibit the highest resistivity of about 300 Ω -cm. With further increasing oxygen pressure, resistivity rapidly decreases due to the increased hole carrier conduction

in the films. For the p-type P-doped ($\text{Zn}_{0.9}\text{Mg}_{0.1}\text{O}$) films grown at 150 mTorr oxygen pressure, the resistivity is about $35 \Omega\text{-cm}$.

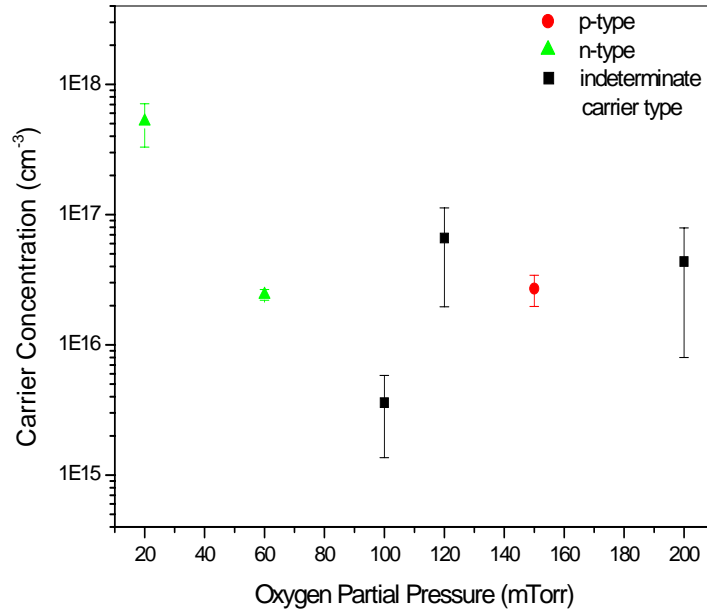


Figure 5-2. Carrier concentration and carrier type in P-doped ($\text{Zn}_{0.9}\text{Mg}_{0.1}\text{O}$) films as a function of oxygen partial pressure.

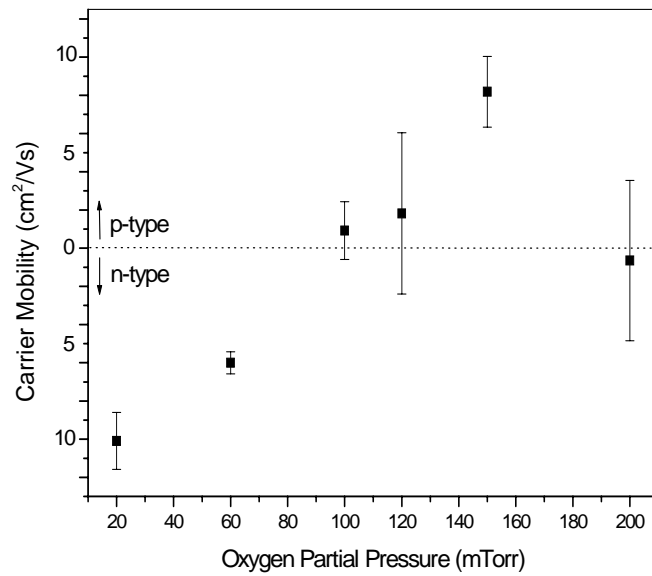


Figure 5-3. Effect of oxygen partial pressure on carrier mobility of P-doped ($\text{Zn}_{0.9}\text{Mg}_{0.1}\text{O}$) films.

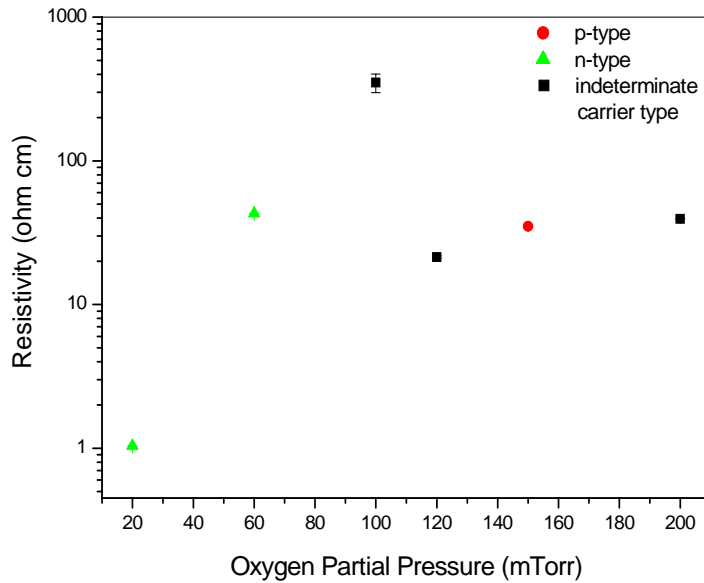


Figure 5-4. Resistivity of P-doped ($\text{Zn}_{0.9}\text{Mg}_{0.1}\text{O}$) films vs oxygen partial pressure.

The Hall effect results show that p-type doping in P-doped ($\text{Zn}_{0.9}\text{Mg}_{0.1}\text{O}$) films is strongly dependent on the oxidation conditions. It is important to note that the effect of oxygen partial pressure on ZnO p-type conduction has been investigated previously by both experiment and theory. Xiong *et al.* [138] reported evidence for p-type conduction in undoped ZnO films grown at high oxygen partial pressure by reactive sputtering. A change in the sign of charge carriers from electrons to holes was identified around 55% oxygen in Ar/O₂ mixture. ZnO-based *p-n* homojunction was also formed by controlling oxygen partial pressure during sputtering. This realization of p-type conductivity in undoped ZnO was consistent with the effect of higher chemical potential of atomic oxygen on defect formation enthalpies. The increased oxygen chemical potential by electronic excitation to a dissociated state raises the formation enthalpy of the intrinsic donor V_{O} and lowers the formation energy of the acceptor O_{i} .

Zunger also suggested several theoretical practical rules for p-type doping of wide bandgap materials to overcome the doping bottlenecks [76]. First, the p-type doping is facilitated by alloying an element that leads to upward bowing of the VBM. One way to shift the VBM upwards is to add a tetrahedrally bonded 3*d* element with active *d* states. In addition, Zunger suggests that limitations to p-type doping can be overcome by manipulating the growth conditions, e.g. the use of the host anion-rich growth conditions to inhibit the formation of so-called “hole killer” defects. Calculations from chemical potentials suggest that the enthalpy of forming anion vacancies decreases under cation-rich (zinc-rich) conditions. In the present study, the growth condition necessary to obtain p-type P-doped ($\text{Zn}_{0.9}\text{Mg}_{0.1}\text{O}$) films is rather narrow (150 mTorr oxygen partial pressure). For the samples grown in the oxygen pressures of 100, 120, and 200 mTorr, the Hall-effect results do not show unambiguous p-type conductivity. The observation of indeterminate carrier type for a growth pressure of 200 mTorr may be explained by the “host anion poor” rule for the anion-substituting p-type dopants which conjectures that anion poor conditions are more favorable for a high solubility of acceptors on anion sites [76]. Consequently, the host anion condition has to be optimized in order to reach an equilibrium state under which p-type doping of ZnO can be realized.

In order to confirm the incorporation of P_2O_5 as a P doping source in the p-type films, X-ray photoelectron spectroscopy was performed to examine the chemical states of phosphorus using Al anode as the X-ray source. Figure 5-5 shows the XPS survey of P-doped $\text{ZnMg}_{0.1}\text{O}$ films grown at 500°C, 150 mTorr oxygen pressure. Zn 2*p*, Mg 1*s* and O 1*s* peaks as well as their Auger peaks are shown in the spectrum. The multiplex of P 2*s* is shown in Figure 5-6. Only one peak with the binding energy of 192.2 eV is observed

from the spectrum, which is consistent with P 2s binding energy of 192.8 eV in P₂O₅. The P 2s peaks regarding to Zn₃P₂ and element phosphorus state have the binding energy values of 186.3 eV and 187.7 eV, respectively [139].

X-ray diffraction was used to examine the crystallinity of the P-doped (Zn_{0.9}Mg_{0.1})O films grown under different oxygen partial pressures as shown in Figure 5-7. The diffraction data shows only ZnO (0002) and (0004) and sapphire (0006) peaks indicating that the films are oriented only with *c*-axis perpendicular to sapphire substrates. Thus, the out-of-plane orientation is ZnO [0001] || sapphire [0001]. No impurity phases were observed from the XRD results. This suggests that the solid solubility of phosphorus and magnesium has not been exceeded in the films under these growth conditions. Also note that there is no discernable change in the *c*-axis lattice parameter with increasing oxygen partial pressure. As discussed earlier in this chapter, the crystallinity of the P-doped (Zn_{0.9}Mg_{0.1})O films grown on LT-ZnO buffer layer was also characterized by four-circle XRD. The FWHM of the omega rocking curve for ZnO (0002) peak is 0.83°.

The ϕ scan of P-doped ZnMgO film grown on sapphire substrate was used to examine the epitaxy of the film and determine the in-plane orientation relationship between the film and substrate. Figure 5-8 shows the ϕ scans through ZnO (10 $\bar{1}$ 1) plane and sapphire (11 $\bar{2}$ 6) plane of the sample grown at 500°C, 20 mTorr oxygen pressure. A sixfold symmetry of the plane is shown indicating good epitaxy of the P-doped ZnMgO film. More interestingly, it is shown that P-doped ZnMgO film perfectly aligns with sapphire substrate. No 30° twisted orientation was observed in these films grown at 500°C. Therefore, the in-plane orientation relationship between the film and sapphire substrate is determined as ZnO [10 $\bar{1}$ 0] || sapphire [10 $\bar{1}$ 0].

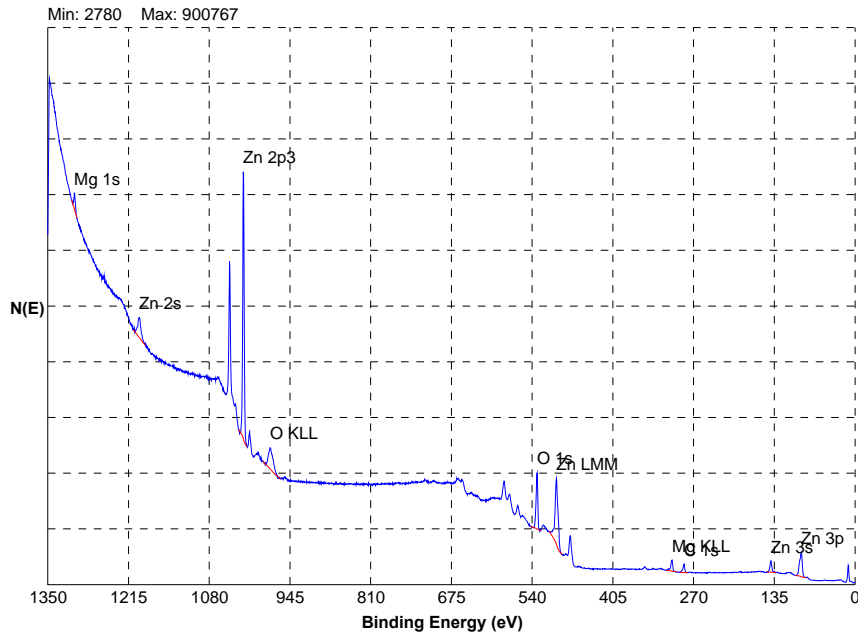


Figure 5-5 X-ray photoelectron spectroscopy survey of P-doped $(\text{Zn}_{0.9}\text{Mg}_{0.1})\text{O}$ films.

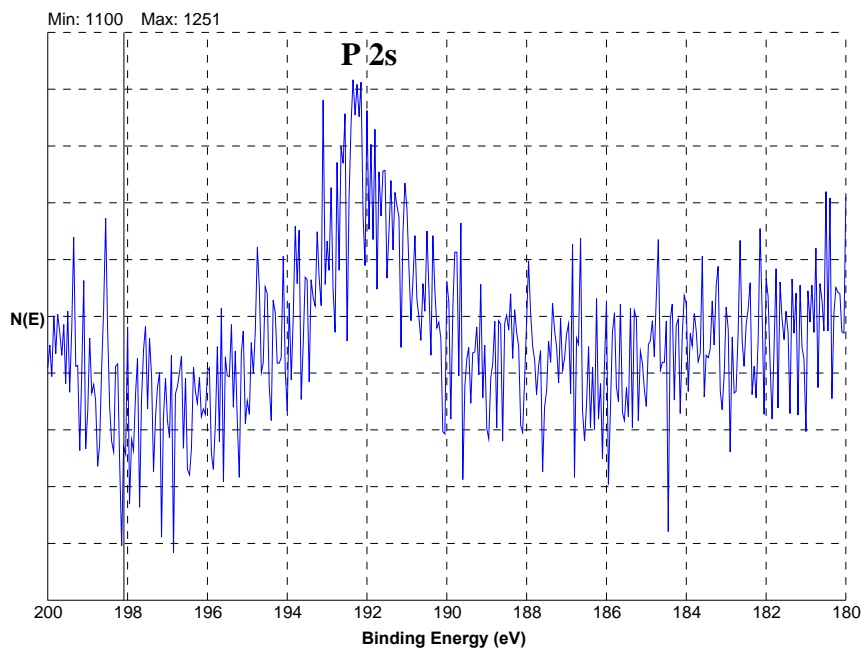


Figure 5-6 X-ray photoelectron spectroscopy multiplex of P 2s peak for P-doped $(\text{Zn}_{0.9}\text{Mg}_{0.1})\text{O}$ films grown at 500°C, 150 mTorr oxygen pressure.

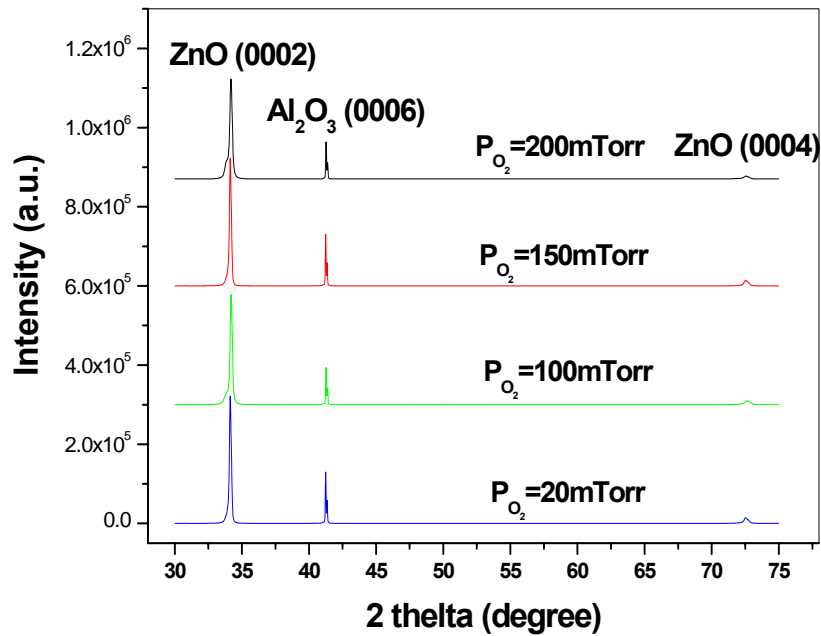


Figure 5-7. X-ray diffraction of P-doped $(\text{Zn}_{0.9}\text{Mg}_{0.1})\text{O}$ films grown under different oxygen partial pressures.

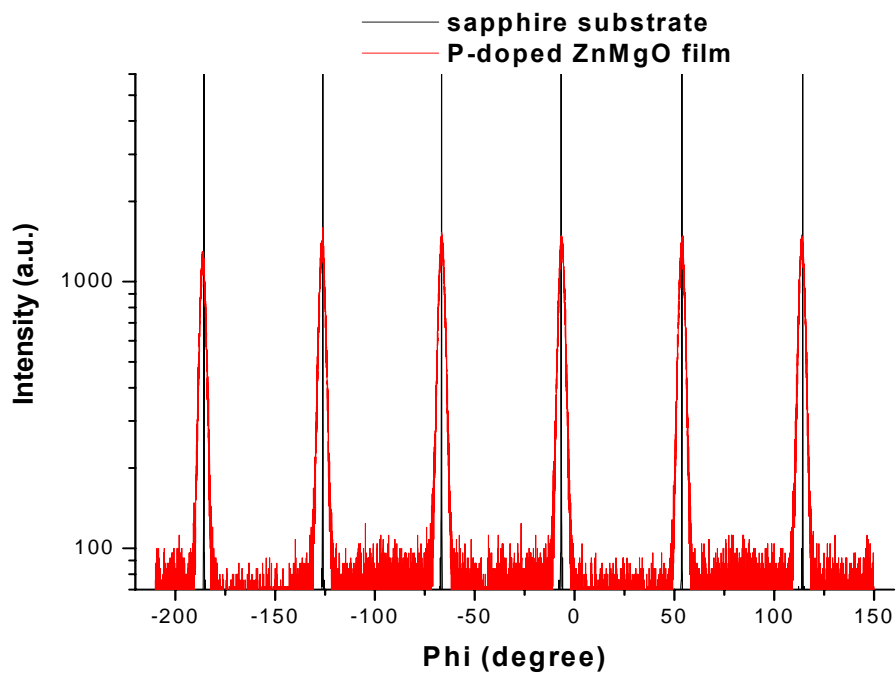


Figure 5-8. XRD ϕ scans of P-doped $(\text{Zn}_{0.9}\text{Mg}_{0.1})\text{O}$ film and sapphire substrate.

The surface morphology of the films grown at 500°C in various oxygen pressures is shown in Figure 5-8. The scan area is $2 \times 2 \mu\text{m}^2$ with a scan rate of 1 Hz. As the oxygen pressure increased, both grain size and surface roughness increased. Figure 5-9 shows the Root-Mean-Square (RMS) roughness of the P-doped ($\text{Zn}_{0.9}\text{Mg}_{0.1}\text{O}$) films as a function of oxygen partial pressure. The RMS roughness for the films increased from 2.60 nm to 12.8 nm as the oxygen growth pressure increased from 20 mTorr to 200 mTorr. For the p-type ($\text{Zn}_{0.9}\text{Mg}_{0.1}\text{O}$) films deposited at 150 mTorr oxygen pressure, the presence of grain boundaries can contribute to the low carrier mobility.

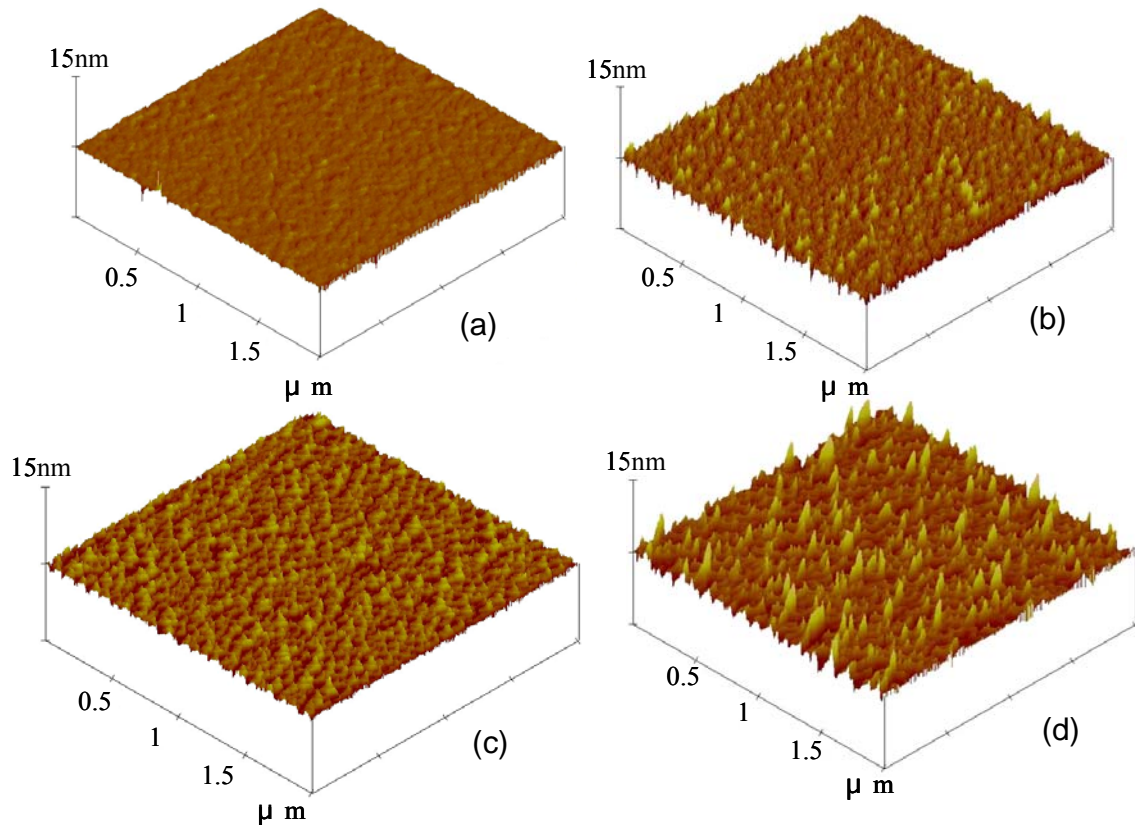


Figure 5-9. AFM images of the P-doped ($\text{Zn}_{0.9}\text{Mg}_{0.1}\text{O}$) films grown at different oxygen pressures: (a) 20; (b) 100; (c) 150; (d) 200mTorr.

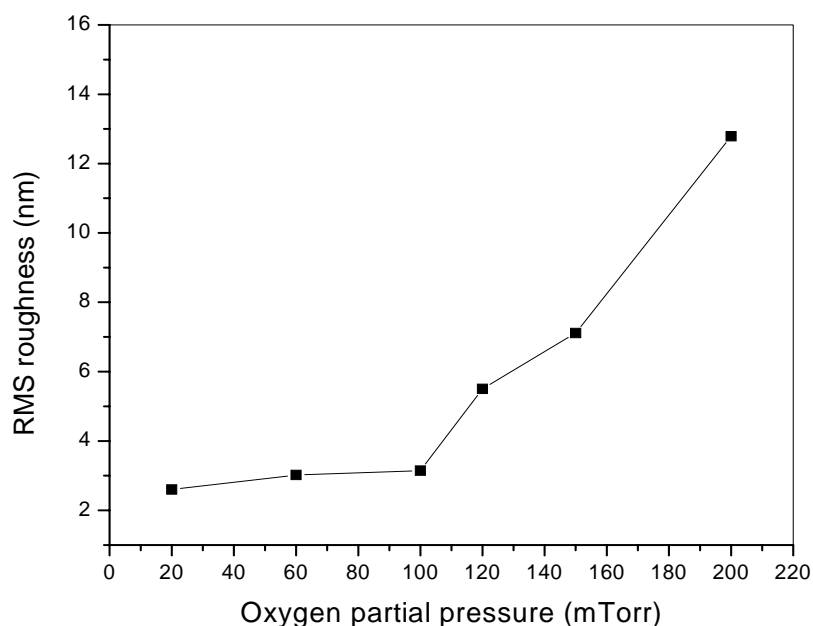


Figure 5-10. RMS roughness of the P-doped ($\text{Zn}_{0.9}\text{Mg}_{0.1}\text{O}$) films as a function of oxygen partial pressure.

In summary, p-type phosphorus-doped ($\text{Zn}_{0.9}\text{Mg}_{0.1}\text{O}$) films have been realized via pulsed laser deposition without post-annealing process. The conduction type of the films strongly depends on the oxygen partial pressure during the deposition process. The films grown at oxygen pressure lower than 100 mTorr are n-type. However, at oxygen pressure of 150 mTorr, the films showed p-type carrier type conduction with a hole concentration of $2.7 \times 10^{16} \text{ cm}^{-3}$, a mobility of $8.2 \text{ cm}^2/\text{Vs}$ and a resistivity of $35 \text{ } \Omega\text{-cm}$. XPS measurements confirmed the existence of P_2O_5 in the p-type P-doped ZnMgO film. XRD results showed good crystallinity of P-doped ZnMgO films grown under different oxygen pressures. The in-plane and out-of-plane orientation relationships are determined as $\text{ZnO} [10\bar{1}0] \parallel \text{sapphire} [10\bar{1}0]$ and $\text{ZnO} [0001] \parallel \text{sapphire} [0001]$. The RMS roughness for the films increased from 2.60 nm to 12.8 nm as the oxygen growth pressure increased

from 20 mTorr to 200 mTorr. The presence of grain boundaries can contribute to the low carrier mobility of p-type P-doped ZnMgO films.

CHAPTER 6
SYNTHESIS AND CHARACTERIZATION OF (Zn,Mg)O:P/ZnO
HETEROSTRUCTURES AND AL-DOPED ZnO

Introduction

Several studies have been reported regarding ZnO-based p-n junctions for LED applications. Alivov et al.[140,141] reported LEDs from n-ZnO/p-AlGa_{0.3}N and n-ZnO/p-GaN heterostructures grown epitaxially on SiC substrates using hybrid vapor-phase epitaxy combined with chemical vapor deposition. The UV LEDs emitted UV light at 389 nm and 430 nm at room temperature, respectively. Osinsky et al. [142] also have reported electroluminescence (EL) from p-(Al)Ga_{0.3}N/n-ZnO junctions. Tsukazaki et al. [143] obtained violet EL from ZnO homojunction grown on lattice matched ScAlMgO₄ substrates. Hwang et al. also reported on the diode and emission characteristics for a heterostructure of p-ZnO/n-GaN fabricated via RF magnetic sputtering [144]. We have previously reported ZnO-based p-n junctions deposited on undoped ZnO substrates using ZnMgO:P/ZnO heterostructure system [145]. The use of a ZnO buffer on the lightly n-type ZnO substrate was critical in achieving acceptable rectification in the junctions. Without this buffer, the junctions showed high leakage current. In this prior work, p-type conductivity was only obtained by post-growth annealing of the P-doped ZnMgO.

Studies in the previous chapters show that oxygen partial pressure plays a significant role in converting n-type to p-type conductivity for 2 at.% P-doped Zn_{0.9}Mg_{0.1}O films. The P-doped (Zn,Mg)O films grown at 150 mTorr oxygen partial pressure exhibited p-type conductance without post-growth annealing. In this chapter, the

development of ZnMgO:P/ZnO heterostructures on both sapphire and single crystal ZnO substrates is described. No post-growth annealing process was carried out for these structures. The characteristics of n- and p-side ohmic contact and the ZnMgO:P/ZnO heterojunction are presented. In addition, to reduce the presence of series resistance such as the current spread resistance in the n-type ZnO layer, 0.01 at. % Al-doped ZnO films were grown on sapphire substrates with MgO buffer layer. Three different growth conditions including growth temperature, oxygen partial pressure and laser energy were examined to provide a systematic study of growth condition effect on the properties of the Al-doped ZnO films. The dependence of crystallinity, electrical properties, photoluminescence and surface morphology on these growth conditions is discussed.

Experimental

Schematic diagrams of the p-ZnMgO/n-ZnO heterostructure on both (0001) c-sapphire and ZnO substrate are shown in Figure 6-1. The (0001) undoped grade I quality, single crystal ZnO substrate is obtained from Cermet. The room temperature electron concentration and mobility were 10^{17} cm^{-3} and $190 \text{ cm}^2/\text{Vs}$, respectively. Pulsed laser deposition was used for film growth. The 2 at.% phosphorus-doped $\text{Zn}_{0.9}\text{Mg}_{0.1}\text{O}$ target was fabricated using high-purity ZnO (99.995%) with or without MgO (99.998%), mixing with P_2O_5 (99.998%) as the doping agent. Sapphire and ZnO substrates were ultrasonically cleaned with trichloroethylene (TCE), acetone and methanol for 5 min and dried in N_2 prior to loading into the growth chamber. The growth chamber base pressure was $1-2 \times 10^{-7}$ Torr. A KrF excimer laser with a wavelength of 248nm was used as the ablation source. A laser repetition rate of 1Hz was used, with a target to substrate distance of 4cm and a laser pulse energy density of $1-3 \text{ J/cm}^2$. The n-ZnO layer $0.6 \mu\text{m}$ thick with an electron concentration of $2.53 \times 10^{18} \text{ cm}^{-3}$ and mobility $36.55 \text{ cm}^2/\text{Vs}$ was

grown first at 800 °C in an oxygen pressure of 100 mTorr, followed by a 0.4 μm thick p-ZnMgO:P layer grown at 500 °C, in 150 mTorr O₂.

Electron-beam evaporated Au (100nm) and Ti/Au (20nm/80nm) were deposited on the p-ZnMgO layer and n-ZnO patterned by lift-off process. In order to improve the ohmic characteristics, the post-growth annealing at 500 °C and 450 °C in N₂ for 2 min were performed, respectively. The I-V characteristics were measured using an Agilent 4145B parameter analyzer at room temperature.

A MgO buffer layer (~200nm) was initially deposited at 450 °C and 10⁻⁴ mTorr oxygen pressure before the growth of 0.01 at.% Al-doped ZnO films on sapphire substrates. The 0.01 at. % Al-doped ZnO target was fabricated using high-purity ZnO (99.995%) mixing with Al₂O₃ (99.998%) as the doping agent. The purpose of the MgO buffer layer is to reduce the micro-cracks resulting from the thermal expansion difference between ZnMgO and sapphire substrate. Table 6-1 shows the different growth conditions of the Al-doped ZnO via PLD. The film thickness of Al-doped ZnO is in the range of 0.75-1 μ m. The transport properties of the as-grown films were determined using four-point Van der Pauw Hall measurements at room temperature. The photoluminescence properties of the films were also measured at room temperature using a He-Cd laser (325nm). The film crystallinity and surface morphology were investigated via using four-circle X-ray Diffraction (XRD) and atomic force microscopy (AFM).

Results and Discussion

The current-voltage characteristics of the metal contacts to *n*-ZnO and *p*-ZnMgO were measured to examine the formation of the ohmic contacts. Previous results show that Au and Ti/Au can be used as ohmic contacts to *p*-ZnMgO and *n*-ZnO, respectively.

Low specific contact resistance was obtained for Au contact to *p*-ZnMgO after post-growth annealing process [146]. Figure 6-2 (a) and (b) show the I-V curves of the Au and Ti/Au metal contacts between two square pads (500 x 500 μm) at room temperature. The I-V characteristics indicate that ohmic contacts are formed on both electrodes. These results show that the rectifying behaviors shown in Figure 6-3 are due to the heterojunction of the ZnMgO/ZnO structure and not to the semiconductor/metal contacts.

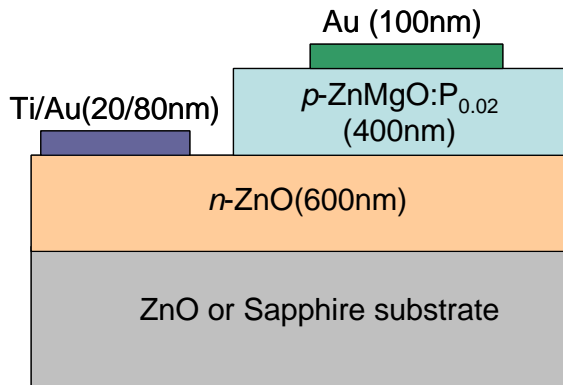


Figure 6-1. Schematic illustration of ZnMgO:P/ZnO heterostructure.

Table 6-1. Growth conditions of 0.01 at. % Al-doped ZnO films via PLD.

Sample	T _g (°C)	Oxygen pressure (mTorr)	Laser energy (mJ)	Buffer layer
A	700	20	350	
B	800	20	350	
C	700	20	300	MgO
D	800	20	300	
E	800	5	300	
F	800	50	300	

The I-V characteristics of the ZnMgO:P/ZnO heterostructure fabricated on sapphire and ZnO substrates are shown in Figure 6-3 (a) and (b), respectively. The devices exhibit clear rectifying electrical characteristics for both structures. Note that for the device grown on sapphire substrate, the drain current is higher than that of the device grown on ZnO substrate. This result might result from the difference in the resistivity of the

epitaxial layers grown on different substrates. The turn-on voltage V_T can be obtained from the intercept of the linear fitting in the forward bias range with the voltage-axis. For the structure grown on sapphire substrate V_T was determined to be about 1.36 V. For the ZnMgO:P/ZnO heterostructure grown on single crystal ZnO substrate, the turn-on voltages are 1.15 V and 2.26 V for the lateral and vertical device structure, respectively. Similar results on the I-V characteristics of oxide-based p-n junctions have been reported previously [147-149]. According to the current-voltage characteristics of the real diodes equations [150],

$$I = I_0 \left[\exp\left(\frac{V}{nV_i}\right) - 1 \right] \quad (6-1)$$

$$n = \frac{q}{kT} \frac{dV}{d \ln I} \quad (6-2)$$

where the pre-exponential factor I_0 is the reverse saturation current, V is the voltage at the junction, $V_i = kT/q$ is the thermal voltage, k is the Boltzmann constant, T is the absolute temperature, and n is the junction ideality factor. From equation (6-2), the ideality factors of the ZnMgO/ZnO heterostructures on sapphire and ZnO substrate can be extracted to be about 7.6 and 11.8, respectively. These large ideality factors possibly result from the defect-level assisted tunneling [151] and carrier recombination in the space-charge region via a deep level near midgap in the ZnMgO. Further work should focus on increasing the hole carrier concentration and mobility of *p*-ZnMgO and the optimization of structure synthesis in order to improve ZnMgO/ZnO *p-n* junction characteristics.

Four-circle X-ray diffraction was used to examine the crystallinity of the Al-doped ZnO samples (1cm x 1cm) grown on sapphire substrates. Figure 6-4 shows the XRD 2 theta scans of the as-grown 0.01at.%Al-doped ZnO films grown under different conditions, suggesting that the all the ZnO:Al films are oriented with the (0001) c-axis

uniformly parallel to the surface normal. Little change in diffraction intensity and lattice spacing was observed for the films grown under different conditions. To further delineate

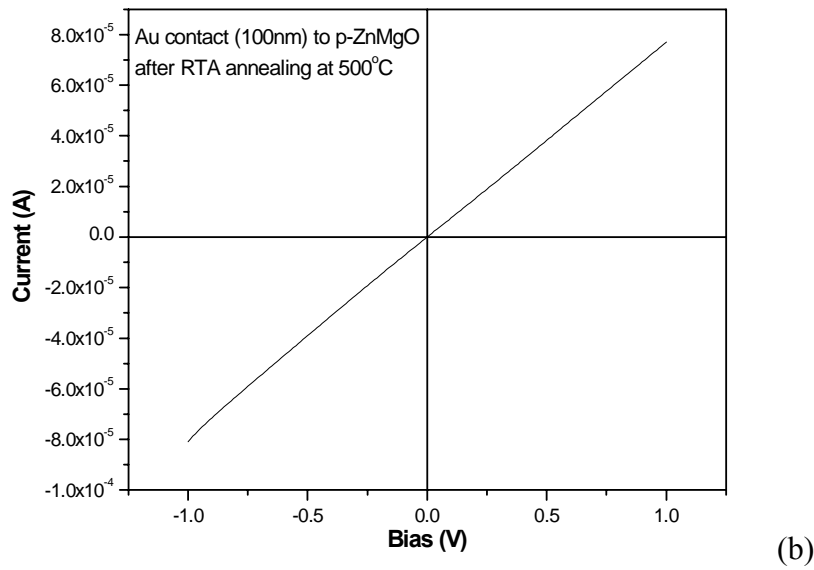
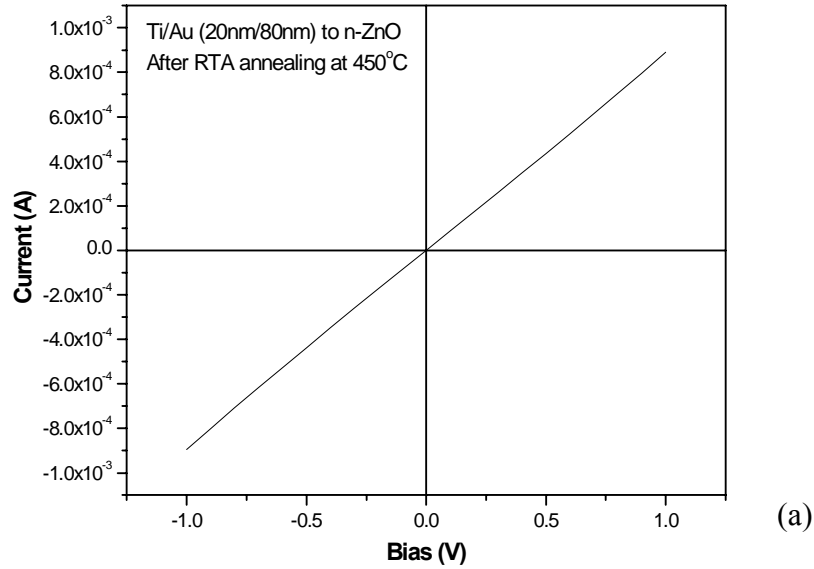
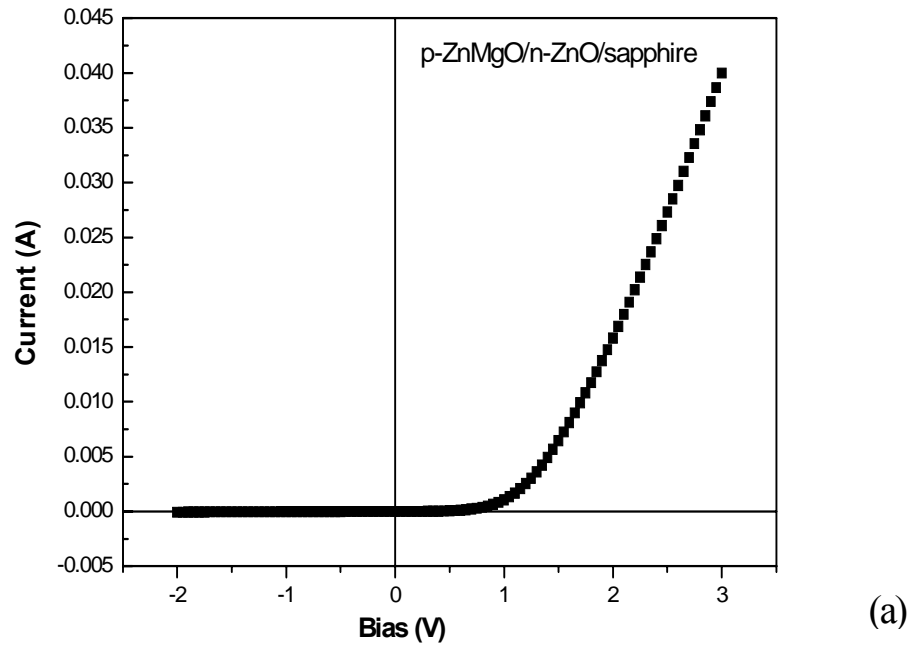
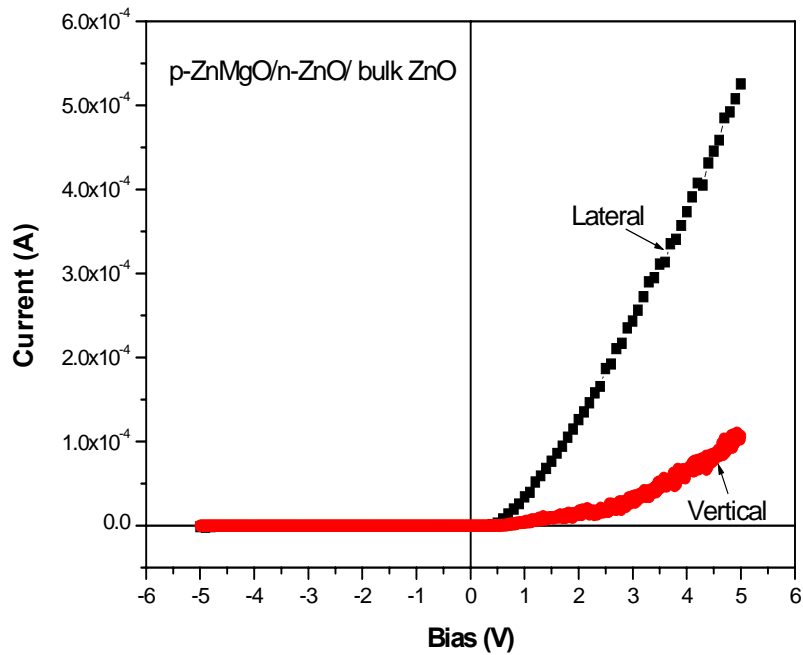


Figure 6-2. The I-V curve of Au and Ti/Au metal contacts on: (a) p-ZnMgO; (b) n-ZnO films, respectively.



(a)



(b)

Figure 6-3: Current-voltage characteristics of the ZnMgO/ZnO heterostructure on: (a) sapphire; (b) ZnO substrate.

the crystallinity of the films grown under different conditions, the omega rocking curve through the (0002) plane of ZnO was investigated. Figure 6-5 shows the omega rocking curve of ZnO:Al films grown under 300 mJ laser energy. The full-width-at-half-maximum (FWHM) values of the Al-doped ZnO films grown under different conditions are listed in Table 6-2. It is shown that for the films grown under 350 mJ laser energy, with increasing growth temperature the FWHM decreases from 0.37° to 0.33° indicating an improved crystallinity of the films. The film grown at 800°C, 50 mTorr oxygen pressure has the narrowest omega rocking curve with the FWHM of about 0.26°. The correlations of crystallinity to the electrical and optical properties of the films will be discussed later.

Table 6-2. FWHM values of ZnO (0002) omega rocking curve for 0.01 at. % Al-doped ZnO.

Sample	A	B	C	D	E	F
FWHM (degree)	0.3703	0.3308	0.2791	0.6366	0.3889	0.2636

Electrical properties of the ZnO:Al films was investigated via using four-point Van der Pauw Hall measurement at room temperature. Table 6-3 shows the Hall measurement results of the as-grown Al-doped ZnO films. The growth conditions of sample A-F are described in Table 6-1 previously. All the films show n-type conductivity with resistivity in the range of 10^{-3} - 10^{-1} ohm-cm. The electron concentration and mobility for these films are in the ranges of 10^{18} - 10^{19} cm⁻³ and 40-60 cm²/Vs, respectively. The effect of different growth conditions on the electrical properties of the films was delineated by analyzing these Hall data. As growth temperature increases, resistivity decreases for the samples grown under the same laser energy. The decrease of resistivity results from the increase in carrier concentration, mobility or both. In addition, the resistivity exhibits an increase

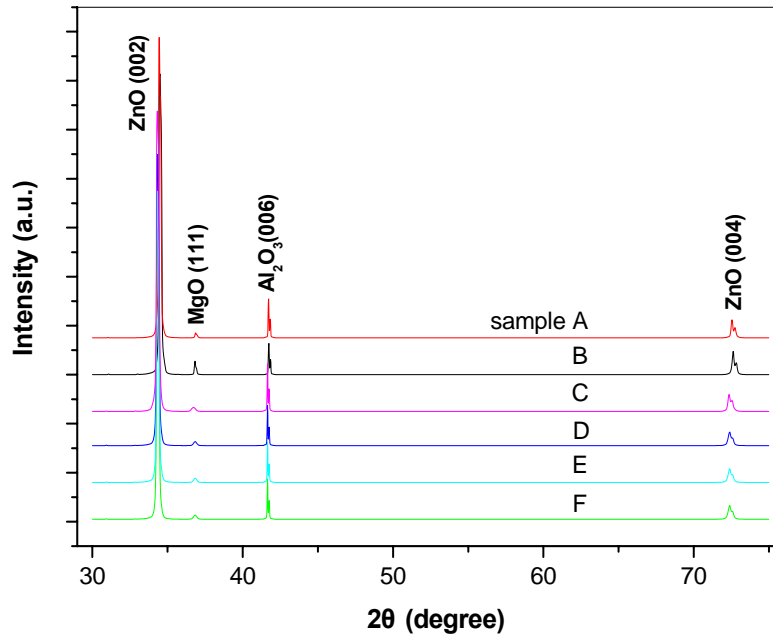


Figure 6-4. X-ray diffraction of 0.01 at.% Al-doped ZnO films grown under different conditions.

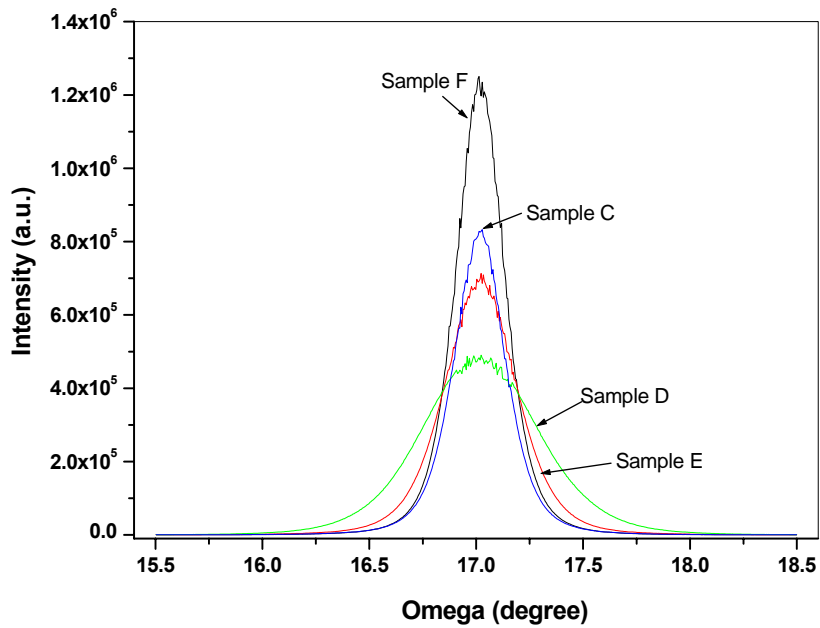


Figure 6-5. Omega rocking curve of ZnO (0002) peak for 0.01 at.% Al-doped ZnO films grown under 300 mJ laser energy.

with oxygen growth pressure for the Al-doped ZnO films grown under same laser energy and growth temperature. Several experimental studies reported similar dependence of resistivity on growth temperature and oxygen pressure for Al-doped ZnO films [152-154]. Kim *et al* [153] suggested that the resistivity of Al-doped ZnO films is related to the Al doping concentration, oxygen vacancies, Al and Zn concentrations at interstitial sites, grain boundaries and ionized impurity scattering. An increase in O/Zn ratio was observed with increasing growth temperature by using Rutherford Backscattering Spectrometry (RBS) [153]. Regarding to laser energy effect on the electrical properties of Al-doped ZnO films, it is shown that with increasing laser energy the resistivity of the films decreases for samples grown at 700°C (sample C vs. sample A). However, for the films grown at 800°C, resistivity does not show large increase with laser energy. Considering the donor contributions in Al-doped ZnO discussed above, the electron density is expected to increase with laser energy when the ZnO:Al target was bombarded by laser beam to create more interstitial atoms or vacancies. The number of scattering centers affecting the mobility of carriers was also increased with increasing laser energy and deposition rate [155].

Table 6-3. Room temperature Hall measurement of 0.01 at.% Al-doped ZnO films under different growth conditions.

Sample	Resistivity (ohm-cm)	Carrier density (cm ⁻³)	Carrier mobility(cm ² /Vs)	Carrier type
A	1.2376 x 10 ⁻²	7.82 x 10 ¹⁸	62.73	n
B	1.3656 x 10 ⁻²	1.158 x 10 ¹⁹	39.48	n
C	1.142 x 10 ⁻¹	1.399 x 10 ¹⁸	39.12	n
D	9.375 x 10 ⁻³	1.32 x 10 ¹⁹	50.45	n
E	8.336 x 10 ⁻³	1.329 x 10 ¹⁹	56.36	n
F	1.1285 x 10 ⁻²	9.094 x 10 ¹⁸	60.85	n

Room temperature PL (RT-PL) was performed to further investigate the effect of growth conditions on the optical properties of the Al-doped ZnO films. Figure 6-6 (a) and

(b) show the laser energy on RT-PL for the Al-doped ZnO films grown at 700°C and 800°C, respectively. The Al-doped ZnO films exhibit the band edge photoluminescence at ~377 nm with very low deep level emission. As laser energy increases from 300mJ to 350 mJ, the band edge emission increases for the films grown at both temperatures. Also note that with decreasing growth temperature from 800°C to 700°C the deposition laser energy shows more prominent effect on the band edge emission, which is consistent with the laser energy dependence of resistivity discussed in the previous section. In addition, as shown in Figure 6-6 (a) and (b) the band edge emission increases significantly with growth temperature. These results suggest that the photoluminescence of the Al-doped ZnO films has strong correlations to the electrical properties and crystallinity of the films. It is known that there are two recombination processes, i.e. radiative and nonradiative transition determining the light emission intensity. The photoluminescence efficiency can be enhanced by increasing the radiative transition and decreasing the nonradiative transition. For the Al-doped ZnO films, the intensity of band edge emission increases as the resistivity decreases due to the increased laser energy and growth temperature. With increasing electron density, the Fermi level will move up toward the conduction-band edge resulting in more mid-gap defect states being filled up. Thus, the possibility of the non-radiative trapping through those defect states will be decreased. For the films grown at a higher temperature, the nonradiative defects can also be reduced by improving the crystallinity of the films. Accordingly, the intensity of the band edge emission is significantly enhanced by increasing growth temperature for Al-doped ZnO films.

The oxygen partial pressure effect on the photoluminescence of the ZnO:Al films is shown in Figure 6-7. Note that the band edge emission intensity does not have linear

dependence on the oxygen partial pressure as resistivity does. As the oxygen pressure decreases from 5 mTorr to 20 mTorr, the band edge emission decreases. However, with further increasing oxygen pressure to 50 mTorr, the band edge emission markedly increases. The film grown at 800°C, 50 mTorr oxygen pressure shows the highest band edge emission of all the films. The above analysis is consistent with the XRD results discussed earlier. With increasing growth temperature, the FWHM value of the omega rocking curve of the films decreases. The film grown at 800°C, 50 mTorr oxygen pressure has the narrowest rocking curve suggesting that crystallinity plays an important role in the photoluminescence properties of the films.

The surface morphology of the films grown in different growth conditions were also examined by performing AFM measurement in air. Figure 6-8 shows the AFM images of the Al-doped ZnO films grown under different conditions. The growth conditions of sample A-F are described in Table 6-1 previously. The scan area is $5 \times 5 \mu\text{m}^2$ and the scan rate is 1 Hz. Interestingly note that growth temperature and oxygen pressure greatly affect the surface morphology of the films. The films grown at 700°C have the smoothest surface with the root-mean-square (RMS) roughness in the range of 8-9 nm. However, as growth temperature increases to 800°C, roughness rapidly increases. In addition, with increasing oxygen pressure the surface of the films also becomes rougher. The sample grown at 800°C, 50 mTorr and 300 mJ laser energy has the highest RMS roughness about 38nm. Similar growth temperature and oxygen pressure dependence of surface morphology was also observed for the P-doped ZnO and ZnMgO films.

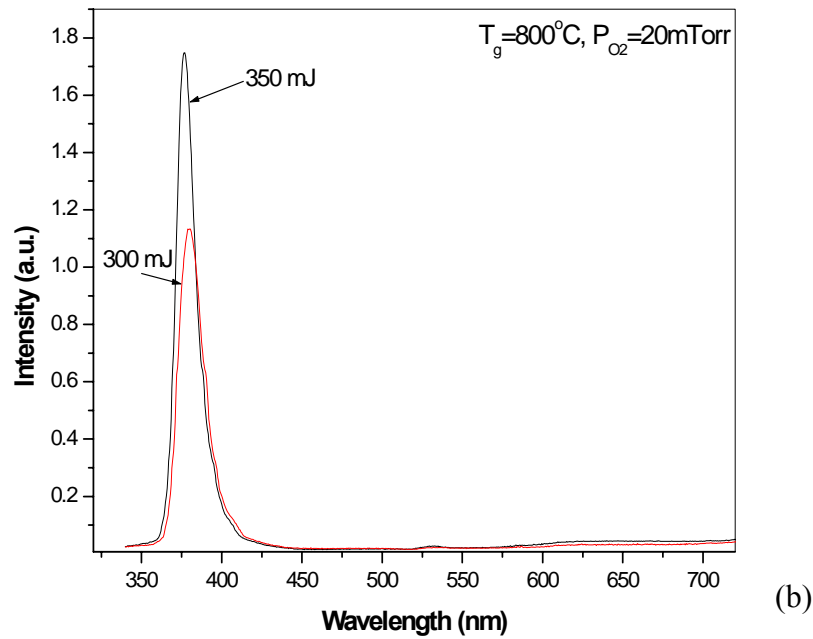
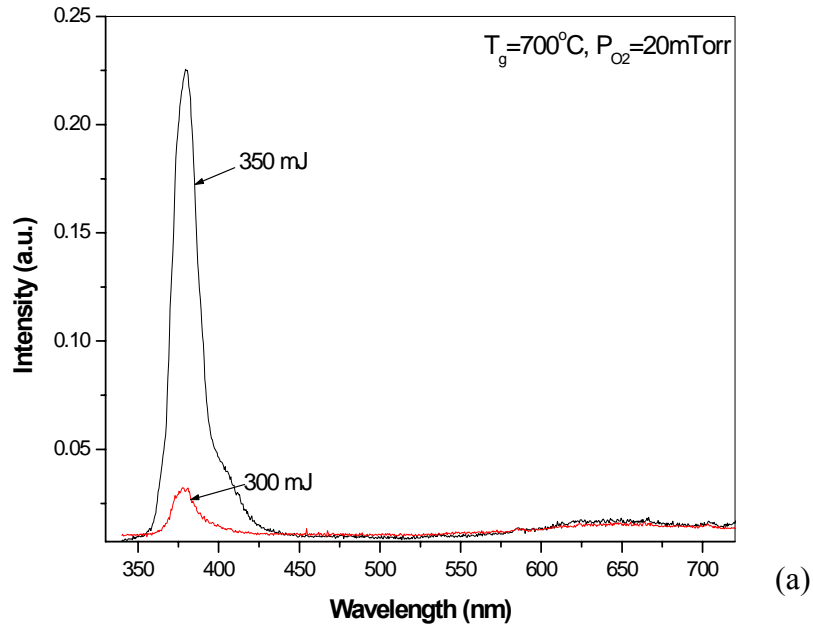


Figure 6-6. Laser energy effect on RT-PL for 0.01 at.% Al-doped ZnO films grown at (a) 700°C; (b) 800°C.

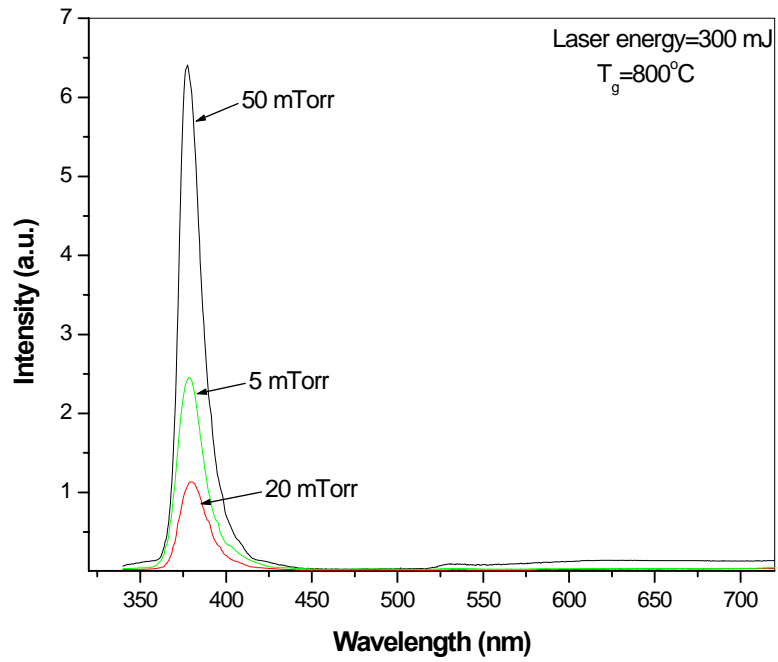


Figure 6-7. Oxygen partial pressure effect on room temperature PL of 0.01 at.% Al-doped ZnO films.

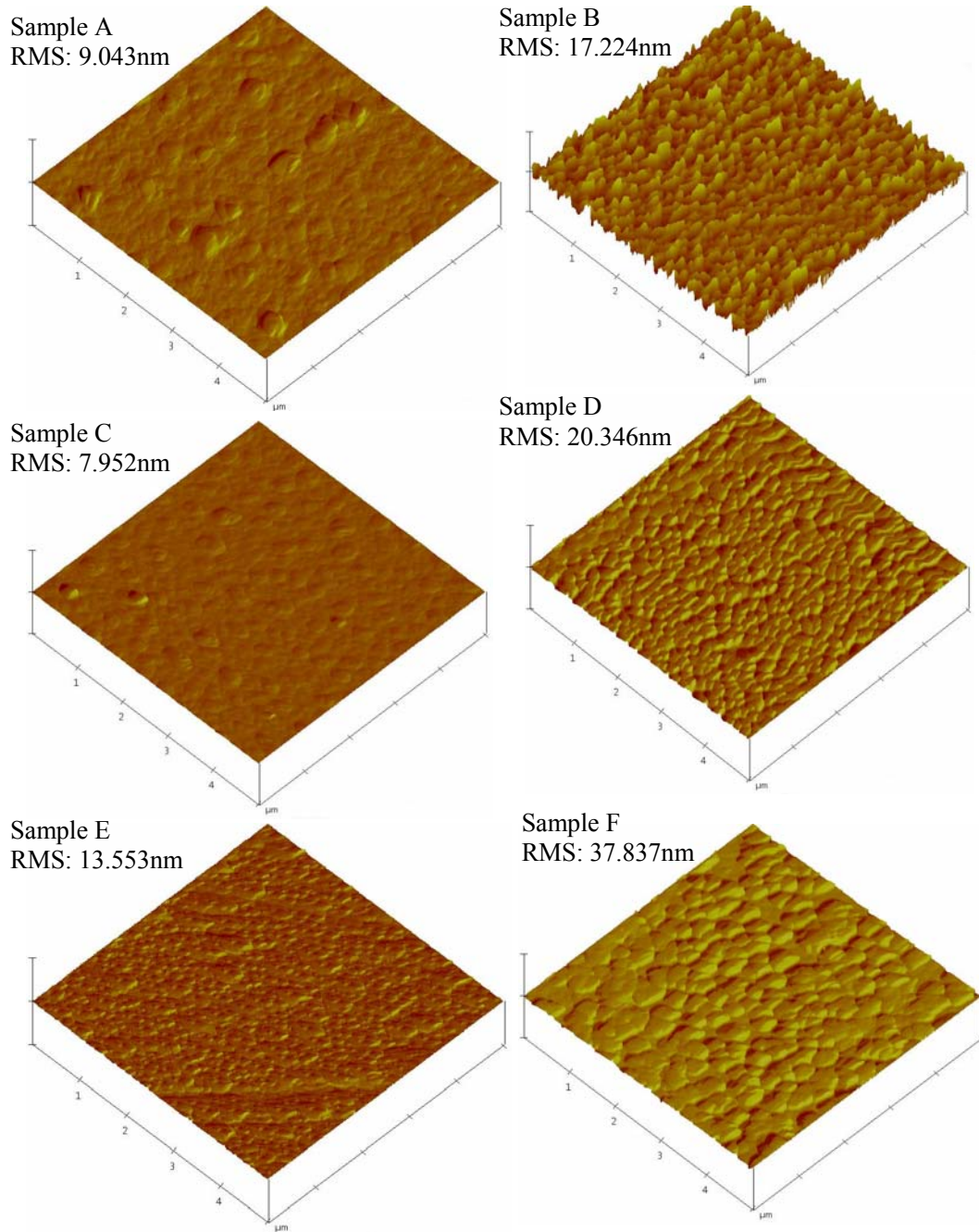


Figure 6-8. AFM image of 0.01 at.% Al-doped ZnO films grown under different conditions. The z-scale is 40 nm/div.

CHAPTER 7 GROWTH AMBIENT AND ANNEALING STUDY OF PHOSPHORUS-DOPED ZnO

Introduction

Systematic study of the effects of growth condition and post-annealing process is essential to control and optimize the properties of P-doped ZnO films. It has been suggested that Zn interstitials, O vacancies, and/or hydrogen complexes as compensation donors in p-type ZnO. Thus, studies need to include understanding the role of oxidizing species in yielding low native defect thin-film materials. The background impurity density of p-type ZnO during growth also needs to be minimized so as to observe the presence of acceptors in transport measurements. Previous studies [91] have focused on the effects of annealing on the transport properties of 1-5 at.% P-doped ZnO films grown by PLD. It showed that annealing significantly reduced the carrier density, yielding semi-insulating behavior which is consistent with activation of a deep acceptor level. However, no detailed studies have been carried out on the growth ambient effect on the properties of P-doped ZnO films as well as the annealing effect on these films.

In this chapter, the effects of different oxidation ambients, growth temperature and post-growth annealing on the properties of P-doped ZnO have been examined. The transport, photoluminescence as well as surface morphology properties of the films were discussed to elucidate these effects.

Experimental

Pulsed laser deposition was used to deposit phosphorus-doped ZnO epitaxial films on c-plane sapphire substrates. The targets were fabricated using high-purity ZnO

(99.995%) mixing with P_2O_5 (99.998%) as the doping agent. The targets were pressed and sintered at 1000°C for 12h in air. Considering the solubility limit of phosphorus in ZnO, the phosphorus doping level in ZnO:P target was chosen to be 0.2 at.%. A KrF excimer laser with a wavelength of 248nm was used as the ablation source. A laser repetition rate of 1Hz was used, with a target to substrate distance of 4cm and a laser pulse energy density of $1\text{-}3\text{ J/cm}^2$. Sapphire substrates were ultrasonically cleaned with trichloroethylene (TCE), acetone and methanol for 5 min and dried in N_2 prior to loading into the growth chamber. The growth chamber base pressure was 2×10^{-7} Torr. Film thickness was in the range of 400-500nm. P-doped ZnO films were deposited under different oxidizing conditions including oxygen and 4% H_2/Ar mixture, pure oxygen and ozone/oxygen mixture. The partial pressure ratio of oxygen and Ar/H_2 in the gas mixture was 1:1. The nitrogen-free plasma discharge ozone generator yielded an O_3/O_2 ratio on the order of 1–3%. The same total growth pressure was maintained at 60mTorr for the different ambients. The growth temperature ranged from 600°C to 800°C . Post-growth annealing was carried out at temperatures ranging from 800°C to 1100°C in a flowing O_2 ambient for 1hr. The transport properties of the as-grown and annealed films were determined using four-point Van der Pauw Hall measurements at room temperature. The photoluminescence properties of the films were also measured at room temperature using a He-Cd laser (325nm). The surface morphology of the films was investigated using atomic force microscopy (AFM).

Results and Discussion

Several studies discussed the passivation effect of hydrogen incorporation into ZnO [156-158]. Ogata *et al* [156] reported that high resistive N-doped ZnSe films were

converted to p-type by thermal annealing in nitrogen atmosphere. A hydrogen passivation model was proposed to explain the activation and passivation of N acceptors resulting from the dehydrogenation and hydrogenation. Accordingly, hydrogen passivation could be very helpful to enhance the p-type doping of ZnO since it would prevent self compensation during growth [158]. Thus, H₂/Ar gas mixture was introduced during the growth of P-doped ZnO to enhance the p-type doping of ZnO in this work.

Hall measurement was performed on these samples to examine the transport properties at room temperature. All of the films show n-type conductivity which is consistent with previous results on the as-grown P-doped ZnO films. Figure 7-1 shows the resistivity as a function of deposition temperature for films grown under different ambients. With increasing growth temperature, the difference in the resistivity of the films grown under different ambients increases. At growth temperature of 600°C the resistivity is within an order of magnitude for the films grown under different ambient. As growth temperature increases above 700°C, there is little change in resistivity for the films grown in pure oxygen and O₂/Ar/H₂ mixture. In contrast, resistivity increases from $2.2 \times 10^{-2} \Omega\text{-cm}$ to $3.5 \Omega\text{-cm}$ for the films grown in ozone/oxygen mixture.

Figure 7-2 shows the carrier density of ZnO: P_{0.002} films grown over a temperature range of 600°C to 800°C. The doping of phosphorus in ZnO films exhibits a significant increase in electron concentration which is in the range of 10^{19} to 10^{20} cm^{-3} . However, for the films grown in ozone/oxygen, the electron density rapidly decreases as increasing temperature. Compared with the O₂/Ar/H₂ mixture and pure O₂, the ozone/oxygen ambient presents a stronger oxidizing species because of the weaker O-O bonds in O₃. According to the theoretical calculations from chemical potentials [76], the anion-rich

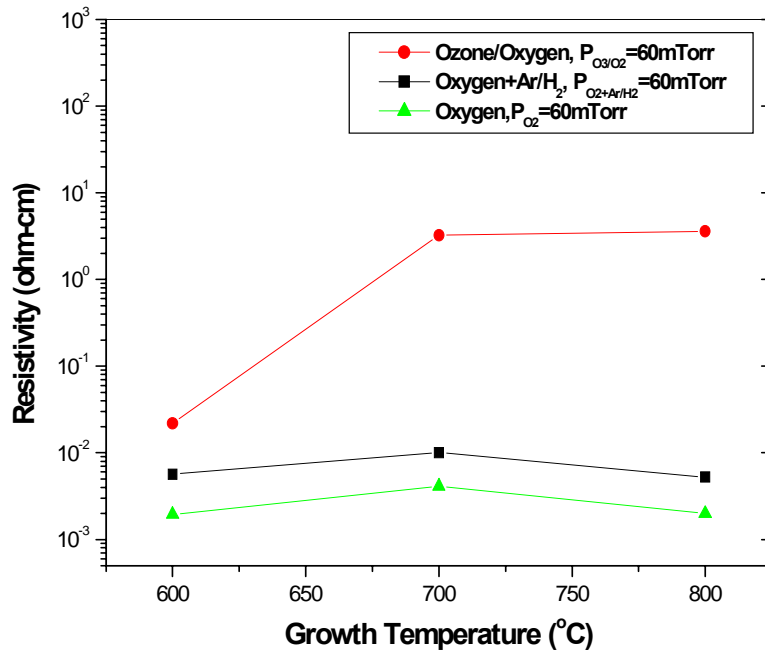


Figure 7-1. Room temperature resistivity as a function of growth temperature for ZnO: $P_{0.002}$ films grown in different gas ambient.

(oxygen-rich) growth conditions could inhibit the formation of compensating defects in p-type doping of ZnO. Therefore, the as-deposited ZnO:P films grown in ozone/oxygen condition shows significantly lower electron density with increasing growth temperature.

The Hall mobility of P-doped ZnO samples is shown in Figure 7-3. With increasing temperature, mobility continuously increases possibly due to the improved crystallinity of the films. For the films grown at 800°C, in pure oxygen and O₂/Ar/H₂ mixture, the mobility is about 35 cm²/Vs.

Consequently, the increase in resistivity for the films grown in ozone/oxygen is due to the rapid decrease in carrier density even though there is a slight increase in mobility. Note that the resistivity of the films grown in O₂/Ar/H₂ mixture is higher than those of the films grown in pure oxygen at different temperatures resulting from a lower value of

electron density. To further investigate and understand the effect of growth condition on the properties of P-doped ZnO films, photoluminescence needs to be measured. Figure 7-4 (a)-(c) show the RT-PL spectrums measured for the as-deposited ZnO:P_{0.002} films grown in O₂/Ar/H₂, pure oxygen and ozone/oxygen, respectively. A strong dependence on different growth ambient and temperatures has been demonstrated. The film grown in O₂/Ar/H₂ mixture shows a stronger band edge emission than those of the films grown in the other two ambients. With increasing growth temperature, this difference becomes more prominent. At growth temperature of 800°C, the films grown in O₂/Ar/H₂ mixture show a strong band edge emission at around 3.29 eV. The improvement in band edge emission intensity for the films grown in O₂/Ar/H₂ mixture may reflect the passivation effect of the deep acceptor-related levels by hydrogen, which also yields the passivation of the deep level emission. Thus, the radiative transition efficiency through band-band recombination is greatly enhanced.

Also note that for the films grown under O₂/Ar/H₂ mixture and pure oxygen, the peak in the band edge emission shifts to slightly longer wavelength, i.e. lower energy with increasing growth temperature. Regarding to the Hall results in Figure 7-2, the carrier density of the films grown in O₂/Ar/H₂ and pure oxygen decreases with the growth temperature. For both growth conditions, the carrier density is in the range of 10¹⁹ to 10²⁰ cm⁻³. Therefore, this shift in PL could be explained by using the Moss-Burstein effect which refers to an increase in the band gap due to the increase in Fermi level in highly degenerate conditions [159].

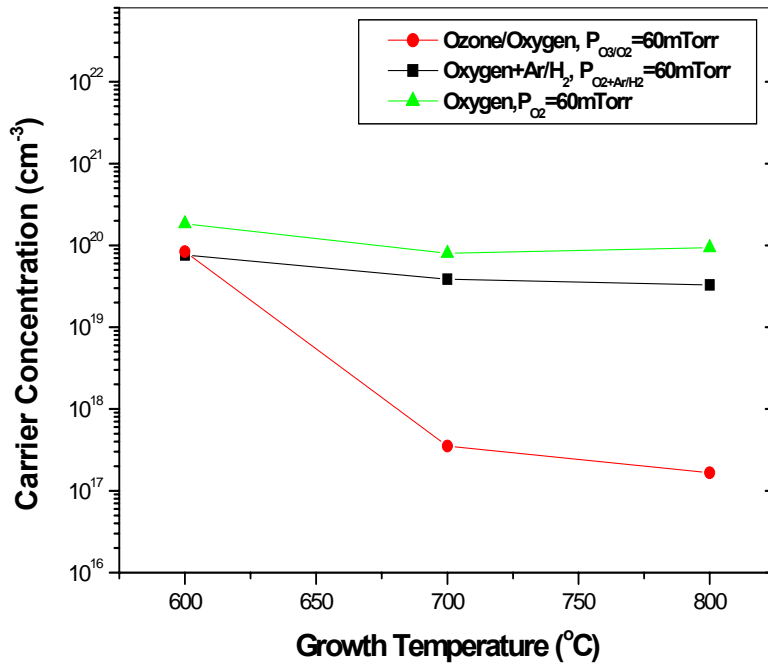


Figure 7-2. Carrier density of ZnO: P_{0.002} films as a function of growth temperature.

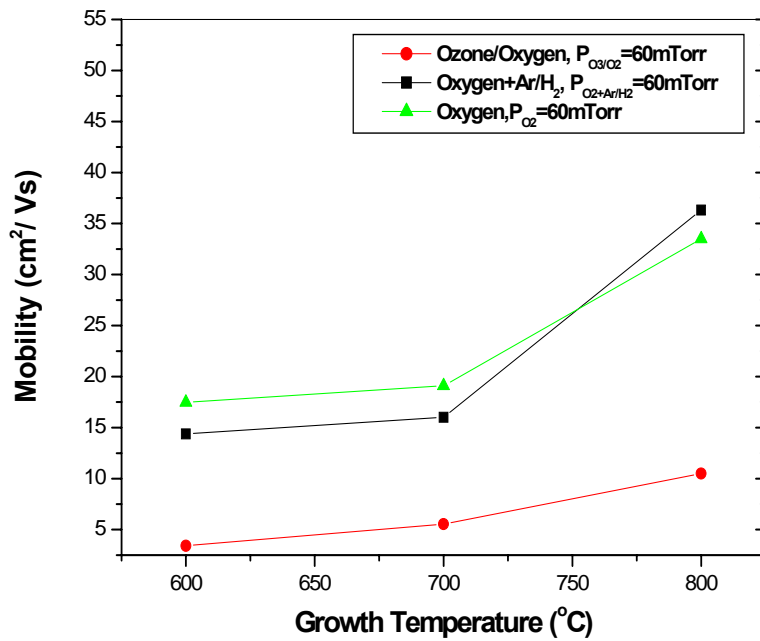


Figure 7-3. Carrier mobility of ZnO: P_{0.002} films as a function of growth temperature.

The RT-PL properties of the films grown in ozone/oxygen are shown in Figure 7-4 (c). The intensity of the band edge emission is very low for the films grown in O₃/O₂ mixture, almost quenched entirely with growth temperature as shown in the inset of Figure 7-4 (c). The deep level luminescence shows much stronger intensity, which increases greatly as growth temperature increases. Previous annealing studies of undoped ZnO [160] have shown a similar dependence of PL on the annealing ambient, with a decrease in band edge emission and an increase in visible defect-related luminescence as ZnO is annealed in an oxidizing environment. However, annealing in the reducing hydrogen ambient increases the band edge emission while subsequently decreasing the deep level emission.

In addition to the growth ambient effect, the growth temperature also plays an important role in the band edge emission. Increasing the deposition temperature improves the UV band edge emission due to a reduction in the structural defects, although the opposite effect is shown for the films grown in O₃/O₂ mixture which is might due to the more effective oxidization process as increasing temperature.

In an effort to reduce electron density and elucidate the phosphorus doping in ZnO, the effect of annealing process on the properties of the ZnO:P_{0.002} films grown under different ambients was examined. The as-grown films were annealed in flowing oxygen for 1hr at temperatures ranging from 800°C to 1100°C. Figure 7-5 (a)-(c) shows the resistivity of the samples annealed at different temperatures and ambients as a function of growth temperature. After the samples being annealed at 800°C in oxygen, the resistivity significantly increases from 10⁻³ to several Ω -cm regardless of growth ambient. However, with further increasing annealing temperature the resistivity starts to decrease. In the

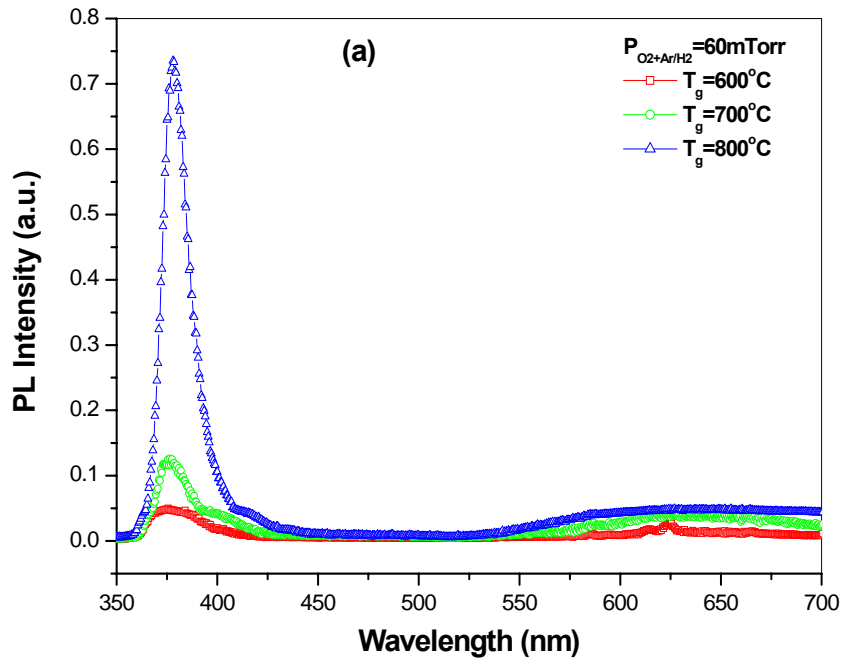


Figure 7-4. Photoluminescence spectra of P-doped ZnO grown in: (a) $O_2/Ar/H_2$; (b) pure oxygen; (c) ozone/oxygen.

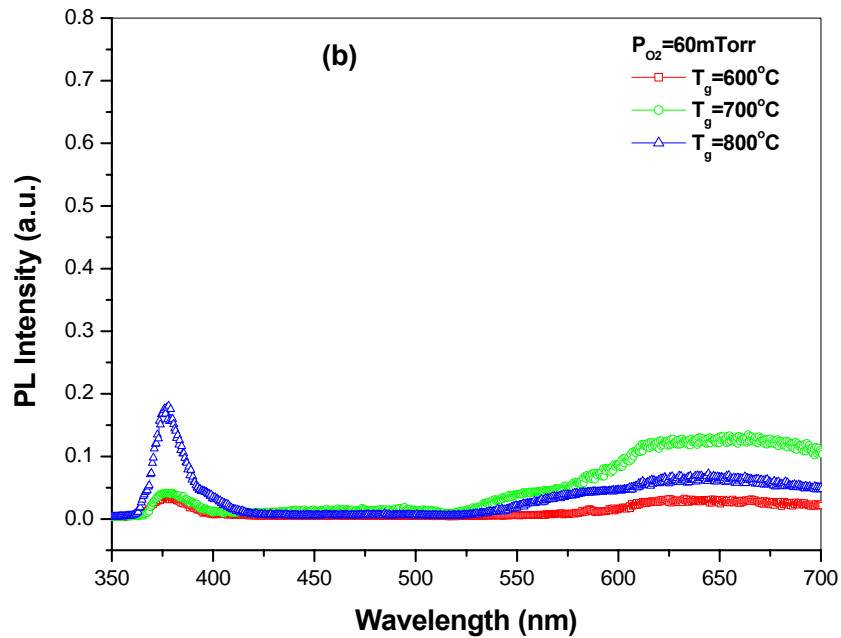


Figure 7-4. Continued.

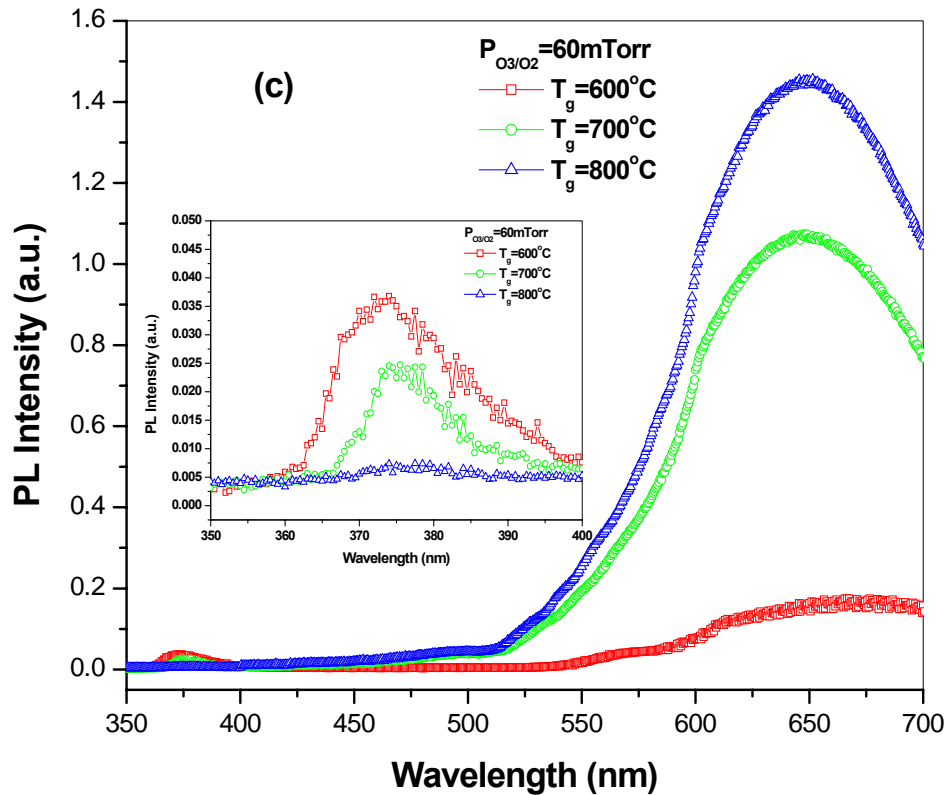


Figure 7-4. Continued.

previous studies on the annealing effect of P-doped ZnO, phosphorus was activated as an acceptor in P-doped ZnO at around 800°C [90]. It also showed that with increasing annealing temperature above 800°C, the hole concentration in the films starts decreasing. These results may suggest that around 800°C is the optimized annealing temperature to thermally activate phosphorus in P-doped ZnO.

The carrier density and Hall mobility for annealed ZnO:P_{0.002} films over a temperature range of 800°C to 1100°C are shown in Figure 7-6 and 7-7, respectively. The Hall measurements indicate that annealed ZnO:P_{0.002} films are also n-type. It indicates that carrier density shows a similar dependence on annealing temperature. However, the mobility of annealed films generally increases as annealing temperature increases.

Very strong deep level emission has been shown for the RT-PL results of annealed samples grown in different conditions. Figure 7-8 shows the RT-PL results for the films grown in $O_2/Ar/H_2$ gas mixture subjected to different annealing temperatures. With increasing annealing temperature, the intensity of the band edge emission decreases while the intensity of deep level emission tremendously increases. This yellow-orange emission has also been observed in ZnO elsewhere [161-163]. It has been suggested that the yellow emission which peaks at around 2.0 eV is due to the single negatively charged interstitial oxygen ions [164]. The intensity of the yellow emission increased with the temperature and oxidation time for the ZnO films under thermal oxidization [161]. In this work, the intensity of the yellow-orange deep level emission was observed to increase with annealing temperature, which could be explained by the increased oxygen interstitials in the P-doped ZnO films.

Surface morphology of annealed P-doped ZnO films was also examined by using AFM. RMS roughness of as-grown samples increases significantly with growth temperature. These results are consistent with the previous ones for the Al-doped ZnO films. Figure 7-9 shows the annealing temperature effect on the surface morphology of P-doped ZnO films grown at 700°C . Note that with increasing annealing temperature, root mean square roughness decreases from 14.5 nm to 3.5 nm. As annealing temperature increases, the mobility of the surface atoms increases resulting in the decreased surface roughness. Thus, after being annealed at 1100°C , the sample shows atomically flat surface.

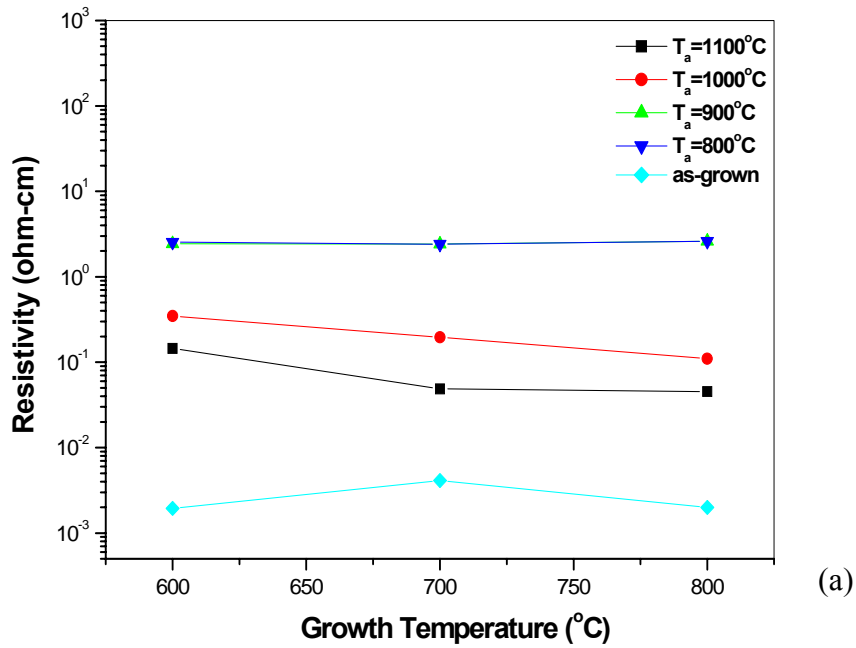


Figure 7-5. Resistivity of 0.2 at.% P-doped ZnO films annealed at different temperatures in O₂. The films were grown in: (a) O₂/Ar/H₂; (b) pure oxygen; (c) ozone/oxygen.

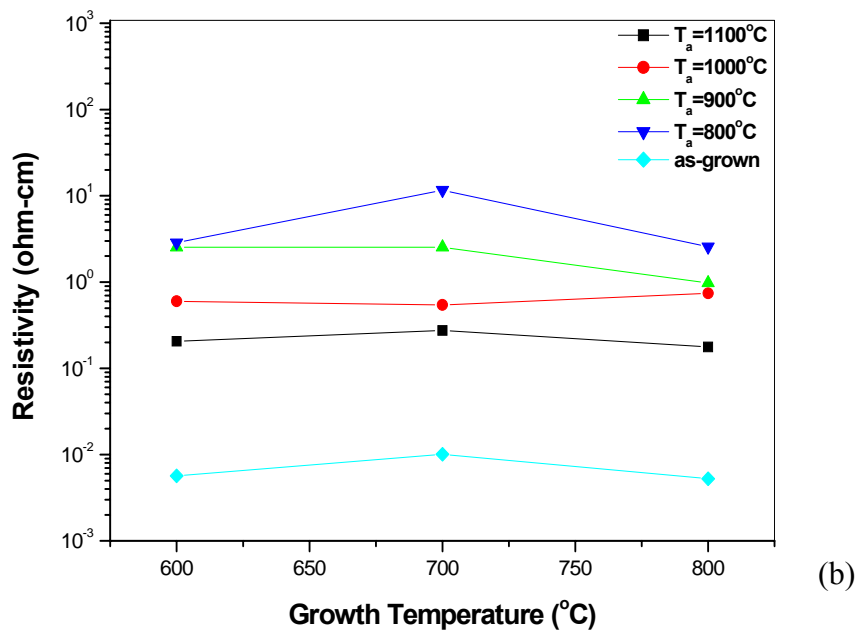


Figure 7-5. Continued.

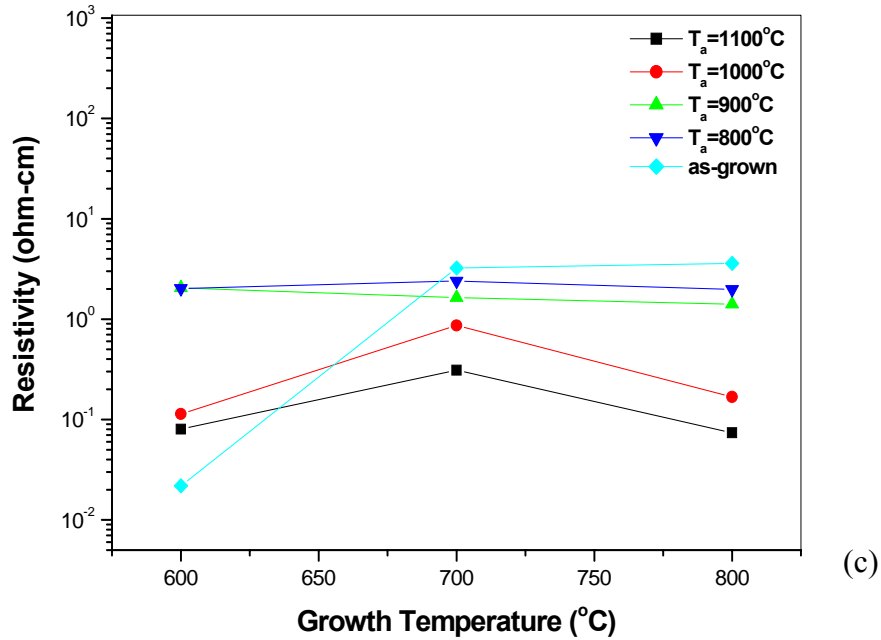
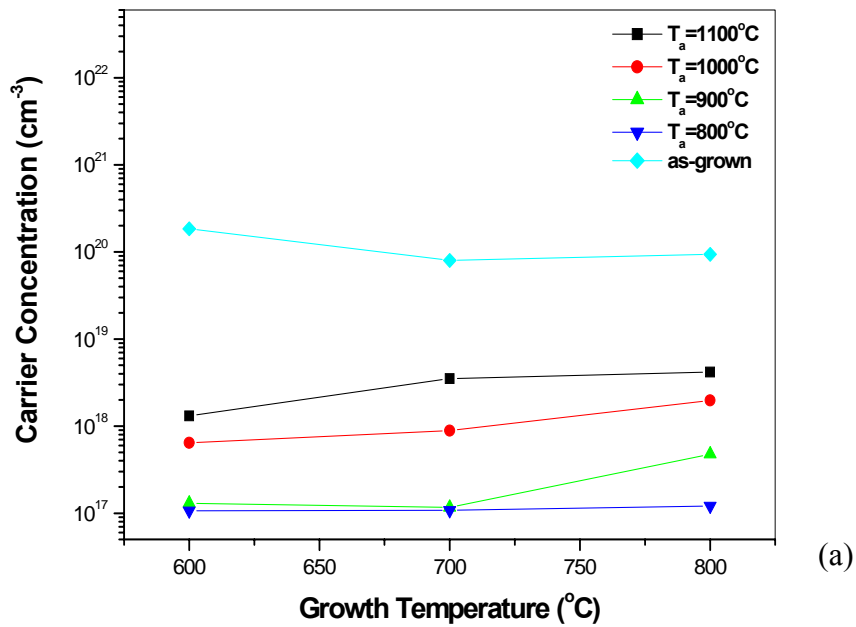


Figure 7-5. Continued.

Figure 7-6. Carrier concentration of 0.2 at.% P-doped ZnO films annealed at different temperatures in O₂. The films were grown in: (a) O₂/Ar/H₂; (b) pure oxygen; (c) ozone/oxygen.

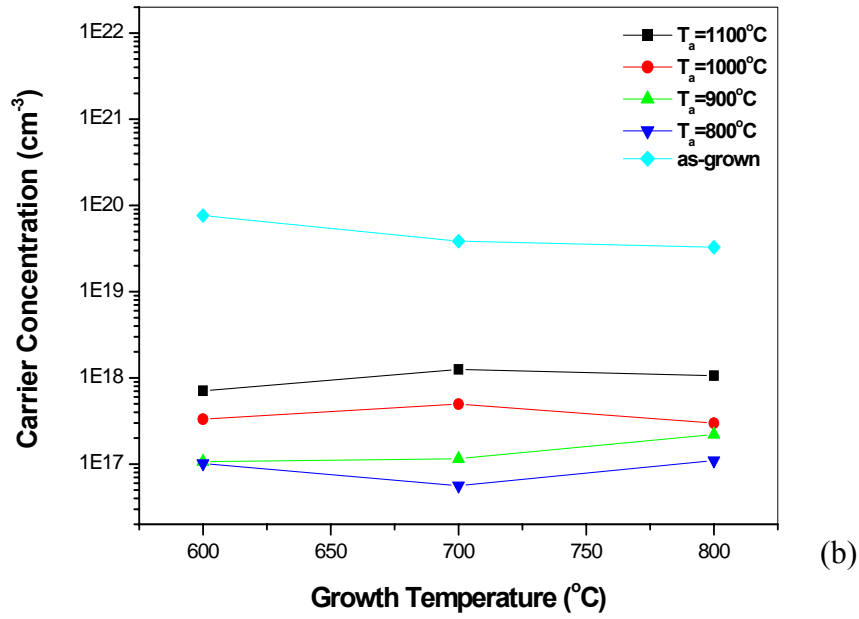


Figure 7-6. Continued.

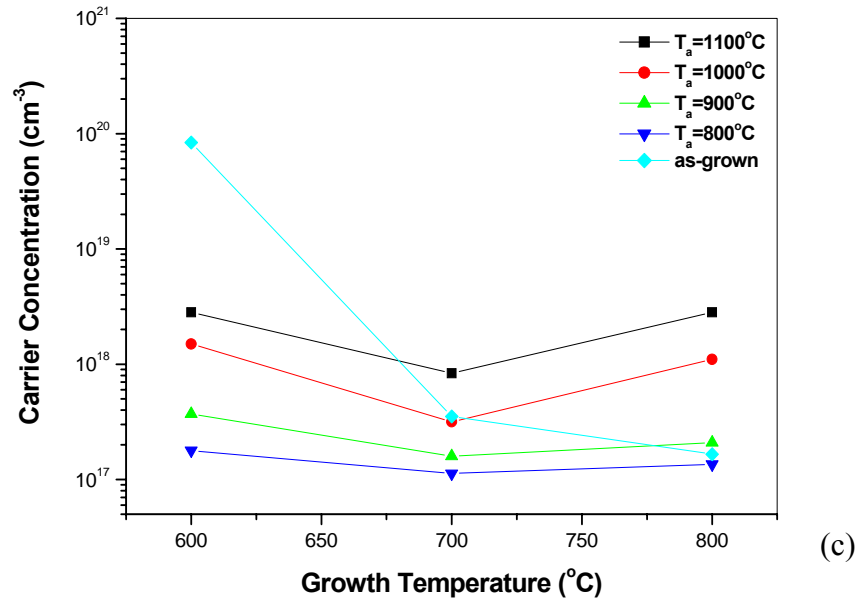


Figure 7-6. Continued.

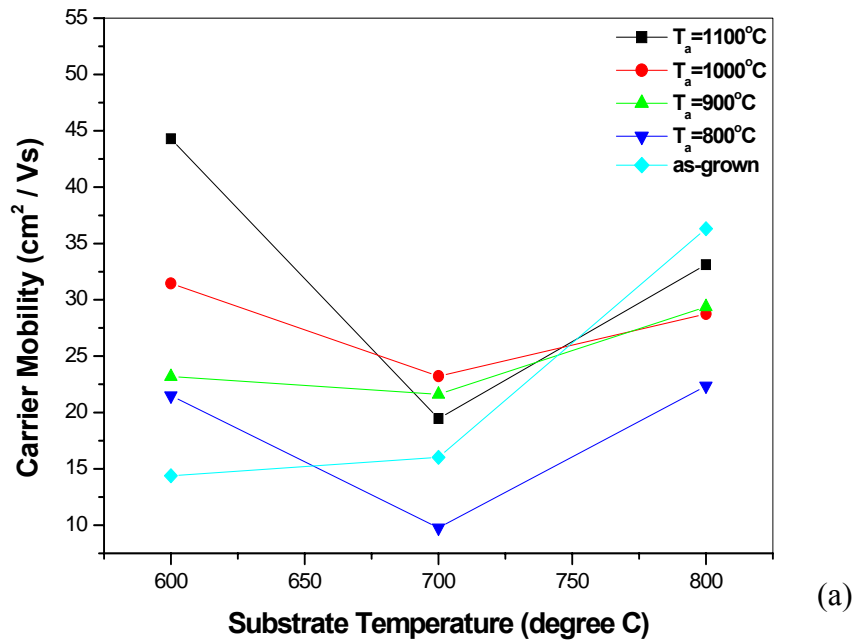


Figure 7-7. Mobility of 0.2 at.% P-doped ZnO films annealed at different temperatures in O_2 . The films were grown in: (a) $\text{O}_2/\text{Ar}/\text{H}_2$; (b) pure oxygen; (c) ozone/oxygen.

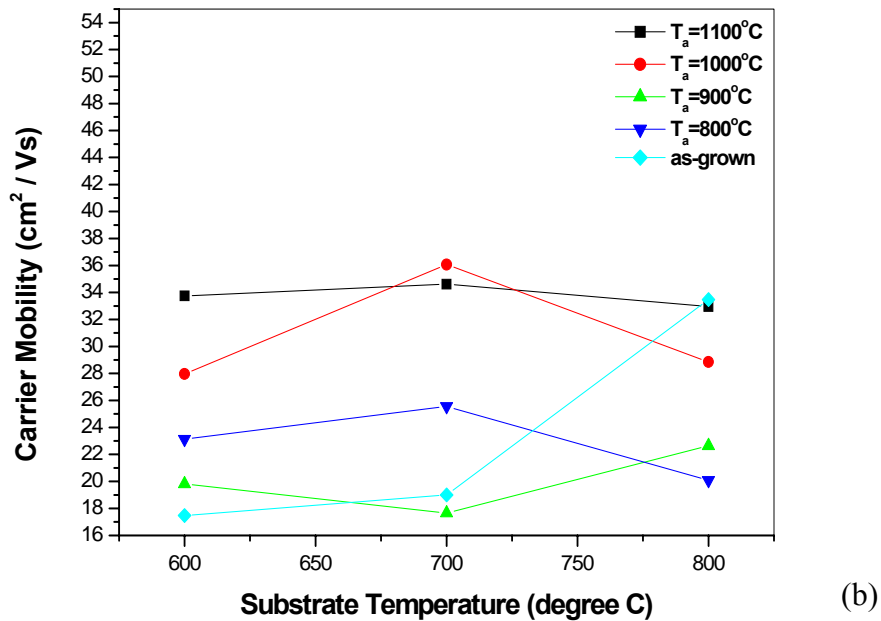


Figure 7-7. Continued.

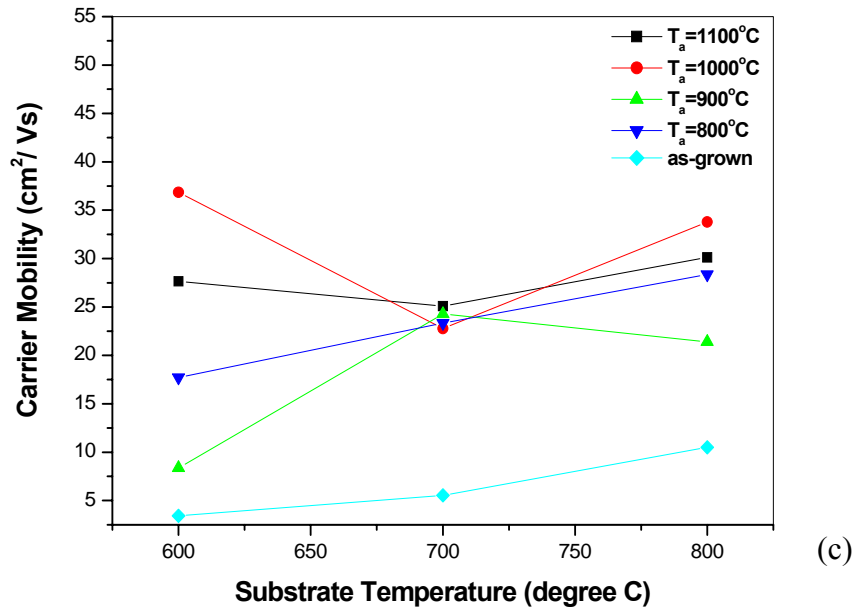
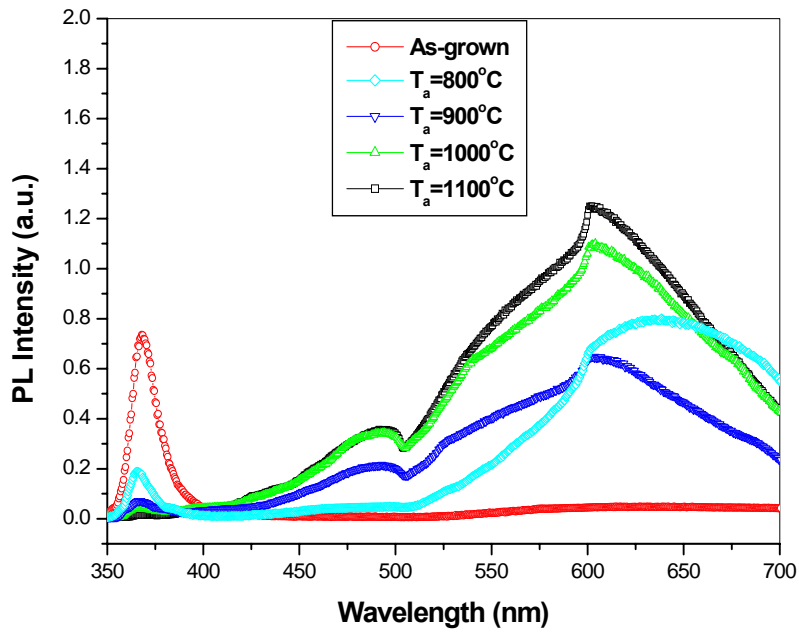


Figure 7-7. Continued.

Figure 7-8. RT-PL of 0.2 at.% P-doped ZnO films annealed at different temperatures in O₂. The films were grown at 800°C and in O₂/Ar/H₂ mixture.

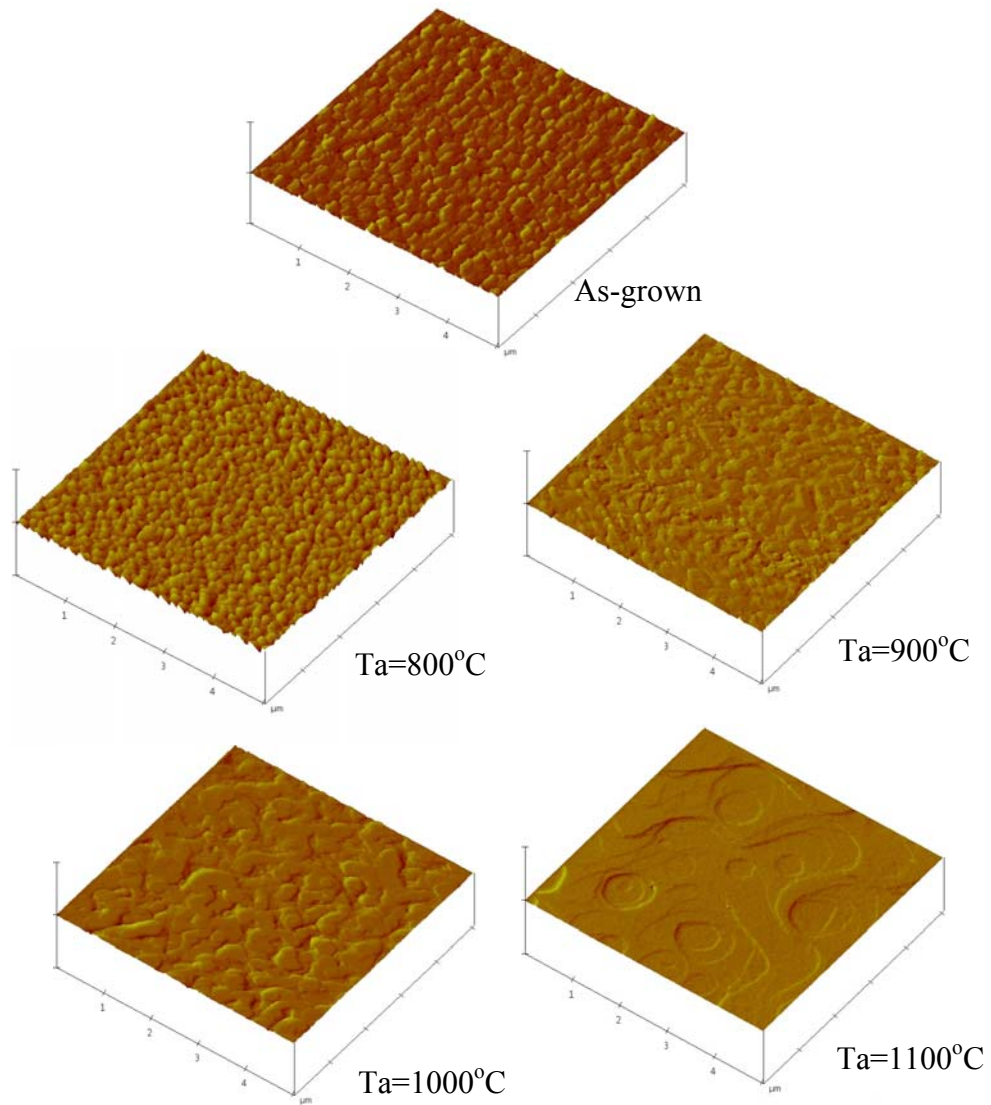


Figure 7-9. Surface morphology of 0.2 at.% P-doped ZnO films annealed at different temperatures in O_2 . The films were grown at 700°C and in 60 mTorr O_2 .

CHAPTER 8 CONCLUSIONS

This work has focused on the process development for ZnO-based thin film transistors on glass substrate and the growth and annealing condition effects on the properties of P-doped ZnO and (Zn,Mg)O films.

Top-gate type ZnO-based thin film transistors on glass substrates were fabricated via photolithography and wet chemical etching process. HCl acid solution was used to etch ITO source and drain pattern. It was found that H_3PO_4 has the best resolution for the gate metal and the highest selectivity of gate oxide and channel layers over underlying ITO. Three types of active channel materials including undoped ZnO, P-doped ZnO and (Zn,Mg)O were deposited at 400°C in 20 mTorr oxygen by PLD. Post-growth annealing treatments were carried out to decrease the electron density in the channel layer. The output characteristics of undoped and P-doped ZnO TFTs show the depletion-mode operation. A preferable enhancement-mode operation is shown for the device with P-doped (Zn, Mg)O as the channel layer. A saturation of I_{DS} is observed for small values of V_{DS} and the calculated FE mobility is about $5.32 \text{ cm}^2 \text{ V}^{-1} \text{ s}^{-1}$ at the drain voltage of 6V. The on/off current ratio is on the order of 10^3 at the gate voltage of 10V is obtained.

P-type phosphorus-doped ($\text{Zn}_{0.9}\text{Mg}_{0.1}$)O films have been realized via pulsed laser deposition without post-annealing process. The conduction type of the films strongly depends on the oxygen partial pressure during the deposition process. For films grown at 500°C , increasing the oxygen partial pressure from 20 to 200 mTorr yielded a carrier type conversion from n-type to p-type. At oxygen pressure of 150 mTorr, the films show p-

type carrier type conduction with a hole concentration of $2.7 \times 10^{16} \text{ cm}^{-3}$, a mobility of $8.2 \text{ cm}^2/\text{Vs}$ and a resistivity of $35 \text{ } \Omega\text{-cm}$. These results indicate the importance of oxidation conditions in realizing p-type (Zn,Mg)O films. XPS measurements confirmed the existence of P_2O_5 in the p-type P-doped ZnMgO film. XRD results showed good crystallinity of P-doped ZnMgO films grown under different oxygen pressures. The in-plane and out-of-plane orientation relationships are determined as ZnO $[10\bar{1}0] \parallel \text{sapphire } [10\bar{1}0]$ and ZnO $[0001] \parallel \text{sapphire } [0001]$, respectively. The RMS roughness of the films increased from 2.60 nm to 12.8 nm as oxygen partial pressure increased from 20 mTorr to 200 mTorr. The presence of grain boundaries can contribute to the low carrier mobility of p-type P-doped ZnMgO films.

$(\text{Zn}_{0.9}\text{Mg}_{0.1})\text{O}:\text{P}/\text{ZnO}$ heterostructures were fabricated on sapphire and ZnO substrates via pulsed laser deposition. Au and Ti/Au metal served as Ohmic contacts to p-ZnMgO:P and n-ZnO, respectively. The Ohmic characteristics of the contacts were improved after post-growth RTA process in N_2 . The heterojunction devices exhibit clear rectifying electrical characteristics for both structures. For the structure grown on sapphire substrate the turn-on voltage V_T is determined to be about 1.36 V. For the ZnMgO:P/ZnO heterostructure grown on single crystal ZnO substrate, the threshold voltages are 1.15 V and 2.26 V for the lateral and vertical device structure, respectively. The large ideality factors may result from several current transport processes being present in the non-ideal wide bandgap p-n junctions. Further work should be focused on increasing the hole carrier concentration and mobility of p-ZnMgO and the optimization of structure synthesis in order to improve ZnMgO/ZnO p-n junction characteristics.

Systematic studies of growth condition effect on the properties of 0.01 at.% Al-doped ZnO with MgO buffer layer have been focused. The dependence of resistivity on growth temperature, laser energy and oxygen growth pressure indicates that the resistivity of Al-doped ZnO is related to Al doping concentration, oxygen vacancies, Al and Zn concentrations at interstitial sites. The Al-doped ZnO films exhibit the band edge photoluminescence at ~377 nm with very low deep level emission. The intensity of the band edge emission of Al-doped ZnO films significantly increases with growth temperature and deposition laser energy. The photoluminescence properties of the Al-doped ZnO films have strong correlations to the electrical properties and crystallinity of the films. The possibility of the non-radiative trapping through deep level defect states decreases with increasing the electron density of Al-doped ZnO films. AFM results showed that the root-mean-square roughness increases with growth temperature and oxygen partial pressure.

The effect of growth ambient and post-growth annealing process on electrical and optical properties as well as the surface morphology of 0.2 at.% P-doped ZnO films was examined. The resistivity of the as-deposited samples grown in ozone/oxygen ambient rapidly increased with growth temperature. The oxidizing species play an important role in yielding low native donor defects in P-doped ZnO. A strong dependence of RT-PL on different growth ambients and temperatures has been demonstrated. The improvement in band edge emission intensity for the films grown in O₂/Ar/H₂ mixture may reflect the passivation effect of the deep acceptor-related levels by hydrogen, which also yields the passivation of the deep level emission. Annealing in oxygen at 800°C increased the resistivity of P-doped ZnO films by three magnitudes. Further increasing annealing

temperature decreased the resistivity of the samples. Both as-grown and annealed P-doped ZnO films show n-type conductivity. The intensity of the yellow-orange emission in RT-PL was enhanced by annealing the samples in oxygen. The increased oxygen interstitials resulted from annealing process may contribute to this deep level emission for the P-doped ZnO films.

LIST OF REFERENCES

1. D. C. Look, *Mater. Sci. Eng.* **B80**, 383 (2001).
2. R. L. Hoffman, B. J. Norris, *Appl. Phys. Lett.* **82**, 733 (2003).
3. R. L. Hoffman, *J. Appl. Phys.* **95**, 5813 (2004).
4. K. Nomura, *Nature*, **432**, 488 (2004).
5. Z. L. Wang, *J. P: Condens. Matt.* **16**, R829 (2004).
6. T. Dietl, H. Ohno, *Science*, **287**, 1019 (2000).
7. K. Ueda, H. Tabata, and T. Kawai, *Appl. Phys. Lett.* **79**, 988 (2001).
8. E. M. C. Fournato, P. M. C. Barquinha, A. C. M. B. G. Pimentel, A. M. F. Goncalves, A. J. S. Marques, R. F. P. Martins, and L. M. N. Pereira, *Appl. Phys. Lett.* **85**, 2541 (2004).
9. D. C. Look, D. C. Reynolds, C. W. Litton and R. L. Jones, D. B. Eason and G. Cantwell, *Appl. Phys. Lett.* **81**, 1830 (2002).
10. K. K. Kim, H. S. Kim, D. K. Hwang, J. H. Lim, and S. J. Park, *Appl. Phys. Lett.* **83**, 63 (2003).
11. Y. R. Ryu, T. S. Lee, and H. W. White, *Appl. Phys. Lett.* **83**, 87 (2003).
12. A. B. M. Almamun Ashrafi, A. Ueta, A. Avramescu, H. Kumano, I. Suemune, Y.W. Ok and T.Y. Seong, *Appl. Phys. Lett.* **76**, 550 (2000).
13. F. Decremps, J. Z. Jiang and R. C. Liebermann, *Europhys. Lett.* **51**, 268 (2000).
14. T. Matsuoka, N. Yoshimoto, T. Sasaki, and A. Katsui, *J. Electron. Mater.* **21**, 157 (1992).
15. F. Hamdani, A. Botchkarev, W. Kim, H. Morkoc, M. Yeadon, J. M. Gibson, D. C. Reynolds, D. C. Look, K. Evans, C. W. Litton, W. C. Mitchel, and P. Hemenger, *Appl. Phys. Lett.* **70**, 467 (1997).
16. F. Hamdani, M. Yeadon, D. J. Smith, H. Tang, W. Kim, A. Salvador, A. E. Botchkarev, J. M. Gibson, A. Y. Polyakov, M. Skowronski, and H. Morkoc, *J. Appl. Phys.* **83**, 983 (1998).

17. Y. Kayamura, Phys. Rev. B **38**, 9797 (1988).
18. W. Wegscheider, L. N. Pfeiffer, M. M. Dignam, A. pinczuk, K.W. West, S. L. McCall, R. Hull, Phys. Rev. Lett. **71**, 4071 (1993).
19. J. Ding, H. Jeon, T. Ishihara, M. Hagerott, and A. V. Nurmikko, Phys. Rev. Lett. **69**, 1707 (1992).
20. D. C. Reynolds, D. C. Look, and B. Jogai, Solid State Commun. **99**, 873 (1996).
21. D. M. Bagnall, Y. F. Chen, Z. Zhu, T. Yao, S. Koyama, M. Y. Shen, and T. Goto, Appl. Phys. Lett. **70**, 2230 (1997).
22. P. Yu, Z. K. Tang, G. K. L. Wong, M. Kawasaki, A. Ohtomo, H. Koinuma, Y. Segawa, J. Cryst. Growth **184/185**, 601 (1998).
23. D.W. Palmer, <http://www.semiconductors.co.uk/propiiivi5410.htm>, January, 2006.
24. National Compound Semiconductor Roadmap/compound semiconductor materials, http://www.onr.navy.mil/sci_tech/information/312_electronics/ncsr/properties.asp, January, 2006.
25. J. D. Albrecht, P. P. Ruden, S. Limpijumnong, W. R. L. Lambrecht, and K. F. Brennan, J. Appl. Phys. **86**, 6864 (1999).
26. T. Makino, Y. Sewaga, M. Kawasaki, A. Ohtomo, R. Shiraki, K. Tamura, T. Yasuda, and H. Koinuma, Appl. Phys. Lett. **78**, 1237 (2001).
27. L. M. Kukreja, S. Barik, and P. Misra, J. Cryst. Growth **268**, 531 (2004).
28. K. Sakurai, T. Takagi, T. Kubo, D. Kajita, T. Tanabe, H. Takasu, S. Fujita and S. Fujita J. Cryst. Growth **237-239**, 514 (2002).
29. A. Ohtomo, M. Kawasaki, T. Koida, K. Masubuchi, and H. Koinuma, Y. Sakurai, Y. Yoshida, T. Yasuda, and Y. Segawa, Appl. Phys. Lett. **72**, 2466 (1998).
30. S. Choopun, R. D. Vispute, W. Yang, R. P. Sharma, and T. Venkatesan, H. Shen, Appl. Phys. Lett. **80**, 1529 (2002).
31. A. K. Sharma, J. Narayan, J. F. Muth, C. W. Teng, C. Jin, A. Kvit, R. M. Kolbas, and O. W. Holland, Appl. Phys. Lett. **75**, 3327 (1999).
32. W. I. Park, G. C. Yi, and H. M. Jang, Appl. Phys. Lett. **79**, 2022 (2001).
33. R. D. Shannon, Acta Crystallogr. A **32**, 145 (1976).
34. J. F. Sarver, F. L. Katnack, and F. A. Hummel, J. Electrochem. Soc. **106**, 960 (1959).

35. A. Ohtomo, M. Kawasaki, I. Ohkubo, H. Koinuma, T. Yasuda, and Y. Segawa, *Appl. Phys. Lett.* **75**, 980 (1999).
36. J. Nause and B. Nemeth, *Semicond. Sci. and Technol.* **20**, S45 (2005).
37. D.C. Look, D.C. Reynolds, J.R. Sizelove, R.L. Jones, C.W. Litton, G. Cantwell and W.C. Harsch, *Solid-State Comm.* **105**, 399 (1998).
38. M. Suscavage, M. Harris, D. Bliss, P. Yip, S.-Q. Wang D. Schwall, L. Bouthillette, J. Bailey, M. Callahan, D.C. Look, D.C. Reynolds, R.L. Jones and C.W. Litton, *MRS Internet J. Nitride Semicond. Res* **4S1** G3.40 (1999).
39. E. Ohshima, H. Ogino, I. Niikura, K. Maeda, M. Sato, M. Ito, and T. Fukuda, *J. of Cryst. Growth* **260**, 166 (2004).
40. K. Maeda, M. Sato, I. Niikura, and T. Fukuda, *Semicond. Sci. Technol.* **20**, S49 (2005).
41. Cermet, Inc. company website: <http://www.cermetinc.com/>, January, 2006.
42. V. Srikant and D. R. Clarke, *J. Appl. Phys.* **81**, 6357 (1997).
43. Y. R. Ryu, S. Zhu, J. M. Wrobel, H. M. Jeong, P. F. Miceli and H. W. White, *J. Cryst. Growth* **216**, 326 (2000).
44. Y. Segawa, A. Ohtomo, M. Kawasaki, H. Koinuma, Z. K. Tang, P. Yu, and G. K. L. Wong, *Phys. Status Solidi B* **202**, 669 (1997).
45. M. Kawasaki, A. Ohtomo, I. Ohkubo, H. Koinuma, Z. K. Tang, P. Yu, G. K. L. Wong, B. P. Zhang, Y. Segawa, *Mater. Sci. Eng.* **B 56**, 239 (1998).
46. M. H. Huang, S. Mao, H. Feick, H. Yan, Y. Wu, H. Kind, E. Weber, R. Russo, P. Yang, *Science* **292**, 1897 (2001).
47. Young Jin Kim and Yoo Taek Kim, Hyung Kook Yang, Jong Chul Park, Yong Eui Lee and Hyeong Joon Kim, *J Vac. Sci. Technol. A* **15(3)**, 1103 (1997).
48. A. Ohtomo, K. Tamura, K. Saikusa, K. Takahashi, T. Makino, Y. Segawa, H. Koinuma, M. Kawasaki, *Appl. Phys. Lett.* **75**, 2635 (1999).
49. K. Tamura, A. Ohtomo, K. Saikusa, Y. Osaka, T. Makino, M. Sumiya, S. Fuke, Y. Segawa, H. Koinuma, M. Kawasaki, *J. Cryst. Growth* **214/215**, 59 (2000).
50. A. Tsukazaki, M. Kubota, A. Ohtomo, T. Onuma, K. Ohtani, H. Ohno, S. F. Chichibu and M. Kawasaki, *Jpn. J. Appl. Phys.* **44**, L643 (2005).
51. T. P. Smith, H. A. Mclean, D. J. Smith, P. Q. Miraglia, A. M. Roskowski, and R. F. Davis, *J. Electron. Mater.* **33**, 826 (2004).

52. A. B. M. A. Ashrafi, B. P. Zhang, N. T. Binh, K. Wakatsuki, and Y. Segawa, *Jpn. J. Appl. Phys. Part I* **43**, 1114 (2004).
53. V. Craciun, J. Elders, J. G. E. Gardeniers, and I. W. Boyd, *Appl. Phys. Lett.* **65**, 2963 (1994).
54. J. H. Choi, H. Tabata and H. Kawai, *J. Cryst. Growth* **226**, 493 (2001).
55. T. Yamamoto, T. Shiosaki, and A. Kawabata, *J. Appl. Phys.* **51**, 3113 (1980).
56. S. Hayamizu, H. Tabata, H. Tanaka, and T. Kawai, *J. Appl. Phys.* **80**, 787 (1996).
57. D. B. Laks, C. G. Van der Walle, G. F. Neumark, and S. T. Pantilides, *Phys. Rev. Lett.* **66**, 648 (1991).
58. T. Yamamoto and H. Katayama-Yoshida, *Jpn. J. Appl. Phys., Part 2* **38**, L166 (1999).
59. Y. Li, G. S. Tompa, S. Liang, C. Gorla, Y. Lu, and J. Doyle, *J. Vac. Sci. Technol. A* **15(3)**, 1063 (1997).
60. D. C. Look and B. Clafin, *Phys. Stat. Sol. (b)* **241**, 624 (2004).
61. A. F. Kohan, G. Ceder, D. Morgan, and C. G. Van de Walle, *Phys. Rev. B* **61**, 15 019 (2000).
62. S. B. Zhang, S. H. Wei, and Alex Zunger, *Phys. Rev. B* **63**, 075205 (2001).
63. D. C. Look, J. W. Hemsley, and J. R. Sizelove, *Phys. Rev. Lett.* **82**, 2552 (1999).
64. A. Janotti and C. G. Van de Walle, *Appl. Phys. Lett.* **87**, 122102 (2005).
65. C. G. Van de Walle, *Phys. Rev. Lett.* **85**, 1012 (2000).
66. D. M. Hofmann, A. Hofstaetter, F. Leiter, H. Zhou, F. Henecker, B. K. Meyer, S. B. Orlinskii, J. Schmidt, and P. G. Baranov, *Phys. Rev. Lett.* **88**, 045504 (2002).
67. C. H. Seager and S. M. Myers, *J. Appl. Phys.* **94**, 2888 (2003).
68. F. Tuomisto, K. Saarinen, and D. C. Look, *Phys. Rev. Lett.* **91**, 205502 (2003).
69. M. Miyazaki, M. Sato, K. Mitsui and H. Nishimura, *J. Un-Cryst Solids* **218**, 323 (1997).
70. S. Y. Myong, S. J. Baik, C. H. Lee, W. Y. Cho and K. S. Lim, *Jpn. J. Appl. Phys. Part II*, **36**, L1078 (1997).
71. H. J. Ko, Y. F. Chen, S. K. Hong, H. Wensch, T. Yao, and D. C. Look, *Appl. Phys. Lett.* **77**, 3761(2000).

72. J. F. Chang, H. L. Wang, and M. H. Hon, *J. Cryst. Growth*, **211**, 93 (2000).
73. C. H. Park, S. B. Zhang, and S. H. Wei, *Phys. Rev. B* **66**, 073202 (2002).
74. D. J. Chadi, *Phys. Rev. B*. **59**, 15181 (1999).
75. S. J. Pearton, D. P. Norton, K. Ip, Y. W. Heo, T. Steiner, *Pro. Mater. Sci.* **50**, 293 (2005).
76. A. Zunger, *Appl. Phys. Lett.* **83**, 57 (2003).
77. K. Minegishi, Y. Koiwai, Y. Kikuchi, K. Yano, M. Dasuga and A. Shimizu, *Jpn. J. Appl. Phys.* **36**, L1453 (1997).
78. D. C. Look, D. C. Reynolds, C. W. Litton and R. L. Jones, D. B. Eason and G. Cantwell, *Appl. Phys. Lett.* **81**, 1830 (2002).
79. M. Joseph, H. Tabata, and T. Kawai, *Jpn. J. Appl. Phys.* **38**, L1205 (1999).
80. X. L. Guo, H. Tabata, T. Kawai, *J. Cryst. Growth* **223**, 135 (2001).
81. K. Iwata, P. Fons, A. Yamada, K. Matsubara, and S. Niki, *J. Cryst. Growth* **209**, 526 (2000).
82. Yanfa Yan and S. B. Zhang, *Phys. Rev. Lett.* **86**, 5723 (2001).
83. X. Li, Y. Yan, T. A. Gessert, C. L. Perkins, D. Young, C. DeHart, M. Young, and T. J. Coutts, *J. Vac. Sci. Technol. A* **21**, 1342 (2003).
84. A. B. M. A. Ashrafi, I. Suemune, H. Kumano, and S. Tanaka, *Jpn. J. Appl. Phys.* **41**, L1281 (2002).
85. B. S. Li, Y. C. Liu, Z. Z. Zhi, D. Z. Shen, Y. M. Lu, J. Y. Zhang, X. W. Fan, R. X. Mu, and D. O. Henderson, *J. Mater. Res.* **18**, 8 (2003).
86. J. Huang, Z. Ye, H. Chen, B. Zhao, and L. Wang, *J. Mater. Sci. Lett.* **22**, 249 (2003).
87. J. Lu, Y. Zhang, Z. Ye, L. Wang, B. Zhao, and J. Huang, *Mater. Lett.* **57**, 3311 (2003).
88. J. Wang, G. Du, B. Zhao, X. Yang, Y. Zhang, Y. Ma, D. Liu, Y. Chang, H. Wang, H. Yang, and S. Yang, *J. Cryst. Growth* **255**, 293 (2003).
89. T. Aoki, D. C. Look, and Y. Hatanaka, *Appl. Phys. Lett.* **76**, 3257 (2000).
90. K. K. Kim, H. S. Kim, D. K. Hwang, J. H. Lim, and S. J. Park, *Appl. Phys. Lett.* **83**, 63 (2003).

91. Y. W. Heo, S. J. Park, K. Ip, S. J. Pearton, D. P. Norton, Appl. Phys. Lett. **83**, 1128 (2003).
92. Y. R. Ryu, T. S. Lee, and H. W. White, Appl. Phys. Lett. **83**, 87 (2003).
93. Y. R. Ryu, T. S. Lee, J. H. Leem, and H. W. White, Appl. Phys. Lett. **83**, 4032 (2003).
94. S. Limpijumnong, S. B. Zhang, S. H. Wei, and C. H. Park, Phys. Rev. Lett. **92**, 155504 (2004).
95. T. Yamamoto, and H. Katayama-Yoshida, Jpn. J. Appl. Phys. **38**, L166 (1999).
96. M. Joseph, H. Tabata, H. Saeki, K. Ueda, and T. Kawai, Physica B **302/303**, 140 (2001).
97. A. V. Singh, R. M. Mehra, A. Wakahara, and A. Yoshida, J. Appl. Phys. **93**, 396 (2003).
98. F. Zhu-Ge, Z.-Z. Ye, L. Zhu, J. Lu, B. Zhao, J. Huang, Z. Zhang, L. Wang, and Z. Ji, J. Cryst. Growth, **268**, 163 (2004).
99. J. G. Lu, Z. Z. Ye, F. Zhuge, Y. J. Zeng, B. H. Zhao, and L. P. Zhu, Appl. Phys. Lett. **85**, 3134 (2004).
100. D. B. Chrisey and G. K. Hubler, Pulsed Laser Deposition of Thin Films, John Wiley & Sons, Inc., New York, 1994.
101. X. D. Wu, R. E. Muenchausen, S. Foltyn, R. C. Estler, R. C. Dye, C. Flamme, N.S. Nogar, A. R. Garcia, J. Martin, and J. Tesmer, Appl. Phys. Lett. **56**, 1481 (1990).
102. G. Koren, A. Gupta, R. J. Baseman, M. I. Lutwyche, and R. B. Laibowitz, Appl. Phys. Lett. **55**, 2450 (1989).
103. R. K. Singh and J. Narayan, Phys. Rev. B, **41**, 8843 (1990).
104. C. R. Brundle, C. A. Evans, Jr., and S. Wilson, Encyclopedia of Materials Characterization, Butterworth-Heinemann, Stoneham, MA, 1992.
105. G. Binnig, C. F. Quate, and Ch. Gerber, Phys. Rev. Lett. **56**, 930 (1986).
106. The Electronics and Electrical Engineering Laboratory/The Semiconductor Electronics Division/Hall effect measurements, <http://www.eeel.nist.gov/812/effe.htm#lore>, January, 2006.
107. D. C. Look, Electrical Characterization of GaAs materials and Devices, John Wiley & Sons, Inc., New York, 1989.
108. D. J. Chadi and K. J. Chang, Phys. Rev. Lett. **61**, 873 (1988).

109. D. V. Lang and R. A. Logan, Phys. Rev. Lett. **39**, 635 (1977).
110. H. X. Jiang and J. Y. Lin, Phys. Rev. Lett. **64**, 2547 (1990).
111. C. C. Wu, S. Theiss, M. H. Lu, J. C. Sturm, and S. Wagner, Proc. IEDM'96, 957 (1996).
112. G. W. Jones, SID'01 DIGEST (2001).
113. M. Stewart, R. S. Howell, L. Pires, and M. K. Hatalis, IEEE Trans. Electron Devices, **48**, 845, (2001).
114. Y. He, R. Hattori, and J. Kanicki, IEEE Trans. Electron Devices, **48**, 1322 (2001).
115. W. E. Howard and O. F. Prache, IBM J. Res. & Dev., **45**, 1 (2001).
116. J.A. Nichols and T.N. Jackson, M. H. Lu and M. Hack. SID'02 DIGEST (2002).
117. Cambridge Display Technology, <http://www.cdtltd.co.uk/technology/39.asp>, January, 2006.
118. D. S. Ginley and C. Bright, Guest Editors, MRS Bulletin **25**, 15 (2000).
119. T. Minami, MRS Bulletin **25**, 38 (2000).
120. A.J. Freeman, K.R. Poeppelmeier, T. O. Mason, R.P.H.Chang and T.J.Marks, MRS Bulletin **25**, 45 (2000).
121. A. Suzuki, T. Matsushita, N. Wada, Y. Sakamoto, and M. Okuda, Japan. J. Appl. Phys. **35**, L56(1996).
122. H. Kawazoe, M. Yasukawa, H. Hyodo, M. Kurita, H. Yanagi and H. Hosono, Nature, **389**, 939 (1997).
123. T. Minami, Semicond. Sci. Technol. **20**, S35 (2005).
124. N. Duan, A.W. Sleight, J. K. Jayaraj and J. Tate, Appl. Phys. Lett. **77**, 1325 (2000).
125. C.F. Windisch, K.F. Ferris and G.J. Exarhos, J. Vac. Sci. Technol. **19**, 1647 (2001).
126. C. F. Windisch, G. J. Exarhos, K. F. Ferris, M. H. Engelhard and D. C. Stewart Thin Solid Films, **398–399**, 45 (2001).
127. R.L. Hoffman, B.J.Norris, J.F.Wager, App. Phys.Lett. **82**, 733 (2003).
128. S. Masuda, K. Kitamura, Y. Okumura, S. Miyatake, H. Tabata and T. Kawai, J. Appl. Phys. **93**, 1624 (2003).

129. P. F. Carcia, R. S. Mclean, M. H. Reilly, and G. Nunes, Jr. *Appl. Phys. Lett.* **82**, 1117 (2003).
130. E. M. C. Fourunato, P. M. C. Barquinha, A. C. M. B. G. Pimentel, A. M. F. Goncalves, A. J. S. Marques, R. F. P. Martins, and L. M. N. Pereira, *Appl. Phys. Lett.* **85**, 2541 (2004).
131. Y. J. Li, Y. W. Kwon, M. Jones, Y. W. Heo, J. Zhou, S. C. Luo, P. H. Holloway, E. Douglas, D. P. Norton, Z. Park, and S. Li, *Semicond. Sci. Technol.* **20**, 720 (2005).
132. S. M. Sze, *Physics of Semiconductor Devices*, John Wiley & Sons, New York, 1981.
133. J. A. Misewich and A. G. Schrott, *Mat. Res. Soc. Symp. Proc.* **623**, 3 (2000).
134. D. K. Schroer, *Semiconductor Material and Device Characterization*, John Wiley & Son, New York, 1990.
135. Y. W. Heo, Y. Kwon, Y. Li, J. Pearton, and D. P. Norton, *Appl. Phys. Lett.* **84**, 3474 (2004).
136. N. Takahashi, M. Shiota, Y. Zhu, M. Shimizu, D. Hirata, Y. Sakamoto, T. Sugino, and J. Shirafuji, *Proc. 7th Int. Conf. on Indium Phosphide and related materials*, 597-600 (1995).
137. E. M. Kaidashev, M. Lorenz, H. Von Wencksterin, A. Rahm, H.-C. Semmelhack, K. H. Han, G. Benndorf, C. Bundesmann, H. Hochmuth, and M. Grundmann, *Appl. Phys. Lett.* **82**, 3901 (2003).
138. G. Xiong, J. Wilkinson, B. Mischuck, S. Tuzemen, K. B. Ucer, and R. T. Williams, *Appl. Phys. Lett.* **80**, 1195 (2002).
139. C. D. Wagner, W. M. Riggs, L. E. Davis, J. F. Moulder, G. E. Muilenberg, *Handbook of X-ray Photoelectron Spectroscopy*, Perkin-Elmer Corporation, 1978.
140. Ya. I. Alivov, J. E. Van Nostrand, D. C. Look, M. V. Chukichev, and B. M. Ataev, *Appl. Phys. Lett.* **83**, 2943, (2003).
141. Ya. I. Alivov, E. V. Kalinina, A. E. Cherenkov, D. C. Look, B. M. Ataev, A. K. Omaev, M. V. Chukichev and D. M. Bagnall, *Appl. Phys. Lett.* **83**, 4719, (2003).
142. A. Osinsky, J. W. Dong, M. Z. Kauser, B. Hertog, A. M. Dabiran, P.P. Chow, S. J. Pearton, Ol Lopatiuk, and L. Chernyak, *Appl. Phys. Lett.* **85**, 4272, (2004).
143. A. Tsukazaki, A. Ohtomo, T. Onuma, T. Makino, M. Sumiya, K. Ohtani, S. F. Chichibu, S. Fuke, Y. Segawa, H. Ohno, H. Koinuma, and M. Kawasaki, *Nat. Mater.* **4**, 42, (2005).

144. D. K. Hwang, S. H. Kang, J. H. Lim, E. J. Yang, J. Y. Oh, J. H. Yang, and S. J. Park, *Appl. Phys. Lett.* **86**, 222101, (2005).
145. K. Ip, Y. W. Heo, D. P. Norton, S. J. Pearton, J. R. Laroche, and F. Ren, *Appl. Phys. Lett.* **85**, 1169 (2004).
146. K. Ip, Y. Li, D. P. Norton, S. J. Pearton, F. Ren, *Appl. Phys. Lett.* **87**, 071906 (2005).
147. H. Ohta, H. Mizoguchi, M. Hirano, S. Narushima, T. Kamiya, and H. Hosono, *Appl. Phys. Lett.* **82**, 1029 (2003).
148. A. Tiwari, C. Jin, D. Kumar, J. Narayan, *Appl. Phys. Lett.* **83**, 1773 (2003).
149. D. K. Hwang, K. H. Bang, M. C. Jeong, and J. M. Myoung, *J. Crystal Growth* **254**, 449 (2003).
150. D. K. Schroeder, *Semiconductor Material and Device Characterization*, John Wiley & Sons, New York, 1990.
151. M. Trivedi and K. Shenai, *J. Appl. Phys.*, **85**, 6889, (1999).
152. Su-Shia Lin, Jow-Lay Huang, P. Sajgalik *Surf. Coat. Technol.* **190**, 39 (2005).
153. K. H. Kim, K. C. Park, and D. Y. Ma, *J. Appl. Phys.* **81**, 7764 (1997).
154. W. J. Jeong, S. K. Kim, and G. C. Park, *Thin Solid Film* (in press).
155. Y. Igasaki and H. Saito, *J Appl. Phys.* **70**, 3613 (1991).
156. K. Kamata, H. Misuharshi, and H. Fujita, *Appl. Phys. Lett.* **63**, 3353 (1993).
157. K. Ogata, D. Kawaguchi, T. Kera, Sz. Fujita, and Sg. Fujita, *J. Cryst. Growth* **159**, 312 (1996).
158. D. C. Look and B. Claflin, *Phys. Stat. Sol. (b)* **241**, 624 (2004).
159. I. Hamberg and C. G. Granqvist, *J. Appl. Phys.* **60**, R123 (1986).
160. Onwona Agyeman, Chao-Nan Xu, Wensheng Shi, Xu-Guan Zheng and Morio Suzuki, *Jpn. J. Appl. Phys.* **41**, 666 (2002).
161. Y.G. Wang, S. P. Lau, X. H. Zhang, H. W. Lee, S. F. Yu, B. K. Tay, H. H. Hng. *Chem. Phys. Lett.* **375**, 113 (2003).
162. N. Ohashi, T. Nakata, T. Sekiguchi, H. Hosono, M. Mizuguchi, T. Tsurumi, J. Tanaka, H. Haneda, *Jpn. J. Appl. Phys.* **38**, L113 (1999).

163. A. Ortiz, C. Falcony, J. Hernandez, M. Garcia, J.C. Alonso, *Thin Solid Films* **293**, 103 (1997).
164. X.L. Wu, G.G. Siu, C.L. Fu, H.C. Ong, *Appl. Phys. Lett.* **78**, 2285 (2001).

BIOGRAPHICAL SKETCH

Yuanjie Li was born on July 4, 1974, in People's Republic of China. After graduating from high school in 1993, Yuanjie Li entered the Beijing University of Aeronautics and Astronautics where she spent about 7 years to study materials science and engineering. In 1997, Yuanjie Li received a Bachelor of Engineering in the specialty of metallic materials and heat treatment. In the same year, she became a research assistant in the Thin Film and Coatings Laboratory at Beijing University of Aeronautics and Astronautics and started her graduate study under the supervision of Professor Shengkai Gong. Her research field for her master's degree was focused on the novel properties of Fe/Cu nano-scale multilayer materials grown by electron beam physical vapor deposition. In 2000, Yuanjie Li received her Master of Engineering in materials science.

Yuanjie Li entered the Department of Materials Science and Engineering at the University of Florida to pursue a Ph.D. degree in Fall, 2001. After working as a teaching assistant for a year, she joined Professor David Norton's research group in the summer of 2002 and has been working on the ZnO-based thin films for electrical and optoelectronic devices since then.